IntechOpen

Characterizations of Some Composite Materials

Edited by Hosam El-Din M. Saleh and Martin Koller

CHARACTERIZATIONS OF SOME COMPOSITE MATERIALS

Edited by **Hosam El-Din M. Saleh** and **Martin Koller**

Characterizations of Some Composite Materials
http://dx.doi.org/10.5772/intechopen.73357
Edited by Hosam El-Din M. Saleh and Martin Koller

Contributors

Hammat Valiev, Bo Jin, Miguel Angel Hidalgo-Salazar, Fernando Luna-Vera, Juan Pablo Correa-Aguirre, Anton Yegorov, Vitaly Ivanov, Olga Zhdanovich, Marina Bogdanovskaya, Vasily Retivov, Kseniya Tcarkova, Olga Kosova, Alessandra Caggiano, Luigi Nele, Roberto Teti, Valentina Lopresto, Tiziana Segreto, Abdelkader Rahmouni, Mohammed Belbachir, Hosam Saleh

Notice

First published in London, United Kingdom, 2019 by IntechOpen
eBook (PDF) Published by IntechOpen, 2019
IntechOpen is the global imprint of INTECHOPEN LIMITED, registered in England and Wales, registration number: 11086078, The Shard, 25th floor, 32 London Bridge Street
London, SE19SG – United Kingdom
Printed in Croatia

British Library Cataloguing-in-Publication Data
A catalogue record for this book is available from the British Library

Additional hard and PDF copies can be obtained from orders@intechopen.com

Characterizations of Some Composite Materials
Edited by Hosam El-Din M. Saleh and Martin Koller

p. cm.

Print ISBN 978-1-78984-911-0

Online ISBN 978-1-78984-912-7

eBook (PDF) ISBN 978-1-83881-734-3

Meet the editors

Hosam Saleh is a Professor of Radioactive Waste Management in the Radioisotope Department, Atomic Energy Authority, Egypt. He was awarded his MSc and PhD degrees in Physical Chemistry from Cairo University. He is interested in studying innovative economic and environment-friendly techniques for management of hazardous and radioactive wastes. He has authored many peer-reviewed scientific papers and chapters. He has been the book editor of different books related to valuable international publishers.

Martin Koller is an experienced senior researcher in the field of bio-mediated polyhydroxyalkaoate (PHA) production, encompassing design and development of continuous and discontinuous fermentation processes, and novel downstream processing techniques for sustainable biopolymer recovery from microbial biomass. His focus of research is enhanced cost-efficiency of PHA production from surplus materials using both eubacteria and halophile archaea as whole cell biocatalysts. In the past, he was also involved in the development of bio-composite materials.

Contents

Preface

The old quote from the renowned psychiatrist C. G. Jung, who stated that "the whole is more than just the sum of its individual parts", can also be applied to the field of composite materials. As a matter of fact, the assembly and processing of basic materials, both of natural and/or artificial origin, can create innovative materials with completely novel properties and characteristics, which are often not expected *a priori* when studying the properties of the individual starting materials.

Nowadays, we come across composite materials in almost all situations of our daily life. This may happen during shopping, when we buy food enveloped in multi-layer plastic composites and carry it home in carrier bags made of a composite material. Composites can accompany us when making sports in wintertime dressed in carbon fiber clothing, in our automobiles, where composites are used to reduce vehicle weight and to reduce CO_2 emissions, or when we are grabbing our smartphone or tablet, which is most probably protected by an injection molded plastic-based composite. As another example, when I visited a scientific conference in France last year, coffee was offered in a cup consisting of an injection molded thermoplastic starch–bagasse composite material, which constitutes a sustainable alternative to petrochemical disposable cups. Moreover, every carpenter, architect, and handyman knows about the performance benefits of reinforced wood composites, widely used wood materials with high strength and dimensional stability with applications *inter alia* in construction and the furniture industry; hence, we live in houses where composite materials are omnipresent. In addition, reinforcing plastics with glass fibers offers options to generate high-performance glass fiber composites, which are applied in the construction sector, the leisure industry, as glass tapes on boats and ships, or in oil and gas lift systems. It might also be that, as I did this morning, the respected reader of this chapter even uses extra firm dog leashes made of glass fiber composites to walk his or her dog. As another example from the construction sector, concrete composite materials are used there, in which the relatively low tensile strength and ductility of concrete are compensated by the inclusion of reinforcement materials, which provides for enhanced tensile strength and/or ductility. Only during the last few years have concrete composites started to attract global attention also as the novel materials of choice to stabilize contaminated biological or soil materials; this application even provides the possibility to finally dispose materials contaminated by radionuclides in a safe and sustainable manner.

As a biotechnologist, I became personally fascinated by special new biocomposite materials, which were produced by our project partners about ten years ago. These biocomposites were based on a matrix of microbial polyhydroxyalkanoate bioplastics, which we produced in bioreactors by feeding bacteria with carbon-rich waste streams. Now, these bioplastics were processed by our project partners together with inexpensive renewable resources like

wood dust or lignin, which typically constitute waste materials without any special use. Preparing these composites definitely helped to overcome well-known shortcomings of native polyhydroxyalkanoate bioplastics, such as high brittleness and insufficient gas barrier performance. Designed composite films were thoroughly examined regarding their melting and crystallization behavior, mechanical and viscoelastic properties, thermo-oxidative stability, and gas permeability. It was shown that the composites exhibited outstanding mechanical and gas barrier properties and expedient thermos-oxidative stability, which pre-destines them for use in packing of easily perishable products such as food. Moreover, designing biocomposites is also a promising route to increase composability of polymeric materials; in the past, automotive parts, or even machine components were already developed consisting of a matrix of a biopolymer and abundantly available filler materials such as bagasse. After the product´s life span, it can be disposed of with a clear conscience on the compost heap. A solution for the current plastic pollution problem!

Currently, we witness a tremendously dynamic development in designing and processing of composites all over the world. For example, advanced composite materials, which contain high strength fibers occupying a large volume of a polymer matrix, are developed globally in order to produce materials with enhanced elasticity and strength along the direction of the reinforcing fiber. Further, such advanced composites display expedient dimensional stability, temperature, and chemical resistance, flex performance, and are relatively easy to be processed by well-established processing technologies. Apart from established processing methods such as melt extrusion, injection molding, melt-spinning, or solvent casting, we get more and more familiar with new emerging processing techniques such as additive manufacturing (3D-printing), electrospinning, or computer-aided wet spinning to produce marketable products made of composite materials. To an increasing extent, such products find use also in the biomedical field such as for production of implants or artificial joints, or for development of scaffolds for enhanced attachment of cell cultures, e.g., for stem cell cultivation.

Not only are such composites designed to trigger fundamental physical material properties of a basic material such as density, breakage, or crystallinity; beyond that, to an increasing extent, nanotechnology enters the field of composite development; "small is beautiful" is also valid for new composites! These nano-technological approaches allow the design of completely new, smart materials with properties fine-tuned to special customer demands. Depending on the type, size, and content of applied nano-fillers, which might be cellulose nano-whiskers, glass-, silica-, or metal nanoparticles, carbon nanotubes, and many more, it is possible to markedly change and fine-tune the mechanical, electrical, electrochemical, thermal, optical, hydrophilic, piezoelectrical, and even catalytic properties of the matrix materials.

However, it is by far no trivial task to develop a new composite material, which exactly matches the performance expectations set by a customer. As Albert Einstein said: "Who never failed never tried out something new!" Hence, such R&D developments *en route* towards a smart composite material are typically cumbersome, involve steps backwards, and take time. In this context, for the development of a new composite material, the synergistic knowledge from experts of different scientific disciplines is required, which calls for the input from chemistry, physics, engineering, and environmental sciences. Especially the detailed characterization of new composite materials is the *conditio sine qua non* needed to assess the performance and applicability of a new composite material. As shown in this book, it is pivotal to define quality and performance benchmarks, which have to be meet by

a new material to outperform established products in terms of material quality, economics of its production, and sustainability aspects. Nowadays, a range of different physical and chemical techniques for analysis and characterization of new composite materials are available, and comprehensively presented in the book at hand.

Writing this brief preface, it is an outstanding pleasure for me to span the bridge between the individual chapters included in this fascinating book project. Leading scientists from diverse academic disciplines provide insights into their particular activities and knowledge related to the composite field, with special emphasis on novel and established tools to assess the quality and potential of these future-oriented hybrid materials.

Enjoy reading!

Hosam El-Din M. Saleh, Ph.D.
Atomic Energy Authority
Radioisotope Department
Nuclear Research Center
Giza, Egypt

Martin Koller
University of Graz
Office of Research Management and Service, c/o Institute of Chemistry
Graz, Austria

Introduction

Chapter 1

Introductory Chapter: Background on Composite Materials

Mohamed M. Dawoud and Hosam M. Saleh

Additional information is available at the end of the chapter

http://dx.doi.org/10.5772/intechopen.80960

1. Overview

"Composite materials" also referred to as "composition materials" or briefly "composites," as the most frequently used term, display materials consisting of two or more components; these two components display considerably diverse physical and/or chemical characteristics. Merging the two or more basic materials creates a new material with features different from the single constituents. Because the individual components remain distinct and separate within the final material structure, composites have to be strictly differentiated from material mixtures and solutions of solids.

The new composite material often displays many beneficial characteristics; in many cases, composites are stronger, of lower density, or less costly in comparison to established materials. Commonly, composites consist of two or more different components forming regions sufficiently large to be considered as continua; the basic components are usually strongly fused at the interface. A variety of both natural and synthetic materials confirm to this picture, such as mortar and concrete, reinforced rubber, alloys, polymers containing fillers, aligned and chopped fiber composites, porous and cracked media, polycrystalline (metal) aggregates, and others [1].

Composite materials are composed of individual basic materials, which are referred to as so-called constituent materials. Two main categories of constituent materials are distinguished: the matrix (aka "binder") and the reinforcement. At least one representative from each category is needed to create a composite. The matrix phase embeds, surrounds, and supports the reinforcements by preserving their relative locations. The reinforcements contribute their specific physical and mechanical assets, thus enhancing the properties of the matrix. The achieved synergism between the two phases generates material properties not observed for

the individual constituent materials, while the unlimited number of binders and reinforcements enables the designer to develop optimum combinations, thus creating tailor-made composites [2].

Well-known examples of composite materials are as follows:

- Lignocellulosic (straw) in sludge
- Wood (cellulose fibers embedded in hemicellulose and the binder lignin)
- Bones (soft protein collagen combined with the hard mineral apatite)
- Pearlite (ferrite combined with cementite) [3, 4]

Classification of composite materials occurs at two different levels:

- The first criterion of classification is based on the matrix (binder) constituent. The main composite families encompass organic matrix composites (OMCs), metal matrix composites (MMCs), and ceramic matrix composites (CMCs). The term OMC generally refers to two classes of composites, namely, polymer matrix composites (PMCs) and carbon matrix composites, which are usually called carbon-carbon composites.
- The second classification criterion refers to the reinforcement phases; here, fiber-reinforced composites (FRCs), laminar composites, or particulate composites are distinguished. FRC can be further separated into those containing discontinuous or continuous fibers, respectively, as reinforcements.
- FRC consists of fibers surrounded by matrix materials. Such composites are considered as discontinuous fiber composites or short fiber composites, if the composite properties are dependent on the fiber length. However, when the fiber length is like that, that any further increase in length does not result in further increase in the composite's elastic modulus, the composite is regarded as "continuous fiber reinforced." Fibers are generally small in diameter, and, when pressed axially, they easily twist, although they normally have proficient tensile properties. Consequently, these fibers need to be reinforced to prevent bending and buckling of the individual fibers.
- Laminar composites consist of material layers stacked together by the matrix; sandwich structures are examples for this composite category.
- Particulate composites constitute particles distributed or embedded in a binding matrix; the particles can be flakes or in powdered. For this category, concrete and wood particle boards are well-known examples [5].

A range of other classifications of composite materials exist as follows:

1. Classification according to the type of matrix materials:
   - Metal matrix composites (MMCs)

Metal fibers are generally of low costs but have a relatively high specific mass. They are applied for reinforcement of metal matrices. Because of their high density, they are not highly demanded. The main function in preparation of the metal-metal composite is enabled by the high fiber-matrix compatibility. Carbon steel fibers are used for reinforcement of metal matrices to resist temperatures up to 300°C. To reinforce metal matrices to withstand even higher temperatures, fibers made of heat resistant metals, such as tungsten or molybdenum, are applied. Some of the most commonly used fibers are listed below:

- Steel: often containing strengthening aluminum alloys.
- Tungsten: used to strengthen heat resistant materials; drawback: they are extremely heavy.
- Boric: very light, yet rigid and solid; the production is not trivial. As typical representative, boric fibers should be mentioned, in which a boron layer is attached on the surface of a thin tungsten wire by chemical deposition of BCl_3 vapor; its surface is first protected against oxidation and boron diffusion into the matrix by attaching a thin SiC layer.

○ Inorganic nonmetallic matrix composite materials.

○ Polymer matrix composites (PMCs).

These polymers display ideal matrix materials, because they are conveniently processed, are of low density, and display desirable mechanical features. Consequently, high-temperature-resistant polymeric resins are widely used in aeronautics [6].

Thermosets and thermoplastics are two major types of polymers. Thermosets are characterized by a well-bonded 3D-molecular structure built up after curing. These materials decompose instead of melting at elevated temperature. Simply altering the resin's basic composition is sufficient to change the conditions appropriate for curing and to determine other properties. In addition, they can be retained in a partially cured condition over extended periods. Moreover, thermosets are of high flexibility. Thus, they are highly suitable as matrix bases for FRC used for advanced applications. Thermosets are widely used to generate chopped fiber composites, especially when using a premixed or molding compound with fibers of specific quality and aspect ratio as starting material, as it is the case for epoxy, polymer, and phenolic polyamide resins. Thermoplastics have one- or two-dimensional molecular structure; they melt at elevated temperature and typically exhibit exaggerated melting points. As an additional advantage, their softening at elevated temperature is reversible; hence, their original properties can be restored by cooling; this facilitates applications of established compression techniques used to produce molded compounds. Currently, resins reinforced with thermoplastics constitute a steadily emerging class of composites. A lot of R&D efforts in this area nowadays are dedicated toward improving the basic properties of the resins and toward extracting the highest possible functional advantages from them for defined applications. This includes endeavors to substitute precarious metals in die-casting processes. In crystalline thermoplastics, the reinforcement considerably changes the morphology, stimulating the reinforcement to allow nucleation.

Whether crystalline or amorphous, these resins are able to change their creep properties over an extensive temperature range. However, this temperature range includes the point where usage of resins is impaired, and reinforcement in such systems can rise the failure load and their creep resistance.

Ceramic matrix composites (CMCs) and carbon-based composite materials like C/C composite materials are the best described representatives of inorganic nonmetallic matrix composites. Polymer matrix composite materials are divided into thermosetting resin-based composite materials and thermoplastic resin-based composite materials; moreover, they encompass one component polymer matrix composites and polymer blends matrix composites [7, 8].

2. Classification according to the nature of the dispersed phase:

- Continuous fiber-reinforced composites
- Fibrous fabric (textile), woven-reinforced composites
- Sheet-reinforced composites
- Very short fiber ("whiskers")-reinforced composites
- Particle-reinforced composites
- Nanoparticle-reinforced composites

3. Classification according to the type of reinforcing fibers:

- Carbon and graphite fiber composites: typical characteristics of these carbon and graphite fibers:
  - Ten times more rigid and only half the density (1.8–2 g cm^{-3}, comprises 90–95% pure carbon) in comparison to glass fibers.
  - Elongation at break is lower than observed for glass fibers.
  - Lower tensile strength at room temperature than for glass or aramid fibers; tensile strength does not decrease with temperature up to 1000°C.
  - Excellent thermal performance if oxidation-protected, stable and chemically inert up to 1000°C and when oxidation-protected: stability even up to 2000°C.
  - Minimal thermal expansion, sometimes even thermal contraction.
  - Drastically higher fatigue resistance than glass.
  - Electrical conductive.
  - A hundred times more expensive than glass.
  - High anisotropy.
  - Frequently poor adhesion to the matrix; therefore, surface modification is needed. The fibers can contain amounts of graphite, which differentiates them into carbon fiber composites, which contain predominantly amorphous carbon, and graphite fiber composites, which are characterized by a predominance of crystalline graphite.

- Preparation modes:
- Polymer pyrolysis: the currently most frequently used method; resorts to synthetic polymers like polyacrylonitrile (PAN) or to natural polymers.
- Hydrocarbon pyrolysis: even production of nanofibers is possible.
- Evaporation from the arc discharge between carbon electrodes; one resorts to the positive pressure of argon. Whiskers can be produced.
- Glass fiber composites.
- Organic fiber composites.
- Boron fiber or SiC fiber composites.

Boron is among the materials that are very challenging to make ductile, and it is highly reactive. Therefore, for use in a metal matrix, a thin layer of SiC is attached onto the fibers.

- Hybrid fiber composites [9].

2. Characteristics of composites

Based on the classification of composites, we are already familiar with the fact that there exists a myriad of different types of these materials. It is a common saying that different types of composites differ in their performance. Yet, composites also have some characteristics in common. Grace to their inherent beneficial characteristics, polymer matrix composites have developed to the fastest emergent and most extensively used composites. Compared with well-established materials like metals, polymer matrix composites display particular characteristics as follows:

1. High specific strength and high specific modulus

The most important benefits of polymer matrix composites are their high specific strength and high specific modulus. Specific strength is defined as the ratio of strength to density, while the specific modulus is the ratio of modulus to density; in both cases, length is the corresponding dimension/unit. Under the premise of equal mass, these parameters are tools to quantify the material's bearing capacity and stiffness properties, which are very significant for aerospace structural materials. **Table 1** provides an overview of values for specific strength and specific modulus of several common structural materials; it is shown that carbon fiber resin matrix composites generally show higher specific modulus and specific strength. The high specific strength and high specific modulus of composites can be explained by the high performance and low density of reinforcing fibers. As a result of relatively low modulus and high density of glass fibers, the specific modulus of the glass fiber resin matrix composites is slightly lower than measured for metallic materials.

2. Expedient fatigue resistance and high damage resistance

The fatigue failure of metallic materials is frequently of no apparent warning to the strikingness of damage. The fiber/matrix interface in composites can avoid crack propagation. The fatigue failure always starts from those links of fibers prone to break. Crack growth or destruction propagates gradually for a long time; hence, there is a substantial forerun before

Materials	Density (g/cm^3)	Tensile strength (GPa)	Elastic modulus (10^2GPa)	Specific strength (10^6cm)	Specific modulus (10^8cm)
Steel	7.8	1.03	2.1	1.3	2.7
Aluminum alloy	2.8	0.47	0.75	1.7	2.6
Titanium alloy	4.5	0.96	1.14	2.1	2.5
Glass fiber composite materials	2.0	1.06	0.4	5.3	2.0
Carbon fiber II/epoxy composite materials	1.45	1.50	1.4	10.3	9.7
Carbon fiber I/epoxy composite materials	1.6	1.07	2.4	6.7	15
Organic fiber/epoxy composites	1.4	1.40	0.8	1.0	5.7
Boron fiber/epoxy composites	2.1	1.38	2.1	6.6	10
Boron fiber/aluminum matrix composites	2.65	1.0	2.0	3.8	7.5

Table 1. Specific strength and specific modulus of some commonly used materials and fiber composites [10].

the onset of the final destruction. As it is visible from the S-N curve of fatigue properties, fatigue strength of the majority of metallic materials amounts to only 30–50% of tensile strength, while this value increases to 70–80% for carbon fiber/polyester composites; for glass fiber composites, the percentage is between these two examples.

3. Good damping characteristics

The natural vibration frequency of forced structures relates to the structure shape itself and is also proportional to the square root of the specific modulus of structural materials. Consequently, composites have a high natural frequency, and generation of a resonance in general is not easy. In parallel, the fiber/matrix interface in composites very easily absorbs vibrational energy, which results in a high vibration damping of these materials. In case vibrations occur, they can easily be stopped [10].

4. Useful processing techniques

- Fiber matrix and other raw materials can be selected according to the utilization conditions and performance requirements of the product; hence, tailor-made material can be designed on demand.
- Molding processing techniques can be applied according to the size, shape, and number of the product.
- Integrated molding can decrease the number of individual parts, which saves time and material and reduces weight.

3. Principle approach for material selection

The proper material choice for an envisaged application is of outstanding importance and key in the development of a new product. Selecting the most suitable material determines

the performance of the final product—whether it will meet the designated function and performance requirements. Inappropriate, less suitable materials can cause the following impairments:

- Technological problems occurring during the production process
- Increase of production costs, consequently higher price of the final product
- Negative ecological impact

○ Selection of material

Material selection is a multifaceted, complex process, which needs to address various factors such as:

- Material expenses
- Production cost
- Demand for energy and raw materials (material intensity of the process)
- The possible environmental impact of material selection, which depends on the production and consumer cycle (cradle-to-grave life cycle)
- Accessibility to material recycling:

○ The interrelations of material, technology, and product:

The functionality of the product (based on its individual components), structure (its shape), material, and technology closely interacts and cannot be regarded independently from each other; consequently, the selection of material cannot be done independently of the technology.

○ Parameters and needs during product design/development:

- The choice of most suitable, individual components regarding their future performance.
- Assessment of the compatibility of components—each phase of the composite material has to preserve its beneficial features; the individual components must not have a negative effect/damage on each other.
- Determining an applicable geometrical form for each phase—while the stronger parts (fibers, strips, belts, etc.) need to be elongated, the weaker phase should wrap the stronger one and bring individual fibers closely in contact within a single structure.
- Composite phases should be distributed in a way which enables them to function in a synergistic way.
- Knowledge on the conditions in which the future composite will function in praxi, such as temperature, humidity, pressure, abrasion, etc.

4. Applications

- Space crafts: antenna structures, radar, rocket engines, satellite structures, solar reflectors, etc.
- Aircrafts: airfoil surfaces, compressor blades, engine bay doors, fan blades, flywheels, helicopter transmission structures, jet engines, rotor shafts in helicopters, turbine blades, turbine shafts, wing box structures, etc.
- Automobiles: abrasive materials, bearing materials, electrical machinery, engine parts (bearing materials, connecting rod, crankshafts, cylinder, piston, etc.), pressure vessels, truss members, cutting tools, electrical brushes, etc.
- Wind turbine blades: wind turbine blades of carbon-wood epoxy composites.
- Cemented carbide: usual cemented carbides are based on tungsten carbide (WC), titanium carbide (TiC), and chromium carbide (Cr_3C_2).

*Tungsten carbide cermets (Co-binder): cutting tools are most frequently used; others: dies for powder metallurgy, indenters for hardness testers, wire drawing dies, rock drilling bits, other mining tools.

*Titanium carbide cermets (Ni-binder): high-temperature applications such as gas turbine nozzle vanes, cutting tools for steels, valve seats, thermocouple protection tubes, torch tips, etc.

*Chromium carbides cermets (Ni-binder): gage blocks, bearing seal rings, valve liners, spray nozzles, etc. [11].

Author details

Mohamed M. Dawoud and Hosam M. Saleh*

*Address all correspondence to: hosamsaleh70@yahoo.com

Radioisotope Department, Nuclear Research Center, Atomic Energy Authority, Egypt

References

[1] Hashin Z. Analysis of composite materials—A survey. Journal of Applied Mechanics. 1983;**50**(3):481-505

[2] Hon D, Shiraishi N, editors. Wood and Cellulose Chemistry. 2nd ed. New York: Marcel Dekker; 2001. p. 5

[3] Ibrahim ID, Jamiru T, Sadiku RE, Kupolati WK, Agwuncha SC, Ekundayo G. The use of polypropylene in bamboo fibre composite and their mechanical properties—A review. Journal of Reinforced Plastics and Composites. 2015;**34**(16):1347-1356

[4] Altenbach H et al. Mechanics of Composite Structural Elements. Berlin: Springer-Verlag; 2004

[5] Miracle DB, Donaldson SL. Introduction to composites. ASM Handbook. 2001;**21**:3-17

[6] Wang R-M, Zheng S-R, Zheng Y-P. Polymer Matrix Composites and Technology. WP, Woodhead Publishing, Oxford; 2011

[7] Thostenson ET, Ren Z, Chou T-W. Advances in the science and technology of carbon nanotubes and their composites: A review. Composites Science and Technology. 2001;**61**(13):1899-1912

[8] Das B et al. Nano-indentation studies on polymer matrix composites reinforced by few-layer graphene. Nanotechnology. 2009;**20**(12):125705

[9] Berthelot J-M. Composite Materials: Mechanical Behavior and Structural Analysis. New York, NY, USA: Springer; 1999

[10] Christensen RM. 2005. Mechanics of Composite Materials. Mineola, New York; 2012

[11] Gay D, Hoa SV, Tsai SW. Composite Materials: Design and Applications. Fl USA: CRC Press; 2003

Section 2

Characterization of Some Composite Materials

Chapter 2

Atomic Force and Electron Scanning Microscopy of Silicone Composites

Hammat H. Valiev, Alexander N. Vlasov,
Vyacheslav V. Vorobyev, Yuliya N. Karnet,
Yury V. Kornev and Oleg B. Yumaschev

Additional information is available at the end of the chapter

http://dx.doi.org/10.5772/intechopen.79537

Abstract

The conclusions of direct numerical simulation obtained earlier, within the cluster quantum-chemical approximation, are used in experimental investigations of polydimethylsiloxane composites with schungit or silica. The surface structure of these composites by atomic force and scanning electron microscopy was studied. Correlation of the distribution of micro- and nanodimensional fillers in the polymer matrix with the physical-mechanical properties of the composites was established.

Keywords: polydimethylsiloxane composites, schungit, silica, atomic force and scanning electron microscopy

1. Introduction

The problems of increasing the strength of polymer materials are important for both fundamental science and applied research. For example, the polydimethylsiloxane (PDMS) CKTH rubbers, as representative of organosilicon polymers, are of the great importance in industry. Materials made on the basis of such CKTH rubbers are resistant to temperatures from −90 to +300°C, as they possess high hydrophobicity, chemical inertness, dielectric properties, vibration resistance, resistance to fungi and microorganisms, and resistance to ozone, oxidizers, and ultraviolet rays. Also they are physiologically inert, tissue and hemocompatible, gas permeable (the highest permeability of all known polymers), selective for gas permeability, and easily sterilized. Unlike organic, CKTH silicone rubbers are more economical, reliable, and durable even under extreme conditions; and are also easy to process. However, they have low

mechanical strength. Reinforcement of these polymers is usually achieved with fillers. The nature of the interaction of matrix elastomers with fillers is determined by the chemical nature, dispersion, shape, activity of the filler particles, the possibility of chemical bonds between the components of composites, and the relationship between the processes of amplification and structuring. In the works of Mark and coworkers [1, 2], which generalize numerous studies, it is stated that the physical and mechanical properties of synthetic low-molecular-weight siloxane elastomers filled with silica are significantly enhanced. It is of great interest also for the search for new reinforcement fillers to PDMS. One of favorable proposals may be schungit [3]. In the development of advanced composites, it is advisable preliminary to perform the molecular computational modeling, which is an effective method of a virtual analysis of the structural, energetic, and micromechanical properties of micro- and nanomaterials. As reported in [4–6], the energetic and structural characteristics of elastomer complexes with silica or schungit have been calculated quantum chemically under developed NDDO/sp-spd semiempirical original program [7]. Numerical calculations on the supercomputer MBC-5000 in the Interdepartmental Supercomputer Center were performed. The microscopic characteristics of nanomechanical behavior, deformation, and strength characteristics of silica or schungit adsorbates with polydimethylsiloxane oligomer molecules during uniaxial tension based on this program in the cluster approximation were examined. It was deduced that one could expect a substantial reinforcement of physical-mechanical properties for such composites.

We used the conclusions of these calculations in the practical synthesis of siloxane composites with schungit and silica. The multistage physical-chemical modification technology for obtaining the active nanostructured schungit filler for rubbers, based on these quantum-chemical calculations, has also been developed.

According to the results of [8], there is an increase in the tear resistance and in the specific work of the deformation during fracture, with preservation of the increased strength properties of synthetic thermally stable low-molecular-weight silicone elastomers based on CKTH-A, filled with micro- and nanoscale schungit and silica SIPERNAT 360.

To further elucidate the nature of the onset of strengthening effects, knowledge of the distribution of fillers in these elastomeric matrices is necessary. The surface structure of these composites, using atomic force and electron scanning microscopy, in the present chapter was studied as extension of the studies [8–11].

2. Examination procedures and materials

As the basis of the composite matrix, silicone low-molecular thermal shock resistant synthetic rubber CKTH brand A (silanol terminated polydimethylsiloxane, HO [–Si $(CH_3)_2$ O–] n H) was chosen. As a filler of CKTH-A rubber a natural schungit mineral was used (Zazhoginsky deposit, Carbon-Shungite Trade Ltd., Karelia, Russia) [3]. The rock is a natural composite, in the carbon matrix of which are distributed highly dispersed silicate particles and small amounts of other oxides. The chemical composition of schungit, according to [3], used in this work is shown in **Table 1**.

Fillers were both the original schungit from provider and the original schungit milled by us in a ball planetary mill PM100 (Retsch, Germany) under different environments. The fillers were added to the CKTN-A rubber according to the compositions given in **Table 2**, kneaded by hand, and then passed through rolls. The resulting mixtures were evacuated for 15 minutes; then, a catalyst No 68 was introduced with a certain concentration for each composition and again evacuated. The samples were placed in Teflon forms and cured [8]. **Table 2** shows the ingredients of the samples used and corresponding code of synthesized composites.

CKTN-A composites with silica fillers, precipitated silicon dioxide, and SIPERNAT 360 (Evonik Industries AG, Germany), were prepared analogues to composites with schungit. **Table 3** shows the ingredients of the samples studied.

The atomic-force microscope (AFM) easyScan (Nanosurf, Switzerland), operating in a contact mode at ambient conditions, using also the force modulation mode, or in the semi-contact mode with the phase contrast mode, was used. In a semi-contact mode, a SuperSharpSilicon probe (Nanosensors, Switzerland) with a tip radius of about 2 nm was

SiO_2	TiO_2	Al_2O_3	FeO	MgO	CaO	Na_2O	K_2O	S	C	H_2O_{cryst}
57.0	0.2	4.0	2.5	1.2	0.3	0.2	1.5	1.2	29.0	4.2

Table 1. Chemical composition of schungit (weight percentage).

Composite ingredients name	Code of composites								
	C300	C301	C302	C303	C304	C305	C306	C307	C308
	Weight percentage								
CKTH-A rubber	100	90	80	70	60	90	80	70	60
Schungit (original)		10	20	30	40				
Schungit (milled)						10	20	30	40
Total	100	100	100	100	100	100	100	100	100

Table 2. Ingredients of the synthesized composites with schungit filler.

No	Composite ingredients name	Code of mixture					
		C 300	C 309	C 310	C 311	C 312	C 313
		Weight percentage					
1	CKTH-A rubber	100	80	90	80	70	60
2	SIPERNAT 360	—	20	10	20	30	40
3	Total	100	100	100	100	100	100

Table 3. Ingredients of the synthesized composites with silica filler.

used. Image processing was performed using the SPIP™—advanced software package for processing and analyzing microscopy images at nano- and microscale (Image Metrology, Denmark). The scanning electron microscope (SEM) Merlin (Carl Zeiss, Germany) worked with an accelerating voltage of 5 kV and beam current of 300 pA. Investigations of the physical-mechanical properties of the composites were conducted on universal testing machine UTS-10 (Ulm, Germany), and nanoscale mechanical properties were studied with NanoTest 600 (MicroMaterials, UK) [8].

3. Experimental results

Initially, schungit powder samples, after deposition on the surface of highly oriented pyrolytic graphite (HOPG) from a suspension in toluene, were tested by AFM. The AFM topography and phase contrast images established the particle sizes of the original schungit from provider in the range from 1 to 5 μm. AFM images of the schungit particles deposited on the HOPG after milling in a ball planetary mill PM100 are shown in **Figure 1**. The agglomerates of nanosized schungit in the range from 50 to 250 nm are clearly detected.

AFM images of surface of pure C 300 rubber CKTH-A are shown in **Figure 2**. The scans visualized typical nodular polymer structure.

In **Figure 3**, an example of AFM scan on sample C 308 from the synthesized composites listed in **Table 2** is displayed. The distribution and size of schungit fillers, presented as bright color in the background of polymeric matrix, clearly are visualized.

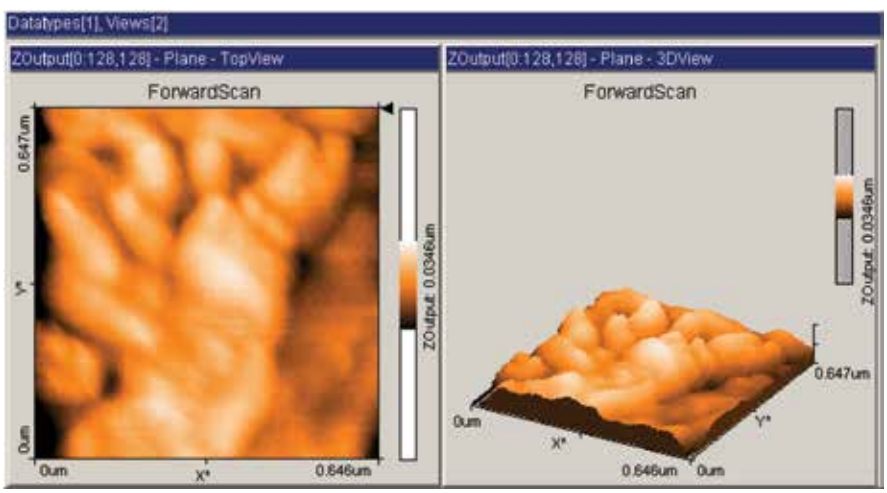

Figure 1. AFM images of the schungit agglomerates after milling, deposited on the HOPG surface. Scan XY = 0.646 × 0.646 microns. Left—topography and right—3D view.

http://dx.doi.org/10.5772/intechopen.79537

The AFM images data processing showed that the aggregate sizes of these nanostructured schungit fillers in composite C 308 are located in the range from 50 nm to 2 μm, and the nearest distance between them on average is 300 nm.

Electron microscopic photographs of the C 308 composite are shown in **Figure 4a** and **b**. The SEM surface topography C 308 composite, prepared in the form of plate samples, is presented in **Figure 4a** and SEM images of its perpendicular cross section in **Figure 4b**. It is well known that the quality of many materials in particular of composites depends on a large extent on the homogeneity of the materials realized. Visualized by these methods

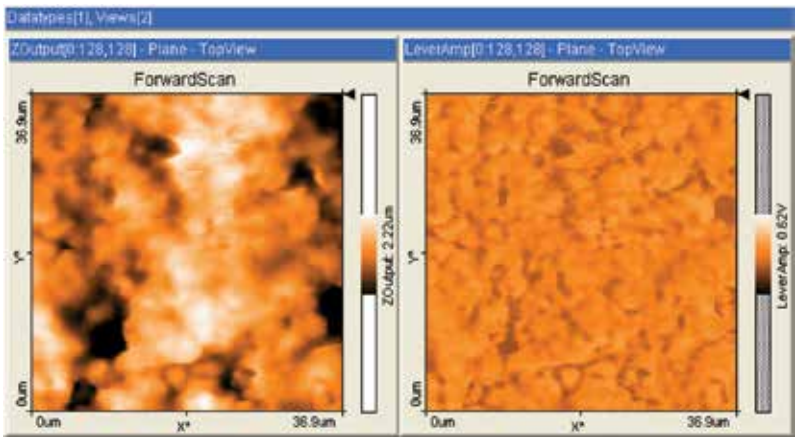

Figure 2. AFM images of the surface of the pure CKTH -A rubber C 300. Scans XY = 36.9 × 36.9 microns. Left—topography and right—phase contrast.

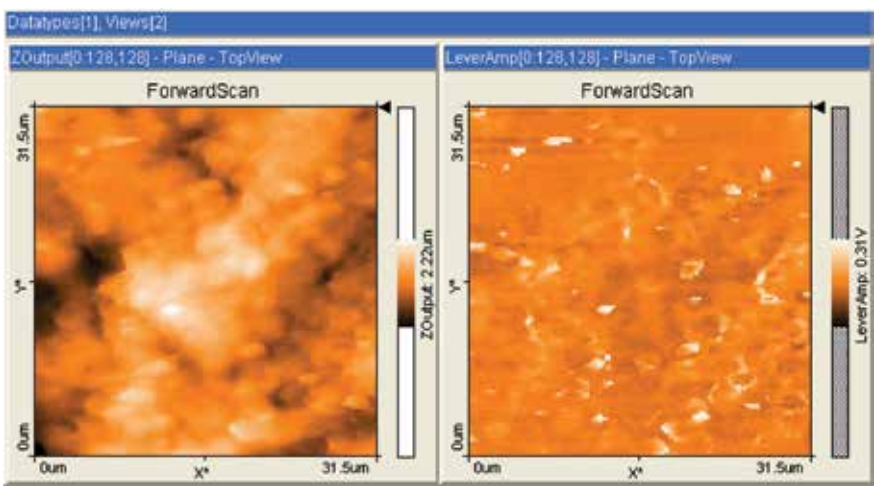

Figure 3. AFM surface images of C 308 composite. Scans 31.5 × 31.5 microns. Left—topography and right—phase contrast.

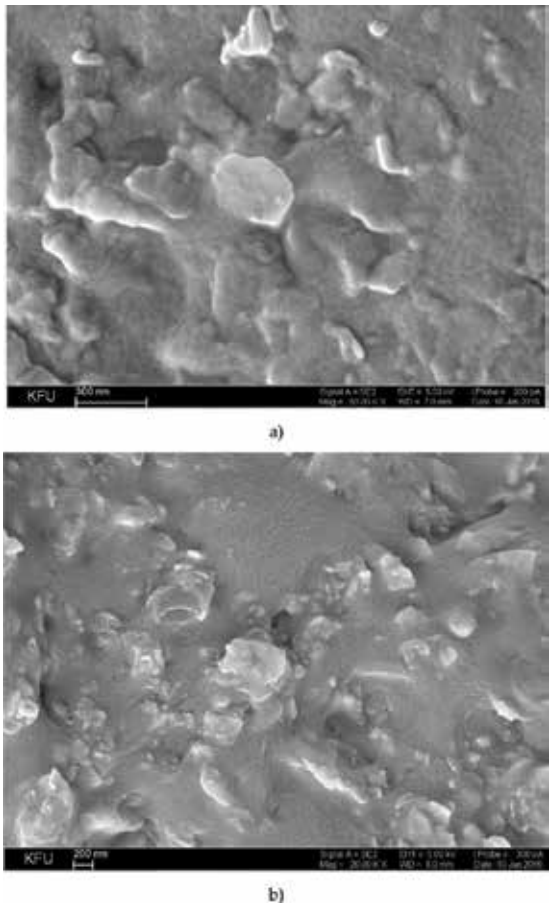

Figure 4. SEM images of the top surface topography plate C 308 composite (a) and of the plate perpendicular cross section (b). Unite scales: (a) 300 and (b) 200 nanometer, respectively.

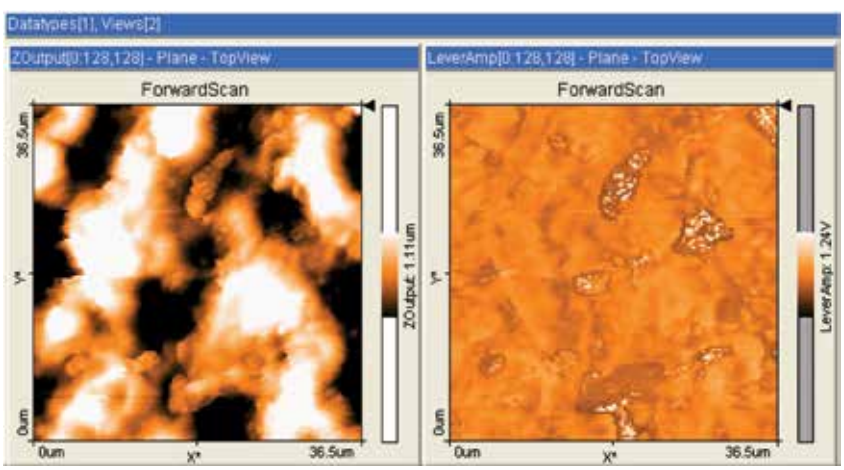

Figure 5. AFM images of the surface structure of composite C 311. Scans XY = 36.5 × 36.5 microns. Left—topography and right—phase contrast.

http://dx.doi.org/10.5772/intechopen.79537

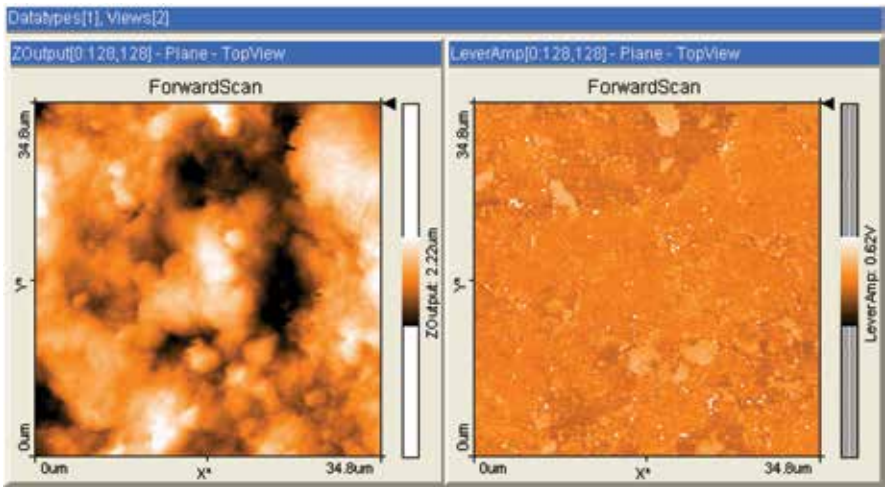

Figure 6. AFM images of the surface structure of composite C 313. Scans XY = 34.8 × 34.8 microns. Left—topography and right—phase contrast.

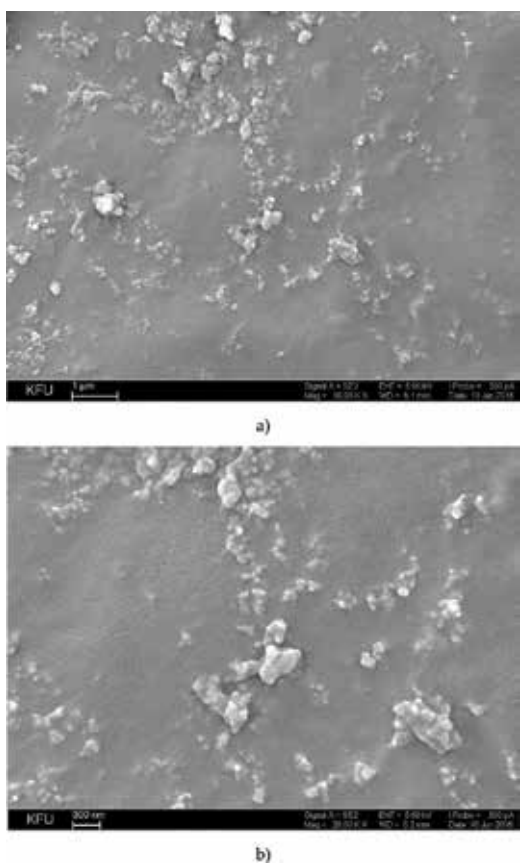

Figure 7. SEM images of the surface structure of sample C 311. Unite scales: (a) 1 micron and (b) 300 nm, respectively.

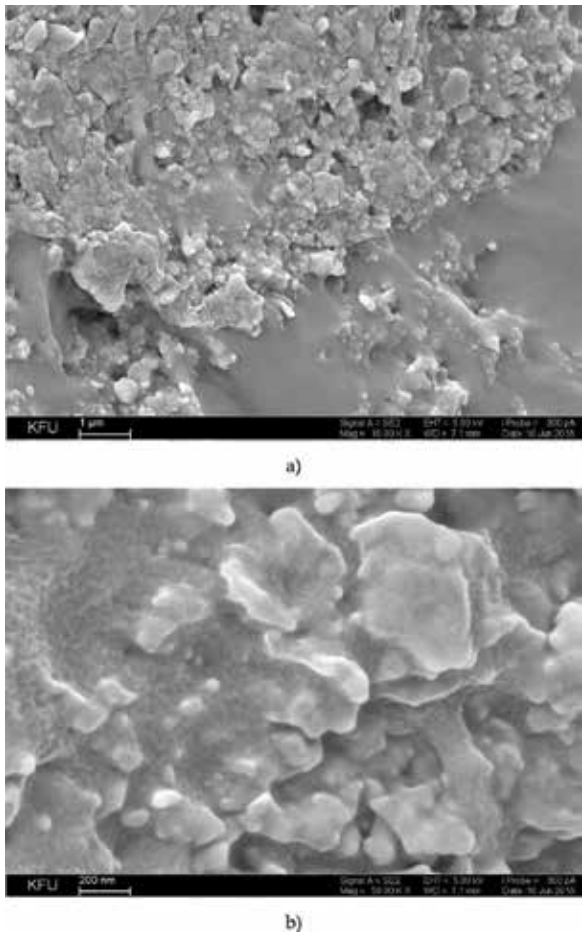

Figure 8. SEM pictures of the structure of the cross sections of the surface of sample C 311. Unite scales: (a) 1 micron and (b) 200 nm, respectively.

of AFM and SEM, the composite C 308 surface morphology shows that the nanosized schungit fillers are homogeneously dispersed in the polymer matrix and are well adhered to the polymer matrix. This finding is very important for understanding the reasons of reinforcing the physical-mechanical properties of initial CKTH-A rubber with used nano-structured schungit filler.

AFM surface images of C 311 composite CKTN-A rubber with silica SIPERNAT 360 fillers are shown in **Figure 5**, and of composite C313 in **Figure 6**. The internal microstructure and agglomerates sizes of this filler in composites are of the same dimensions as in the case of nanosized schungit filler.

SEM images of the top surface topography of the plate of the same C 311 composite are shown in **Figure 7** and of the plate perpendicular cross section in **Figure 8**.

These SEM images show the same approximate pictures of fillers dispersed distributions in the elastomer matrices and mean values of their aggregate sizes as deduced from AFM measurements; additionally SEM scans of the plate perpendicular cross sections visualized the space arrangement of fillers in these composites.

4. Discussions

The application of SEM and AFM methods to visualize topography of surfaces and cross sections of investigated silicone rubber composites with schungit and silica SIPERNAT 360 fillers allowed direct observation of changes in the structure of composite elastomers on the micro- and nanometer range by increasing their concentrations. It is known that in silicone compositions, along with the interactions between the filler and the polymer matrix, there is also a process of agglomeration and structuring of the filler particles [1, 2]. As established by the data of AFM and SEM (**Figures 3–8**), a rather homogeneous distribution of the filler in the elastomeric matrix takes place in the investigated composites. Correlation of these results with the physical-mechanical properties of these materials, studied in [8], makes it possible to understand the cause of the enhancing ability of nanostructured schungit in organosilicon elastomers, due to the formation of a spatial filler network in the polymer matrix. These data make it possible to understand the reasons for the schungit filler manifestation of the reinforcing properties in the CKTH-A rubber, as conditioned not only by the chemical affinity of the amorphous carbon and the silica with the polydimethylsiloxane matrix, but also by a fairly uniform spatial distribution of the filler in the composite. The role of polar hydroxyl groups (OH) bounded to silica part of the schungit (silanol groups) interacting with siloxane segments (Si–O–Si) of matrix is also important, because the formed complex prevents the macroscopic agglomeration of initial schungit particles during the introduction of the polymer. The resulting increase in the interaction surface of the nanostructured filler with the polymer macromolecules leads to an effective reinforcement of the initial polydimethylsiloxane matrix. As reported in [8], the tests of these composites on a machine UTS-10 showed an increase in the tensile strength from about 0.5 MPa in original CKTH-A rubber to 3.6 MPa in C 308 composite, and tear resistance from 1.3 to 7.0 kN/m, respectively. It was also showed that these rubber composites with nanostructured schungit fillers have values of the specific work deformation for destruction belonging to the same regions of magnitude as silica filled composites with the same matrix. These results, when compared with traditional silicon dioxide filler [1, 2], show good effectiveness of the present nanostructured schungit as reinforcement filler in polydimethylsiloxane.

The obtained images of the topography and material contrast of the surface of the composites with silica SIPERNAT 360 fillers also made it possible to visualize a fairly uniform distribution of silica particles in a matrix of silicone rubber. Tests of vulcanizates of these mixtures on a tensile machine UTS-10 showed an increase in the tensile strength from about 0.5 MPa in C300 to 3.0 MPa in C 311 composites, and tear resistance from 1.3 to 3.4 kN/m, respectively, and in C313 composite to 4.1 MPa and 7.1 kN/m accordingly [8]. Studies on the NanoTest 600 measuring system by the method of nanoindentation are in accord with these results. The obtained data make it possible also to understand the reasons for the manifestation of the

SIPERNAT 360 filler, with the reinforcing properties in the CKTH-A rubber as conditioned not only by the chemical affinity of the silicon dioxide and the matrix, but also by the fairly uniform spatial distribution of the filler in the composite. The role of polar hydroxyl groups (OH) associated with the filler SIPERNAT 360 (silanol groups) interacting with silicone segments (Si–O–Si) of the SKTN-A silicone analogous to nano schungit is important, with the formation of a hydrogen bond. This also makes it possible to prevent macroscopic agglomeration of the silica when introduced into the polymer, ensuring homogeneity of the filler distribution in the composite. The resulting increase in the interaction surface of the filler with the polymer leads to an effective hardening of the initial silicone matrix.

The experimental verifications of numerical semi-empirical quantum-chemical predictions that nano schungit and silica may be active also in the reinforcement of butadiene-styrene rubbers are shown in [9, 10].

5. Conclusions

The application of SEM and AFM methods to visualize topography of surfaces and sections of investigated silicone rubber composites with schungit and silica SIPERNAT 360 fillers allowed direct observation of changes in the internal structure of fillers in composite elastomers in the micro- and nanometer range. The correlation of these results with the physical-mechanical properties of the composites is important for the development of the basic principles of reinforcement material strengths. The preliminary direct numerical calculations within the framework of the cluster quantum-chemical approximation of the schungit nanostructure and its components, predicting the effectiveness of its use as a filler in elastomers proved to be valuable for conducting these experiments. The presented experimental results show both theoretical and practical significance of the quantum-chemical approach proposed for computer selection of components for elastomeric composites and ways of modifying their fillers in order to predict the technologies for obtaining materials with improved strength characteristics. This developed computational technique can be applied in similar problems of designing new advanced materials.

Conflict of interest

The authors declare that they have no “conflict of interest.”

Author details

Hammat H. Valiev[1]*, Alexander N. Vlasov[1], Vyacheslav V. Vorobyev[2], Yuliya N. Karnet[1], Yury V. Kornev[1] and Oleg B. Yumaschev[1]

*Address all correspondence to: hhvlv@mail.ru

1 Foundation Russian Academy of Sciences, Institute of Applied Mechanics RAS, Moscow, Russia

2 Interdisciplinary Center “Analytical Microscopy”, KFU, Kazan, Russia

References

[1] Mark J, Schaefer D, Gui Lin. The Polysiloxane. Oxford University Press, USA; 2015. 296 p

[2] Mark J, Allcock H, West R. Inorganic Polymers. 2nd ed. Vol. 334. NY: Oxford University Press; 2005

[3] Filippov M, Golubev A, Medvedev P, et al. Organic Matter of Schungite-Bearing Rocks of Karelia: Genesis, Evolution, Methods of Study Petrozavodsk. Vol. 206. Russia; Karelian Research Center, Russian Academy sciences; 1994. 206 p

[4] Nikitina E. Computational modelling of surfaces and interfaces of nanoobjects. In: Mechanics of Composite Materials and Structures. 2001;**7**:288-310

[5] Nikitina E, Barthel H. Quantum-chemical study on the mechanical behaviour of polydimethylsiloxane under deformation: Interaction with fumed silica surfaces. Composite Interfaces. 2001;**8**:263-290

[6] Yanovsky Y, Myagkov N, Nikitina E. Computer modeling and nanoscopic investigation of the structure and properties of shungite. Mechanics of Composite Materials and Structures. 2006;**12**:513-529

[7] The software component NDDO/sp-spd of high-precision semi-empirical calculations in sp- and spd-bases, which includes a set of programs for obtaining structural, electronic, energy, deformation and spectroscopic characteristics of atomic-molecular systems up to 1000 atoms. Certificate of State Registration of the Computer Program No. 209614949. 2009

[8] Kornev Y, Chirkunova S, Boyko O. Investigation of the effect of dispersity of schungite mineral on the complex of properties of elastomeric compositions based on SKTN-A rubber. Kauchuk and Rubber. 2012;**6**:10-14

[9] Yanovsky Y, Nikitina E, Karnet Y. Quantum mechanics simulation and experimental study of adhesive interaction and aggregation of carbon-silicate nanoparticles—Reinforcing fillers of polymer composites. Physical Mesomechanics. 2014;**17**:39-49

[10] Valiev H, Karnet Y, Kochurov N. Atomic force microscopy and physical—Mechanical properties of new elastomeric composites. Materials Physics and Mechanics. 2016;**26**: 45-48

[11] Valiev H, Vorobyev V, Karnet Y. Application of quantum-chemical modeling results in experimental investigations of silicone composites. Materials Physics and Mechanics. 2017;**32**:293-297. DOI: 10.18720/MPM.3232017-9

Chapter 3

Out of Autoclave Metal and FRP Composites Thermo-Hydroforming

Bo C. Jin, Xiaochen Li, Karl Neidert and Michael Ellis

Additional information is available at the end of the chapter

http://dx.doi.org/10.5772/intechopen.81600

Abstract

In this chapter, we explore a novel type of thermo-hydroforming process conceived to expand the role of sheet metal hydroforming machines from one of just forming sheet metal materials into one of being able to form multiple materials. This work specifically focuses on the use of thermohydroforming to shape and thermal catalyze prepreg composite sheets into rigid parts of complex 3D geometry. Elastomeric Sheet Hydroforming is an excellent low-cost manufacturing method requiring a single tool die on only one side. The mating die is a flexible membrane backed by fluid under high pressure. Various designs configurations exist that allow for significant pressure levels of up to 1400 Bar (20,000 psi), to be contained. The cycle life of the containment vessel components is commonly designed to accommodate up to 1 million cycles of use over 40 years. However, these machines can be expensive ranging in cost from several hundred thousand up to $6 million dollars. Expanding the market scope and potential of the press by enabling them to also form composites will provide benefit to both the machine owners and their customers. The intent of this project is to advance the state of the art in composites forming by demonstrating through FEA modeling that a hydroforming machine can be potentially configured to form thermally catalyzed prepreg composite panels. It is believed that the concept in like manner, will also be applicable to forming metal-composite hybrid panels, stratified metal thermoplastic laminates, thermoplastic synthetic granites and of course sheet metal materials. This concept seeks to benefit the American Manufacturing Industry and create jobs in the U.S. by providing a low-cost method for manufacturers to produce medium to very large sized high-quality sheet composite parts of an advanced nature in construction. This application is for operations requiring volumes less than 30,000 forming cycles per year per machine. Processes currently exist in the industry that utilizes heated air or heated glycol to form sheet materials. However, this process seeks to offer greater benefit by using pure water as a high thermal conductivity working fluid in a scheme that offers vastly elevated pressure during forming and curing cycles.

Keywords: thermo-hydroforming, novel manufacturing methods for composite materials

1. Introduction

1.1. Background: identification and significance of the innovation

1.1.1. General information

Sheet hydroforming is a process that was primarily developed for the needs of the aircraft industry. In sheet hydroforming, formed tooling blocks are placed in the machine's loading tray and pre-cut sheet metal blanks are placed over the blocks. Throw pads are then placed over the blanks to cushion sharp edges. The tray is then fed into the pressing chamber as a thick elastic blanket is unrolled over the tool and sheet metal. The pressure chamber is a thick-walled cylinder wound with high tensile strength metal wire that is engineered to handle the extremely high forming pressures. Once the part is loaded, immensely high fluid backfill pressure is applied to the membrane. The elastic blanket diaphragm expands and flows downward, over and around the metal blank. The sheet metal is then pressed to follow the contour of the die block, exerting an even, positive pressure at all contact points. As a result, the metal blank is literally wrapped to the exact shape of the die block. The press is then depressurized for unloading the tray. This process is ideal for prototyping and low volume production in aluminum, titanium, stainless steel, and other aerospace alloys such as matrix metal panels in low volumes [1, 2].

1.2. Customer problem

1.2.1. Automotive

The new fuel economy standards which mandate an average fuel economy of 54.5 miles per gallon for the 2025 model year will highly motivate auto manufacturers to step up development of improved vehicle designs and technologies to sharply improve the fleet mileage. Mass produced models will need to utilize more efficient engines and new lighter but safe car bodies. Automobile manufacturers have investigated alternatives to the steel traditionally used in car production. However, in most cases, the on-road properties of steel make it the best choice for automotive fabrication [3]. As a result, we are seeing a renewed interest in the use of high-strength steel and composites.

Carbon-fiber composite car structures are now in vogue. BMW produces two all carbon electric vehicle designs the i3 and the i8. General Motors' Corvette Stingray has a carbon-fiber roof and hood. Other recent autos that feature carbon-fiber-reinforced polymer (CFRP) components include the Audi R8, the BMW M6, and the Dodge Viper. Most of these models, however, are high end, low-volume vehicles that are mainly assembled manually because composites use in low and medium-priced cars is still awaiting the development of cost effective mass-production processes and materials [4, 5].

1.2.2. Aerospace: NASA general aviation program

The goal of the NASA General Aviation Program is to reduce public travel times by half in 10 years and by two-thirds in 25 years. To accomplish this goal, NASA and its partners are pursuing development of the revolutionary technologies necessary not only to build the next generation of vehicles for business and personal air transportation but also to train the average person to operate them safely. Low cost composite panels are vital to the success of NASA's program which supports electric aircraft and H.R. 1848, "The Small Airplane Revitalization Act" [6–8].

1.3. Modern architecture

The world has recently seen massive advancements in architecture. Numerous buildings in places such as Dubai have advanced the state of the art well beyond previous construction methods. Leading architects such as Frank Gehry, Zaha Hadid, and others are deep in a renaissance of building construction esthetics and methodologies.

Structures fabricated from numerous unique panels are especially well suited to production applications. Computer Aided Design (CAD) software is now used to convert complex 3D geometric forms into numerous 3D architectural SIP (Structural Insulated Panels) panels of a manageable size and shape. The panelized surface architecture process can be applied to buildings, sculptures, ships and aircraft [9].

2. Out-of-autoclave (OOA) composites hydroforming approaches

2.1. Out of autoclave sheet composites forming methods

2.1.1. Globe machine manufacturing

The Globe Company (**Figure 1**) now produces a pressurized air driven bladder technology that is used to form body panels for the Chevy Corvette. This process uses 300 psi of air with a 0.5 mm silicone sheet bladder to pressure bag form parts. They are currently supporting volumes of 34,000 vehicles a year [10, 11].

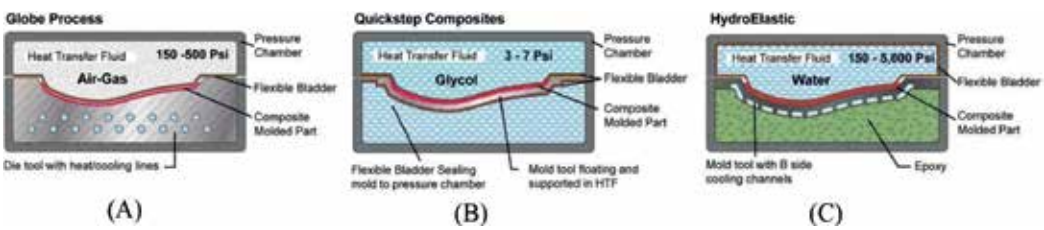

Figure 1. Cross sections of processes: (A) globe manufacturing (left); (B) quickstep composites (middle); (C) hydrothermal hydroforming (right).

2.1.2. Quickstep composites

Quickstep is an Australian-listed company. The Quickstep process forms composite parts using 4 psi (low pressure) on a rigid tool suspended between two elastomeric membranes back filled with glycol fluid. Their large format out of autoclave forming and curing process works well for large parts. Aerospace parts such as wing skins can be molded using either prepreg materials or resin injection molding [12, 13].

2.1.3. Thermo-hydroforming

In this chapter, an "Out of Autoclave (OOA) HydroElastic Hydroforming" method is proposed to utilize pressurized water as a forming fluid behind an elastomeric membrane. The shell tool is water heated and backed by a high strength reusable fiber/epoxy composite [14–24]. In addition to the forming chamber shown, an outer sleeve chamber is used to contain extremely high pressures [25, 26]. Because of this high-pressure capability, the system can simultaneously form laminate stacks of both metal and composite material strata using the OOA hydroforming approach. This opens new potential possibilities for metal [27–32] and fiber reinforced composite flat panel [33–35] as well as contoured part designs [36, 37].

2.2. GLARE® laminate with S-2 glass fiber by AGY

One of the most exciting materials under evaluation for primary and secondary aircraft components is GLARE laminate. Glass Laminate Aluminum Reinforced Epoxy (GLARE) is a sandwich material constructed from alternating layers of aluminum and S-2 Glass® fiber with bond film. The material, developed at Delft University of Technology in the Netherlands, has been recognized as one of the top aerospace materials for the future.

It is believed that thermo-hydroforming has the potential to form GLARE multi-sheet material stacks. This would create a 3D conformal forming process that allows full design engineering of complex 3D shaped parts as needed. The parts are formed in a tool die that allows the part to be configured exactly as needed for the specified function. In addition, thermo-hydroforming forming, will enable subtle surface inflections to be made in parts for things such as flush access doors, flush rivets and flanges as well as embedded cast–forged, electrical or intelligent components.

2.3. Technical objective

This project seeks to gain a foundational understanding of the proposed thermo-hydroforming machine's performance by conducting FEA simulations [38–40]. This simulation studies a multiply coupon of carbon fiber prepreg being formed by a vulcanized silicone elastomeric bladder. The bladder is heated and pressed into the composite coupon by water heated to 285°F under 300 psi of pressure. The tool is pre heated to the temperature of 285°F as well. As a result, the composite coupon is heated from above and below. This process should be used comfortably to 425°F (218°C) and 10,000 psi/700 Bar.

We understand from work by Globe manufacturing, Quickstep Composites and other prior art that both air and fluid heat behind a membrane can be used to react and cure prepreg materials. It is also known that pure water has one of the best thermal conductors. Water

http://dx.doi.org/10.5772/intechopen.81600

has a thermal conductivity that is 24 times greater than that of air and that circulating water increases this effectiveness even further by a factor of 10. Our objective is to study the viability of adopting these methodologies to hydroforming.

Hydroforming has a well-documented history of safely forming sheet metal materials at pressures of up to 20,000 psi (137.89 Mpa) well beyond the requirements of composite materials. Because hydroforming machines can deliver and contain high fluid pressure, it is believed that the addition of a thermal cycle to heat & cool the forming chamber's working fluid will enable a significant industrial advancement in sheet hydroforming machines. The new methodology will allow for a single machine to shape, catalyze and cure prepreg composite materials, thermal plastics and matrix materials in addition to its traditional use as a metal forming machine.

With FEA simulations demonstrated, qualitative assessments can be made to facilitate the future validity for development, implementation and commercialization of thermo-hydroforming machinery.

3. Fluid properties for thermal-hydroforming

Fresh water has a very high level of thermal conductance. It is 100% better than glycerol and 350% better than machine oil. However, in order to be used at high temperature water must be pressurized to prevent boiling. In this design configuration pressure is applied as a part of the process. As a result, at 300 psi water can be used at temperatures of approximately 400°F (**Figures 2** and **3**).

4. FEA simulation: thermal-hydroforming of composites

4.1. Analysis type and geometry

The first load step consists of a linear static analysis where only the pressure load is applied. This allows for the composites to be in contact with the tool. Following this, a transient coupled thermal displacement step is run to obtain the temperature distribution and heat flux through time. Total time used was 200 s.

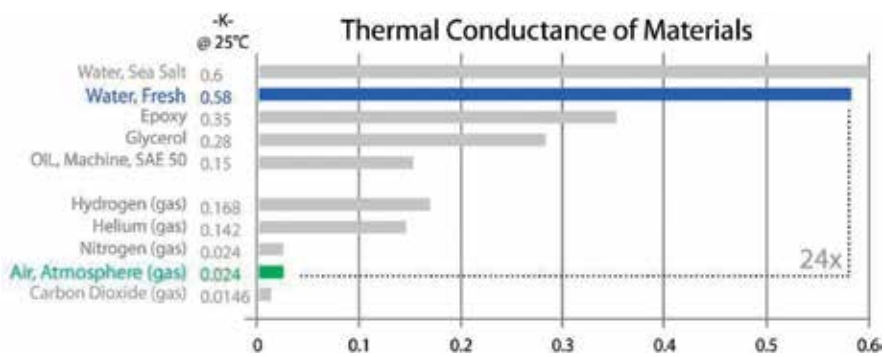

Figure 2. Thermal expansion of select materials.

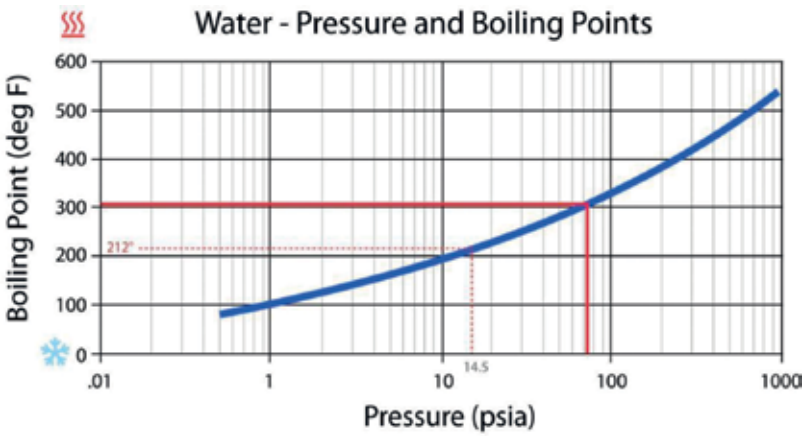

Figure 3. H_2O pressure vs. boiling temperature.

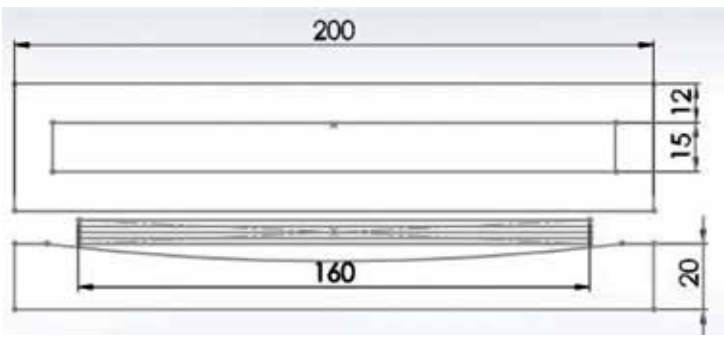

Figure 4. General dimensions of the model.

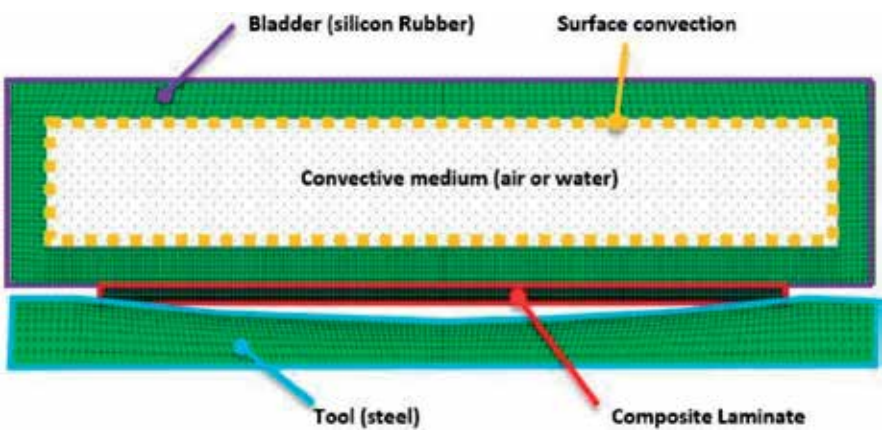

Figure 5. Assigned materials for each component.

The geometry consists of an expandable silicon rubber bladder, which contains a convective medium inside. This convective medium is not modeled, however, the effects of convection on the general temperature distribution are important and therefore, simulated. Two different bladder thicknesses were evaluated: 6 mm and 12 mm. The bladder sits on top of a Torayca 300 carbon/epoxy prepreg laminate consisting of the following stacking order: $(0, -45, 90, 45)_2$. The laminate sits on top of a concave aluminum tool (**Figures 4** and **5**).

4.2. Load steps

a) The rubber bladder at room temperature is pressurized with hot fluid (285°F). The bladder heats up by convection until it reaches thermal equilibrium with the hot fluid.

b) The Rubber bladder expands downward due to the exerted pressure of 300 psi and pushes the composite laminate onto the aluminum tool which is also heated to 285°F.

c) The composite laminate which has a cold OTF (Out of Freezer) temperature of 65°F is heated by the tool and rubber bladder by means of thermal conduction until thermal equilibrium is achieved.

4.3. Thermomechanical properties input

The following mechanical and thermal properties (**Tables 1–3**) of the respective component's material were assigned to the different parts to proceed with the FEA simulations.

4.4. Boundary conditions

Shown in **Figure 6**, the bladder is fixed from the top, to allow the bottom to expand downward, pushing the composites towards the tool. The tool is also fixed so the compressive load is applied to the composites.

4.5. Loading conditions

Shown in **Figure 7**, a uniform pressure of 300 psi was applied to the bottom inner surface, to simulate the bladder expansion which pushes the composite towards the tool. Initial temperatures assigned to the parts were shown in figure.

Material	Elastic modulus (Mpa)	Poisson ratio	Density (Ton/mm^3)
Composite Laminate	135,000	0.3	1.76E-09
Steel	210,000	0.3	7.89E-09
Silicon Rubber	50	0.48	1.70E-09

Table 1. Mechanical properties of assigned materials.

Material	Heat conductivity specific heat	
	Coefficient (mJ/mm K)	(mJ/Ton K)
Composite Laminate	10.46, 7.2, 9	795,000,000
Steel	43	466,000,000
Silicon Rubber	1.375	1,180,000,000

Table 2. Thermal properties of assigned materials.

Material	Convection coefficient (mW/mm² K)	Efficiency
Free air	0.0015	1X
Free water	0.06	40X
Moving water	5.15	3433X

Table 3. Convection coefficients for different liquids.

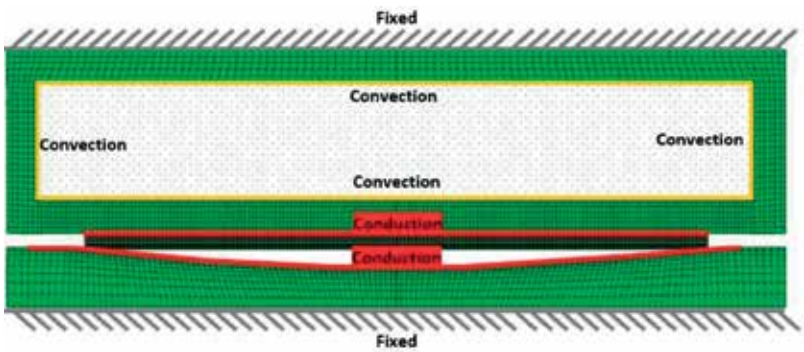

Figure 6. Boundary conditions applied to the model.

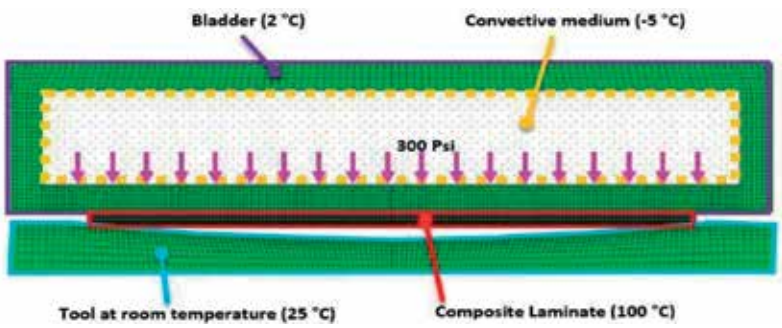

Figure 7. Initial temperatures for each part.

http://dx.doi.org/10.5772/intechopen.81600

4.6. FEA results

4.6.1. Load step 1: bladder heating

During this first load step, thermal conduction between the bladder and the composite laminate is ignored, this allows for the display of the thermal contour of the bladder as it heats up due to convection (**Figures 8–11**).

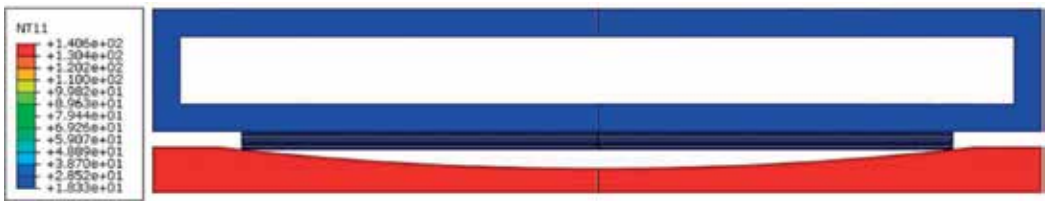

Figure 8. Nodal temperature results at t = 0 s (initial state).

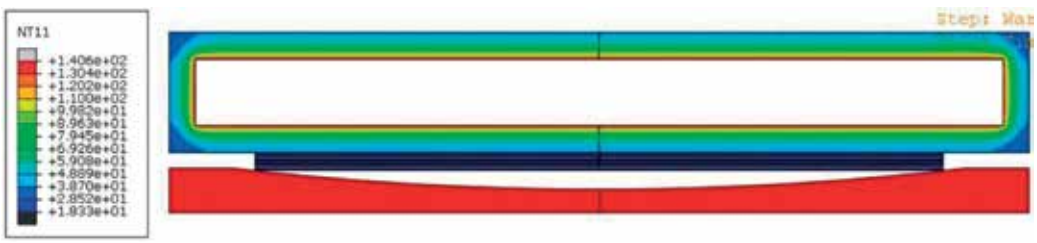

Figure 9. Nodal temperature results at t = 8.38 s.

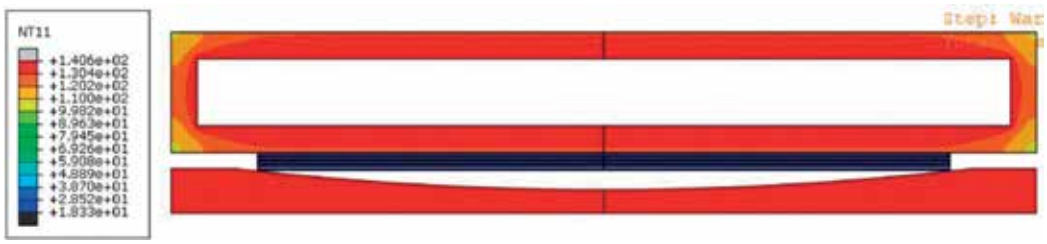

Figure 10. Nodal temperature results at t = 70 s.

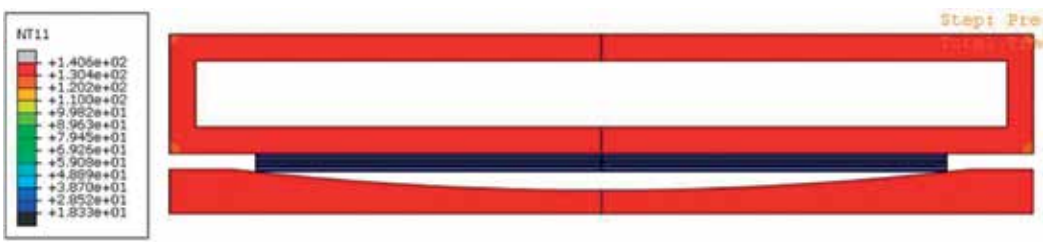

Figure 11. Nodal temperature results at t = 120 s (bladder completely heated up).

4.6.2. Load step 2: bladder expansion

Once the bladder is at operating temperature (285°F), the expansion due to the fluid's pressure is simulated. This makes the bladder expand, which consequently pushes the composite plate towards the concave aluminum tool (**Figure 12**).

4.6.3. Load step 3: curing by thermal conduction

The final load step in the simulation is to enable the thermal conduction between the bladder and the tool towards the cooler composite laminate (**Figures 13–18**).

Additionally, one element per composite layer was probed to analyze its temperature through time. The selected elements were those in the symmetric center of the composite laminate. The same procedure was used for the bladder, to measure the time required for it to reach its working temperature (**Figures 19–23**).

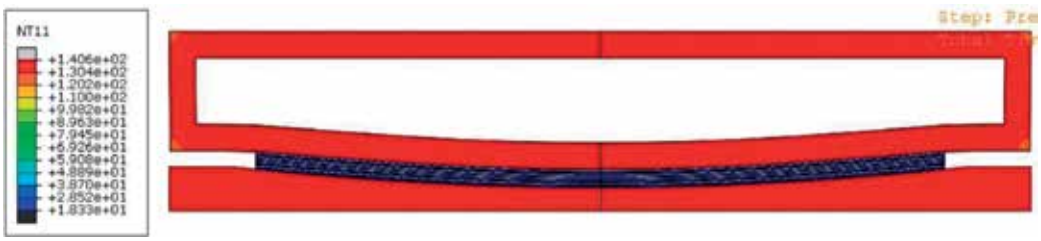

Figure 12. Expanded bladder due to applied pressure of 300 psi (the composite plate and tool are in contact).

Figure 13. Nodal temperature results at t = 120 s (respective to current load step).

Figure 14. Nodal temperature results at t = 130 s, t = 120 s (respective to current load step).

http://dx.doi.org/10.5772/intechopen.81600

Figure 15. Nodal temperature results at t = 147 s (respective to current load step).

Figure 16. Nodal temperature results at t = 274 s (respective to current load step).

Figure 17. Nodal temperature results at t = 338 s (respective to current load step).

Figure 18. Nodal temperature results at t = 438 s (respective to current load step).

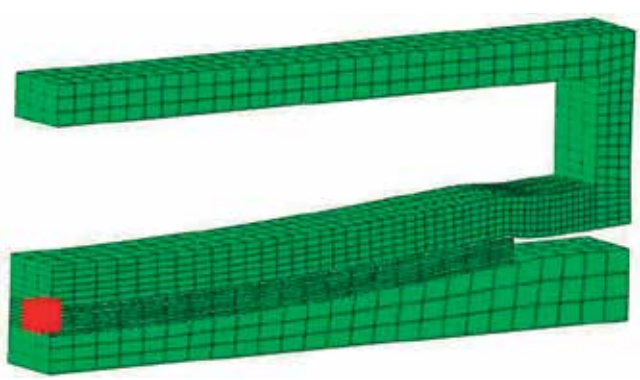

Figure 19. Nodes selected for plotting the temperature gradient throughout the composite material thickness.

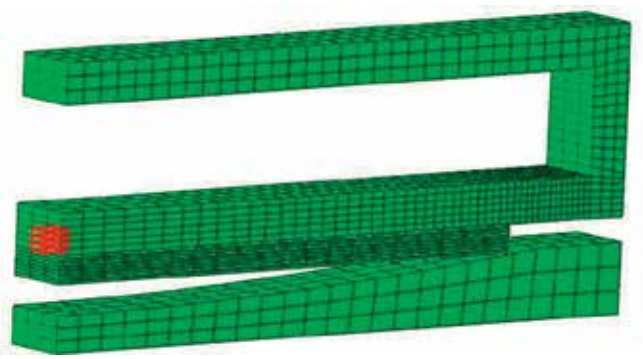

Figure 20. Nodes selected for plotting the temperature gradient throughout the composite material thickness.

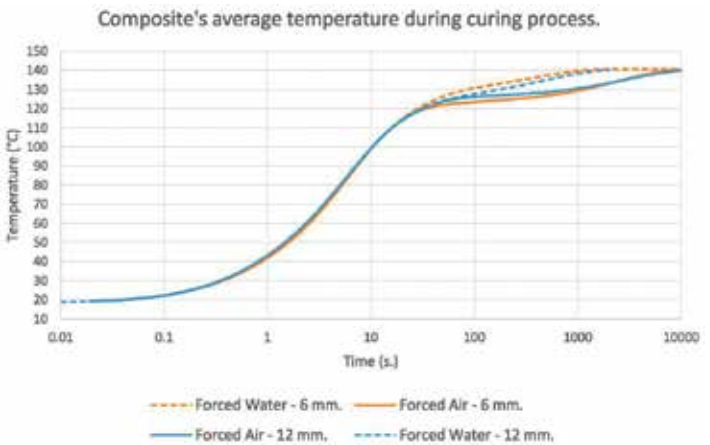

Figure 21. Composite temperature history.

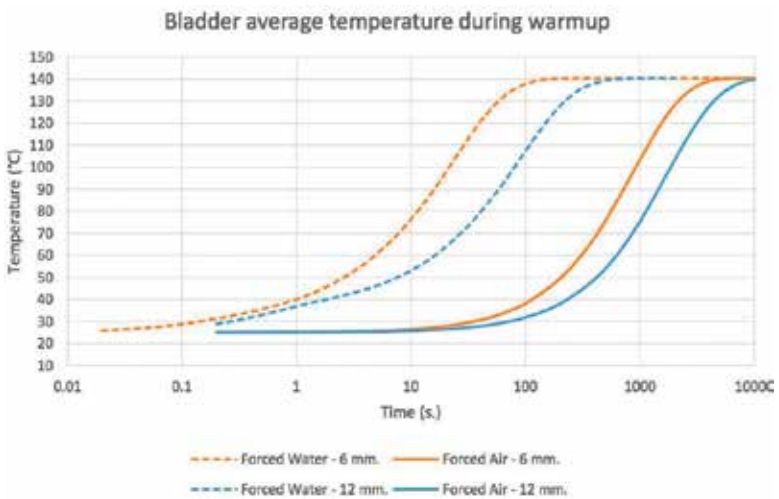

Figure 22. Bladder temperature history.

http://dx.doi.org/10.5772/intechopen.81600

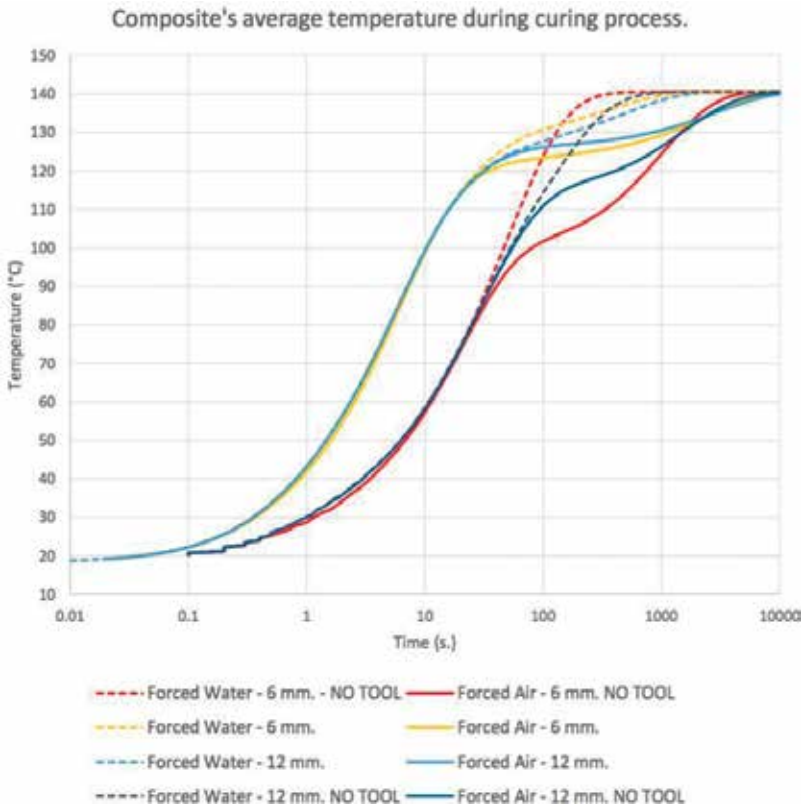

Figure 23. Effect of the aluminum tool on the overall curing process.

5. Conclusions

It can be concluded that both air and water provide similar curing temperatures for the composite laminate, however, the warm-up time is considerably different for the two convective mediums as it can be observed in the above presented results. Air is considerably slower in warming up the silicon bladder up to operating temperature. Once the aluminum tool and the silicon bladder are at operating temperature, the bladder thickness nor the convective medium have much effect on the overall curing process time. It is only until the very end that the different convective mediums display different curing rates.

Based on results of the simulation provided, the use of a snap cure epoxy binder, and an additional 90 second cycle to cool the part; It seems highly probable that parts can be formed in a hydroforming machine in approximately 10 min. With the addition of residual heat in the bladder and some process optimization it may be possible to reduce the actual cycle time 30% further to 7 min. Physical experiments are needed for validation.

A large hydroforming tray bed may be able to form 4–6 parts in one cycle. A 10-min cycle running 4 parts produces a 2.5-min average part cycle time. A 250 days' work year, running a 7-h shift would produce 42,000 parts per year. The envisioned ability to form and cure metal composite laminated parts in one single hydroforming process step has yet to be

physically proven, but based on simulations it is highly promising. More in-depth study and physical models will be required to fully validate the process. However, based on the initial work completed, it seems viable to project, that a hydroforming machine can be used to form composite parts.

It also seems viable that a hydroforming machine is well suited to accommodate the high pressures required by some snap-cure resins such as HexPly M77. This particular resin requires a pressure of 80 bar (1160 psi). Over a large wide surface area, 80 bar will generate significant force. However, hydroforming machine are designed for much greater loads and would easily accommodate the level of pressure. The ability to co-form metal alloys and composite materials seems to be viable and is believed to be a topic worthy of additional study.

Vehicles produced for H.R. 4013 (IH)—Low Volume Motor Vehicle Manufacturers Act of 2014, 2025 CAFÉ Corporate Average Fuel Economy mpg target of 54.5 and the needs of General Aviation, advancement especially electric aircraft may attain benefits from this study.

6. Potential future opportunities

6.1. Unique industry applications and possible advancements resulting from concept development

- Typology Optimized Structural Sandwich Panels (SSP)
- SSP Panels and skin panels with embedded electrical circuits, sensors, induction fields
- SHM Structural Health Monitoring of panels
- Heating from above and below accommodates use of panel cores with insulating properties such as porous media, foams gels and ceramics
- 3D structural battery or structural capacitor skin panels
- Power and communications integral to panels
- Induction field-based panel warping
- Induction field based electromagnetic lock downs and energy pick up
- Large area pressure sensitive/pressure monitoring panels or tiles
- Embedded surface heating for de-icing
- Damaged Part and Part Deflection Detection/SHM Structural Health Monitoring
- Insertion of “Heavy Inserts” such as ceramics, castings, forgings or computers
- Large 3D conformal structural storage tanks for liquid or air-gas fuel
- Electric vehicles, electric aircraft, robotics
- Integration of EAP (Electroactive Polymer) into skin panels

6.2. Electroactive polymer (EAP)

Electroactive Polymer (EAP) is a polymer that exhibits a change in size or shape when stimulated by an electric field. The field generates coulomb attractive forces on the electrodes that apply compressive forces on the dielectric causing the change in size or shape. There are three primary types of EAP: Ionic, Piezoelectric and Dielectric. EAP can be used to create a variety of devices including sensors, actuators, and energy harvesting devices. Inclusion of EAP into composites laminate sandwich panels may have potential for a few excellent features such as vibratory deicing or wing warping.

Author details

Bo C. Jin[1]*, Xiaochen Li[1], Karl Neidert[2] and Michael Ellis[3]

*Address all correspondence to: bochengj@usc.edu

1 Research Scientist, Aerospace and Mechanical Engineering, University of Southern California, California, United States

2 Patent Attorney, Karl Neidert and Associates, CA, United States

3 CTO, Ellis Industrial Design, San Diego, CA, United States

References

[1] Enprotech Hydroforming. http://www.enpromech.com/hydroforming-fluid-cell/

[2] Triform Hydroforming http://www.triformpress.com/?gclid=COel8ZXM7cYCFY17fgodXEIKhQ

[3] Grelling Keane. http://www.bloomberg.com/news/articles/2011-0729/automakers-agree-to-54-5-mpg-u-s-fuel-economy-rule-obama-says

[4] Composites World. http://www.compositesworld.com/blog/post/in-new-corvette-stingrayanother-step-forward-for-composites

[5] Plasan Carbon Composites Corvette Marketing Materials http://plasancarbon.com

[6] Conner, Monroe. http://www.nasa.gov/centers/armstrong/Features/leaptech.html

[7] Kim HD, Brown GV and Felder JL. NASA Glenn Research Center Cleveland Ohio: Distributed Turboelectric Propulsion for Hybrid Wing Body Aircraft; 2008 July 24

[8] Rep. Pompeo, Mike. https://www.congress.gov/bill/113th-congress/house-bill/1848; 2013, May 7

[9] Eigensatz M, Kilian M, Schiftner A, Mitra NJ, Pottmann H, Pauly M, Evolute Software. 2010. http://www.evolute.at/software-en/evolutetools-for-rhino, http://vecg.cs.ucl.ac.uk/Projects/SmartGeometry/paneling/paper_docs/panelization_sigg10_small.pdf

[10] US 20140134382 A1, Ronald M. JACOBSEN. Thermal Processing and Consolidation System and Method, Globe Machine Manufacturing Company; May 15, 2014

[11] US8650745 B2 Ronald M. JACOBSEN. Thermal Processing and Consolidation System and Method, Globe Machine Manufacturing Company; Feb 18, 2014

[12] US 7497981 B2 Neil Graham. Composite and Metal Component Production, Forming and Bonding System; Mar 3, 2009

[13] US8580176 - Q/S Neil Graham. Systeme de liaison, de formation et de production de composite et de composant metallique; Aug 1, 2002

[14] Jin B, Pelegri A. Three-dimensional numerical simulation of random fiber composites with high aspect ratio and high volume fraction. Journal of Engineering Materials and Technology. 2011;**133**:41014

[15] Jin B, Li X, Jain A, Carlos G, LLorca J, Nutt S. Optimization of microstructure and mechanical properties of composite oriented strand board from reused prepreg. Journal of Composite Structures. 2017;**174**:389-398

[16] Wu M, Jin B, Nutt S. Processing and performance of recyclable composites for wind turbine blades. Advanced Manufacturing: Polymer & Composites Science. 2019;**12**:12-28

[17] Jin B, Li X, Jain A, Wu M, Mier R, Herraez M, et al. Mechanical properties and finite element analysis of reused UD carbon fiber/epoxy OoA VBO composite oriented strand board. In: Proceedings of SAMPE 2016; Long Beach. 2016

[18] Jin B, Li X, Wu M, Jain A, Jormescu A, Gonzalez C, et al. Nondestructive testing and evaluation of conventional and reused carbon fiber epoxy composites using ultrasonic and stitched micro-CT. In: Proceedings of SAMPE 2016; Long Beach. 2016

[19] Jin B, Li X, Jain A, Wu M, Mier R, Herraez M, et al. Prediction of stiffness of reused carbon fiber/epoxy composite oriented strand board using finite element methodsRecycling Materials & Structures. Feature Article. Society for the Advancement of Material and Process Engineering (SAMPE) Journal. 2017;**53**:32-39

[20] Jin B, Li X, Jain A, Herraez M, Gonzalez C, LLorca J, et al. Development of a finite element model for reused carbon fiber epoxy composite oriented strand board. In: Proceedings of SAMPE 2016; Long Beach. 2016

[21] Jain A, Jin B, Nutt S. Mean field homogenization methods for strand composites. Journal of Composites Part B. 2017;**124**:31-39

[22] Jain A, Jin B, Li X, Nutt S. Stiffness predictions of random chip composites by combining finite element calculations with inclusion based models. In: Proceedings of SAMPE 2016; Long Beach. 2016

[23] Jain A, Jin B, Nutt S. Development of chip composites with improved mechanical performance attributes using hybrid multi-scale modelling methods. In: Proceedings of CAMX 2016; Anaheim. 2016

[24] Jin B. Recent development of reused carbon Fiber reinforced composite oriented Strand boards. In: Chapter of Book: Recent Developments in the Field of Carbon Fibers. Rijeka: Intech Open. DOI: 10.5772/intechopen.71346

[25] Jin B, Mier R, Li X, Neidert K, Nutt S, Ellis M. Design and FEA of a wound composite hydroforming machine under high pressure. In: Proceedings of SAMPE 2015; Baltimore. 2015

[26] Jin B. Sustainable and efficient hydroforming of aerospace composite structures. In: Chapter of Book: Green Sustainable Composites. IntechOpen. In Print

[27] Wu H, Fan G, Jin B, Geng L, Cui X, Huang M. Fabrication and mechanical properties of TiBw/Ti-Ti (Al) laminated composites. Journal of Materials and Design. 2016;**89**:697-702

[28] Wu H, Fan G, Jin B, Geng L, Cui X, Huang M, et al. Enhanced fracture toughness of TiBw/Ti3Al composites with a layered reinforcement distribution. Journal of Materials Science and Engineering: A. 2016;**670**:233-239

[29] Wu H, Jin B, Geng L, Fan G, Cui X, Huang M, et al. Ductile-phase toughening in TiBw/Ti-Ti3Al metallic-intermetallic laminate composites. Journal of Metallurgical and Materials Transactions A. 2015;**46**:3803-3807

[30] Chen Z, Huang T, Jin B, Hu J, Lu H, Nutt S. High yield synthesis of single-layer graphene microsheets with dimensional control. Journal of Carbon. 2014;**68**:167-174

[31] Huang T, Li T, Xin Y, Jin B, Chen Z, Su C, et al. Preparation and utility of a self-lubricating and anti-wear graphene oxide nano-polytetrafluoroethylene hybrid. Journal of RSC Advances. 2014;**4**:19814

[32] Huang T, Jin B, Li X, Li T, Nutt S. Experimental and finite element analysis study of load carrying capacity of modified polyimide. In: Proceedings of SAMPE 2013; Wichita. 2013

[33] Jin L, Jin B, Kar N, Nutt S, Sun B, Gu B. Tension-tension fatigue behavior of layer-to-layer 3D angle-interlock woven composites. Journal of Materials Chemistry and Physics. 2013; **140**:183-190

[34] Jin L, Niu Z, Jin B, Sun B, Gu B. Comparisons of static bending and fatigue damage between 3D angle-interlock and 3D orthogonal woven composites. Journal of Reinforced Plastics and Composites. 2012;**31**(14):935-945

[35] Ma Q, Wang K, Wang S, Liu H, Jin B, Jin L. Tensile damage mechanism of 3-D angle-interlock woven composites using acoustic emission events monitoring. Autex Research Journal. 2018;**18**(1):46-50

[36] Jin B, Li X, Mier R, Pun A, Joshi S, Nutt S. Parametric modeling, higher order FEA and experimental investigation of hat-stiffened composite panels. Journal of Composite Structures. 2015;**128**:207-220

[37] Jin B, Joshi S, Pun A, Nutt S. Design sensitivity of hat-stiffened composite panels. In: Proceedings of American Society for Composites Conference 2014; San Diego. 2014

[38] Wu H, Xu W, Shan D, Jin B. An extended GRN model for low stress triaxiality and application in spinning forming. Journal of Materials Processing Technology. 2019;**263**:112-128

[39] Jin B, Liu W, Patel H, Nutt S. Application of MSC NASTRAN UDS in modeling and analysis of a hybrid composite reinforced conductor core. In: Proceedings of MSC NASTRAN Conference 2013; Los Angeles. 2013

[40] Ma H, Xu W, Jin B, Shan D, Nutt S. Damage evaluation in tube spinnability test with ductile fracture criteria. International Journal of Mechanical Sciences. 2015;**100**:99-111

Chapter 4

Non-Destructive Testing of Low-Velocity Impacted Composite Material Laminates through Ultrasonic Inspection Methods

Tiziana Segreto, Roberto Teti and
Valentina Lopresto

Additional information is available at the end of the chapter

http://dx.doi.org/10.5772/intechopen.80573

Abstract

Low-velocity impact damages in composite material laminates, such as matrix cracks, delaminations and fibre breakage, usually develop inside the material and can be difficult to detect. As these flaws downgrade the structural integrity of the composite, the thorough damage evaluation is essential to assess the impact damage criticality. This chapter focuses on the ultrasonic non-destructive inspection of low-velocity impacted composite laminates for damage estimation and assessment. The impact damage generation mechanisms are described and characterised. Ultrasonic testing methods and their defect detection capabilities are illustrated. Recent research studies on ultrasonic non-destructive evaluation of low-velocity impacted composite materials are presented and discussed.

Keywords: composite materials, low-velocity impact, non-destructive testing, ultrasonic inspection

1. Introduction

Low-velocity impact is one of the most subtle threats to composite materials integrity. Due to the weak bonds between the plies, even small energies imparted by out-of-plane loads can result in hardly detectable damages, such as matrix cracks, delamination and fibre breakage, causing considerable stiffness and strength losses in tension and, especially, in compression and severely reducing the material structural integrity. Generally, the main observable

damage affecting a laminate subjected to low-velocity impact is delamination, mainly responsible for compression strength decay. For this reason, diverse research works have been devoted to the mechanisms of delamination initiation and growth [1–6]. During impact, more than one delamination in the thickness direction generally develops in a composite laminate, depending on the impact energy and the laminate stacking sequence. Hence, it is crucial to understand the mechanisms of impact damage onset and growth in composite laminates.

To date, non-destructive testing (NDT) techniques play a fundamental role in diverse industrial areas (such as aerospace, automotive, naval and sporting goods, etc.) for the detection of defects in composite material components in order to ensure their integrity during both the manufacturing phase and the service life [7]. Many types of NDT methods are used for flaw analysis, including ultrasonic inspection, X-ray, acoustography, shearography, acoustic emission, etc. [8].

Ultrasonic testing is the most widely utilised NDT procedure for the detection of flaws in composite materials, allowing the identification and characterisation of internal and external damages without cutting apart or otherwise altering the composite material. The main advantages of UT NDT include [9]: high penetration capacity, which allows to inspect parts of large size; high sensitivity, permitting to detect extremely small defects; only one surface of the part needs to be accessible for UT testing and no hazards exist for the operator or the test materials. The disadvantages of UT NDT comprise: need for expert operators; difficulty in inspecting rough surfaces with irregular or too small shapes; need for a coupling medium between the UT probe and the test part and reference standards are required for both instrument calibration and defect characterisation.In this chapter, the non-destructive characterisation and assessment of low-velocity impact damage in composite material laminates is investigated through UT inspection. A description of low-velocity impact damage generation and development in composite materials is presented in Section 2. Section 3 gives an overview of the UT testing methods, describing the basic principles, the UT inspection systems, the defect identification capabilities and the UT data representation; moreover, the UT NDT techniques applied to composite materials are illustrated. In the last section, the research studies of the last several years on the detection of defects generated in low-velocity impacted composite materials are presented and discussed.

2. Impact damage in composite materials

By considering that for many composite materials applications, such as body panels of cars, trucks, rail vehicles and aircraft fuselage, the designer of the composite structure must ensure the prevention of penetration by foreign objects of known mass and velocity. Accordingly, the knowledge of penetration energy becomes a critical issue. Moreover, the absorbed energy is a fundamental parameter in impact situations where it is necessary that the mechanical shock is not transferred to the human body, such as in motorcycle helmets and race car frames, with the aim to ensure the driver's safety in case of high-speed crashes. Accordingly, for these applications, laminated composites must be designed to absorb as much as possible the impact energy and to limit the decelerations on the human body.

Due to their brittleness and anisotropy, composite laminates are particularly sensitive to low-velocity impact damage caused by accidental loadings imparted during fabrication or

service. This has led to numerous studies concerning impact dynamics [10–12], mechanisms of failure initiation and propagation [12–15] and correlation between impact energy, damage and residual material properties [2, 9, 12, 16–18].

Delamination is the most important and crucial damage caused by dynamic loading conditions. Matrix cracking consists in cracks that develop in the resin rich areas between two adjacent composite layers. It has been observed that delamination occurs when a threshold energy is reached in presence of matrix cracking [19]. Even if there is a common agreement on the mechanisms of initiation and growth of this failure mode during an impact event, and several research studies are devoted to this topic [15, 20], a general approach to predict the damage mechanisms and interaction in order to prevent catastrophic failures, is absent. The complexity of the stresses in the vicinity of the point of impact complicates the analysis. In [21], it was shown that delamination growth is governed by interlaminar longitudinal shear stress (σ_{13}) and transverse in-plane stress (σ_{22}) in the layer below the delaminated interface and by the interlaminar transverse shear stress (σ_{23}) in the layer above the interface.

A critical aspect of impact damage is the fact that it is difficult to detect by visual inspection: a composite structure can be severely damaged without any external sign. The only external indication of an impact is indentation, that is, the plastic deformation of the laminate surface due to the contact, left by the impactor during the loading phase. This has led to the concept of "barely visible impact damage", usually adopted in the design of aeronautical structures.

2.1. Experimental characterisation of impact damage

A thorough study of the behaviour of composite laminates subjected to dynamic loads, was carried out by [1–6, 12–14], with the aim to understand the complex mechanisms of damage initiation and propagation under low-velocity impact loading. Many parameters are involved in an impact event and the diverse induced damages, together with their interaction, are very complex to investigate. Moreover, there are instances where impact damage, though seriously present inside the material, is barely visible or not at all visible from the outside.

An extensive experimental testing campaign was carried out on different composite material systems by increasing the initial kinetic energy up to the complete material penetration [16]. This allowed the study of the initiation and the propagation of the complex failure modes related to impact damage. The starting point was the study of the load-deflection curves recorded during impact testing for all the different test conditions. From the curves, the relevant impact parameters were obtained: first failure load and energy, maximum load and energy, absorbed and penetration energy. The influence on the impact parameters, exercised by the composite system, the material constituents, the thickness and the laminate stacking sequence as well as the constraint conditions and the tup diameter were evaluated. Destructive and non-destructive testing were applied to investigate the failure modes, and the observed damage was correlated to the relative energies and the other relevant parameters.

Indentation was found to be a function of the impact energy on the basis of the perforation energy. The latter represents the minimum kinetic energy necessary to completely penetrate

the laminate and is evaluated as the area under the complete load-displacement curve at penetration [22]. This is a fundamental parameter to be known in order to gather information about the impact energy that causes the loss of material mechanical properties [16, 23].

2.2. Load-displacement curve analysis

The load-displacement curve recorded during experimental impact tests is a fundamental tool to obtain information about the impact response and behaviour of composite material samples or structures under service conditions. Some characteristic points on the recorded curve are correlated with the evolution of the impact damage inside the material. In correspondence of these points, the first failure load and energy, the maximum load and energy, the absorbed and the penetration energy, were calculated. The influence of the thickness, the laminate stacking sequence, the matrix type and content, the fibre type and orientations and the impact conditions (impactor tup, diameter of sample support and load speed) was clearly evidenced by comparing the load-displacement curves obtained under the different test conditions. The examination of the load-displacement curves evidence that, notwithstanding the differences in thickness, material composition and reinforcement architecture, there are typical features common to all composite laminates subjected to impact testing [24]. **Figure 1** shows a schematic view of a typical load-displacement curve with the characteristic points identified by arrows and letters ("a", "b", "c", "d", "e").

In **Figure 2**, four curves from low-velocity impact tests on carbon fibre reinforced polymer (CFRP) laminates with different thicknesses are overlapped: despite the thickness difference, common features can be clearly noted. Up to point "a", the curve shows no evidence of damage developing inside the material. A different behaviour between thin and thick laminates can be observed due to the increase of the initial laminate rigidity with increasing thickness (**Figure 2**). The thinner laminates display a clear non-linear response for very low displacement

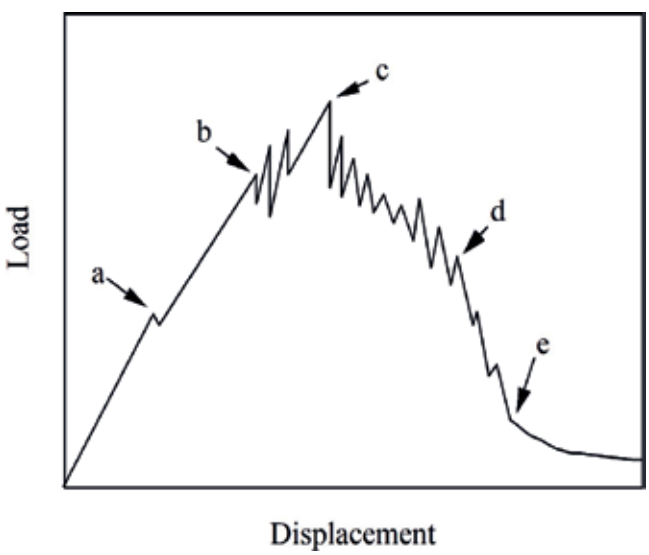

Figure 1. Schematic view of the impact load-displacement curve at penetration.

http://dx.doi.org/10.5772/intechopen.80573

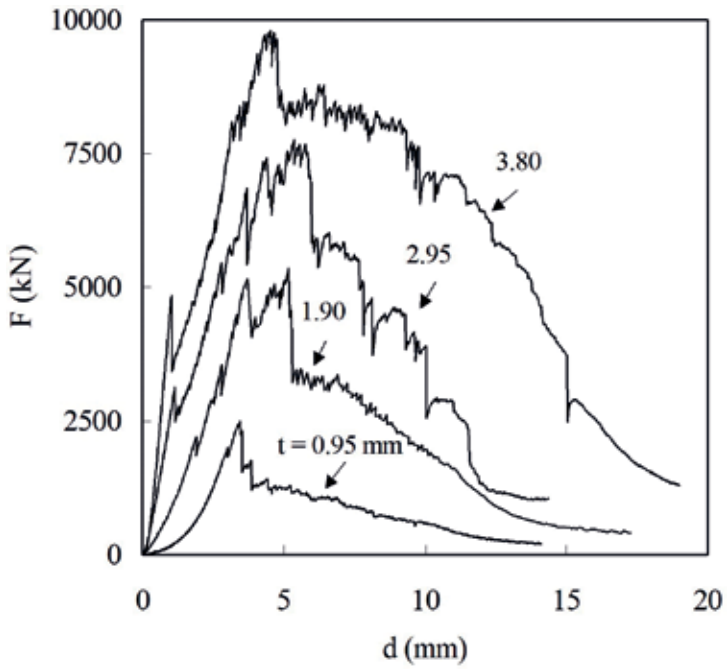

Figure 2. Load, F, versus displacement, d, curves for different CFRP laminate thickness, t.

values, due to the larger amount of displacement at low impact force in comparison with the thicker laminates [25]. At the end of the elastic phase, a load drop occurs, the more clearly when the material thickness is sufficiently high (point "a" in **Figure 1**). This behaviour is difficult to appreciate for the lowest thickness where the load remains substantially constant with increasing displacement or a different slope is evidenced. However, in both cases, a local rigidity variation happens, denoting damage in the laminate.

The successive load drop is an indication of fibre breakage and/or damage propagation in the form of matrix cracking, delamination, fibre breakage, fibre/matrix debonding and fibre pull out (point "b" on the curve). Matrix cracking in the resin pockets are the first type of damage developed during an impact [25] and the presence of matrix cracks does not affect the overall laminate stiffness [26]. However, matrix cracks represent the initiation point for delamination [4, 21] and fibre breakage which dramatically change the stiffness of the composite laminate [27]. All the energy exceeding the one necessary for these damage initiation phenomena is employed for damage propagation. After the first failure, the load increases again, although the laminate rigidity is reduced. Then, a series of load drops are noted, resulting in oscillations in the force-displacement curve, which correspond to extensive propagation of failures of fibres and in the resin through-the-thickness. In the range from points "b" to "d" (**Figure 1**), the different damages propagate through all the layers, until the complete perforation is achieved (point "d"). The slope of the load-displacement curve begins to rapidly decrease when composite material perforation occurs. The maximum force (point "c") is generally achieved between points "b" and "d", even for the thicker laminates (12 layers or more); point "b" is often found coincident with point "d", which means that the first significant fibre failure frequently occurs at maximum force [24].

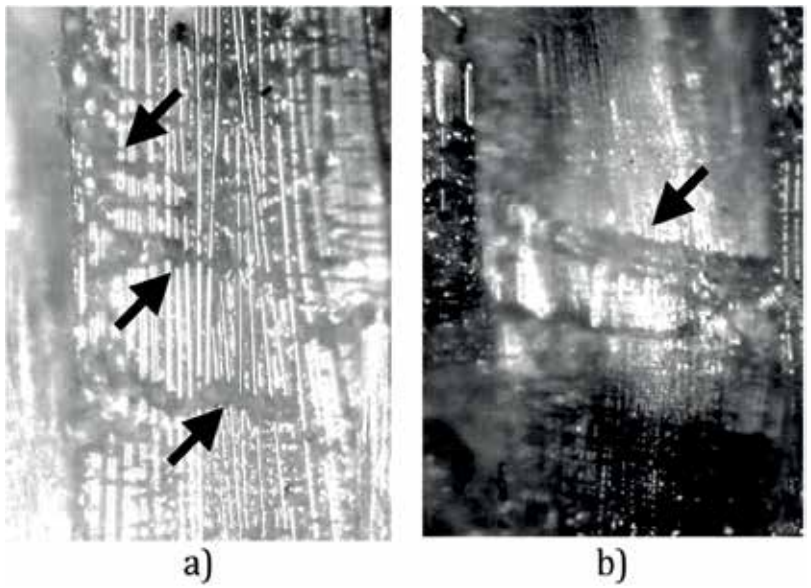

Figure 3. Fibre failures indicated by the black arrows.

In **Figure 3**, examples of fibre failures are shown. The decrease in contact load between points "d" and "e" corresponds to the penetration process. Finally, beyond point "e", the contact load decreases slowly: the cylindrical body of the impactor slides through the penetrated sample. The penetration energy necessary to completely penetrate the laminate, given by the area under the load-displacement curve at penetration, is conventionally calculated at point "e". Both **Figures 1** and **2** refer to impact test cases where complete perforation occurred. In case of non-perforating impacts, during the loading phase the maximum displacement is reached and then the displacement decreases during unloading (**Figure 4**). After the first load drop (arrows in **Figure 4**), the unloading part is different from the loading one since a fraction of the energy is stored in the material for damage formation.

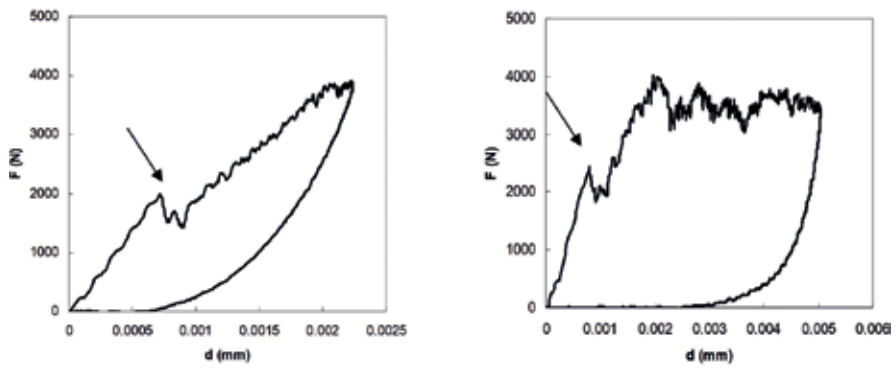

Figure 4. Load-displacement curves for a not penetrated CFRP laminate (t = 3 mm): (a) impact energy level U = 5 J; (b) impact energy level U = 15 J.

http://dx.doi.org/10.5772/intechopen.80573

In [5], it was demonstrated that an interaction between matrix cracking and delamination initiation exists. Delamination propagation starting from intralaminar cracks was found mainly in thin laminates [5, 28] where the membrane contribution is important. In **Figure 5**, low (a) and high (b) magnification micrographs of dynamically loaded CFRP samples are reported showing matrix cracks and delamination starting from the cracks in the resin pocket and connected by intralaminar cracks [5].

As found in several research works by different authors [6, 21], the evolution of damage in a composite laminate subjected to a concentrated dynamic load is driven by intralaminar tensile and shear cracks occurring in the layers farther from and nearer to the contact point. From these cracks, delaminations were found to be generated at interfaces between differently oriented plies, mainly propagating in the direction of the fibres in the lower ply and extending the more sideways with respect to the contact point.

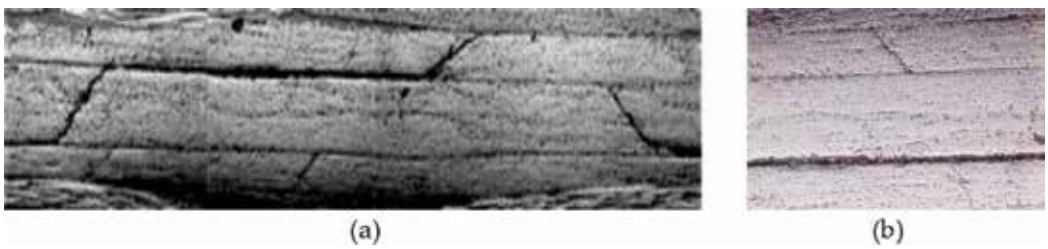

Figure 5. Low (a) and high (b) magnification micrographs of dynamically loaded CFRP laminate with thickness t = 2 mm.

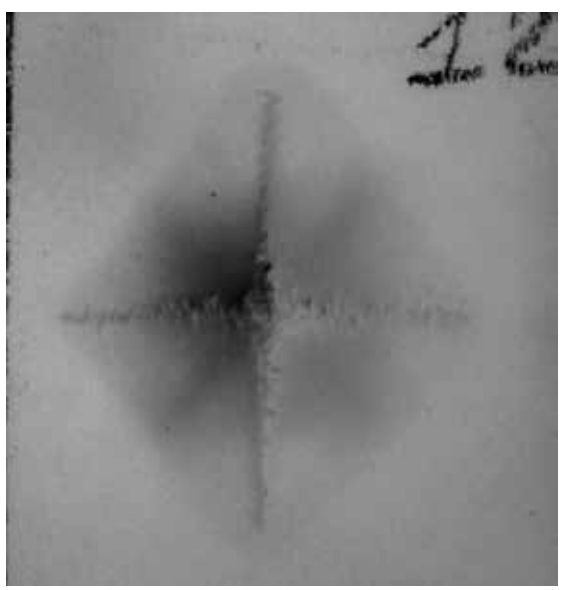

Figure 6. Typical damage zone after impact (back laminate surface). Laminate thickness t = 1.92 mm. Impact energy U = 15.8 J.

A different behaviour is noted for thin and for thick laminates. In thin laminates, bending stresses are more important whereas shear stresses predominate in thick laminates and delaminations without evidence of intralaminar cracks were found at mid-thickness.

In **Figure 6**, a typical impact damage, visually observed on to the back surface of the impacted laminate, is reported, where the classical visible diamond-shaped delaminated area has attained its maximum size. The delamination axes coincide with the warp-weft fibre directions of the surface fabric layer.

3. Ultrasonic non-destructive testing

During World War I, underwater detection systems using high-frequency acoustic waves and quartz resonators for submarine detection were developed by Langevin [29] as a consequence to the tragic sinking of the Titanic in 1912. In 1928, Sergei Y. Sokolov proposed the use of a through-transmission UT technique for flaw detection in metals [30]. Mulhauser firstly patented an UT device employing separate transmitter and receiver transducers to detect flaws in solids [29]. In 1940, Firestone was the first to realise the UT reflection or pulse-echo technique [31]. In 1948, extensive study of UT medical imaging started in the United States and Japan. One of the first UT testing apparatuses using piezoelectric crystal transducers for the detection of defects was patented by McNulty in 1962. This apparatus was capable of isolating defect signals from high level noise signals and providing an alarm upon occurrence of a defect signal [32]. Since those times, technology improvements led to remarkably enhanced UT non-destructive testing (NDT) allowing to detect surface, subsurface and internal flaws (cracks, delaminations, cavities, pores, inclusions and fractures) in diverse types of materials (metals, composite materials and plastics) [33]. In the manufacturing industries, UT NDT techniques are widely applied for the quality control of components and structures as well as for the characterisation of materials.

3.1. Basic principles

UT NDT is based on the measurement of the energy variations associated with mechanical waves, with frequencies ranging between 50 kHz and 25 MHz, generated by a piezoelectric transducer. The UT beams are introduced into the material by a coupling medium (oil, grease and water) and the variations of the reflected and/or transmitted UT energy are used to identify defects within the material which represent discontinuities in the UT path. When an atomic or molecular particle is displaced from its equilibrium position due to UT waves propagation in the material, the internal (interatomic or intermolecular) forces tend to bring it back to its original position. The displacement of a particle causes the dislocation of those placed in the neighbourhood, and thus the propagation of the UT waves in all the material is determined [8, 34].

In **Figure 7**, the basic parameters of a continuous UT wave are shown. The distance between two consecutive peaks of an UT wave is the wavelength, λ, while the number of UT oscillations per unit time is the frequency, f. The time required to complete a full cycle is the period T. The relation between frequency and period in a continuous wave is given by:

http://dx.doi.org/10.5772/intechopen.80573

$$f = \frac{1}{T} \tag{1}$$

UT velocity, v, in a perfectly elastic material at a given temperature and pressure is constant. The relationship between v, f and λ is given by Eqs. (2) and (3).

$$\lambda = \frac{v}{f} \tag{2}$$

$$\lambda = vT \tag{3}$$

In UT NDT, the shorter wavelength resulting from an increase in frequency will usually provide for the capability to detect smaller discontinuities. As a general rule, a discontinuity must be larger than one-half the wavelength in order to be detected.Based on the particle displacement mode, UT waves are classified as longitudinal, shear, surface, and Lamb waves. Longitudinal waves are compressional waves where the particle motion is parallel to the propagation direction of the wave. Shear waves are present when the oscillation direction is perpendicular to the propagation direction. Surface (Rayleigh) waves have an elliptical particle motion and travel across the surface following the profile of the material. Plate (Lamb) waves have a complex vibration occurring in materials where the thickness is less than the wavelength of the UT waves introduced into it.

UT propagation velocity in a medium and UT wave attenuation (loss of amplitude and energy) depend on the medium itself. In solids, the velocity of longitudinal waves, V_L, is given by:

$$V_L = \sqrt{\frac{E(1-v)}{\rho(1+v)(1-2v)}} \tag{4}$$

where E = Young's modulus; ν = Poisson's ratio; ϱ = density of the material.

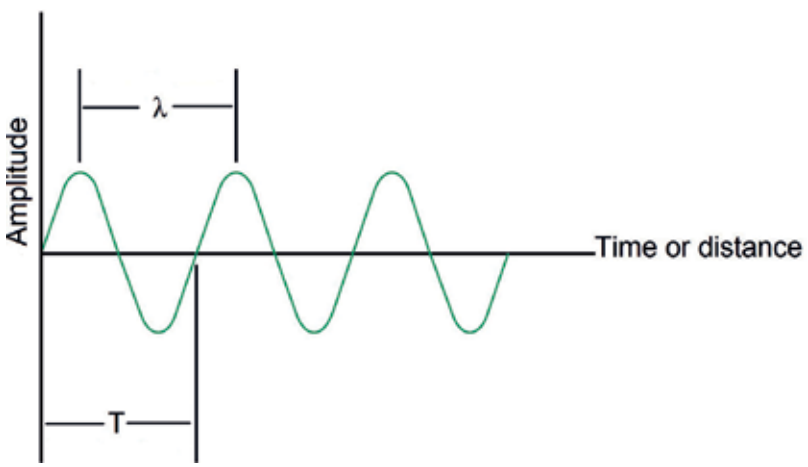

Figure 7. Basic parameters of an UT wave.

The speed of transverse (or shear) waves, V_T, depends on the shear deformation under shear stress (shear modulus) and the density of the medium, defined by the following formula:

$$V_T = \sqrt{\frac{G}{\rho}} \tag{5}$$

where G = shear modulus of elasticity.

In isotropic materials, the elastic constants are the same for all directions within the material. However, most materials are anisotropic and the elastic constants differ with each direction.

ASTM E494 - 15: "Standard Practice for Measuring Ultrasonic Velocity in Materials" covers a test procedure for measuring UT velocity in materials with conventional UT pulse-echo flaw detection equipment. In this practice, tables with longitudinal and shear velocities are reported for metal and ceramic materials [35].

UT attenuation is the decay rate of the UT wave as it propagates through a material. It is mainly due to absorption (conversion of sound energy into other forms of energy) and scattering (reflection of sound in directions other than the original propagation direction) phenomena. The amount of attenuation through a material is a critical parameter for the selection of the appropriate UT transducer for an application.

3.2. UT inspection system

The basic equipment of an UT inspection system consists of diverse functional units: pulser/receiver, transducer and display devices. A pulser/receiver is an electronic device generating short, high amplitude electric pulses which are converted by the transducer into high-frequency UT energy. The sound energy is introduced into the test material and propagates through the material in the form of UT waves. If there is a discontinuity (e.g. a crack) in the UT wave path, part of the energy is reflected back from the flaw surface. The reflected UT wave signal reaches the transducer which transforms it into an electrical signal that can be recorded and/or displayed on a screen [36].

The control functions associated with the pulser circuit include the pulse length or damping and the pulse energy, whereas the control functions in the receiver phase are related to the refinement, filtering and amplification of the return signals.

Selection of the appropriate UT transducer is the first significant step to be considered for UT inspection of a part. Two main categories of transducer are available: contact and immersion transducers. The first category refers to transducers utilised for direct contact inspections which are generally hand manipulated by a skilled operator. Diverse contact transducers are commercially available and their selection depends on the characteristics of the contact surface and the thickness of the part as well as on the aims of the UT inspection. The most common contact transducers are: flat contact, dual element and angle-beam transducers. Immersion transducers are designed to operate in a liquid environment and consequently are typically utilised inside a water tank or as part of a squirter system for UT NDT scanning applications. These transducers can be equipped with cylindrically or spherically focused lens. A focused transducer has the property to concentrate the sound energy onto a small area in order to improve sensitivity and axial resolution.

http://dx.doi.org/10.5772/intechopen.80573

Two basic quantities are measured in UT testing: the time-of-flight (TOF) corresponding to the amount of time for the sound to travel through the sample, and the amplitude of the received signal. Based on velocity and round trip time-of-flight through the material, the material thickness, S, can be calculated as follows:

$$S = \frac{v\,t_s}{2} \tag{6}$$

where v = material sound velocity; t_s = time-of-flight.

Measurements of the relative change in UT signal amplitude can be used for sizing flaws or measuring the material attenuation properties.

3.3. Variables in UT inspection for defect detection

The major variables to be considered in UT NDT include the characteristics of the utilised UT waves and the proprieties of the part being inspected. UT equipment type and capability interact with these variables; often, different types of equipment need be selected to accomplish different inspection objectives. Generally, a compromise must be made between favourable and adverse effects to achieve an optimum balance and to overcome the limitations imposed by equipment and test material [37].

The frequency of the utilised UT waves affects the inspection capability in several ways:

- Sensitivity, or the capability of an UT inspection system to detect a very small discontinuity, is generally increased by using high frequencies (short wavelengths).
- Resolution, or the ability of the UT system to generate simultaneous and distinct indications from discontinuities located close to each other within the material or located close to the front surface of the part, is directly proportional to the frequency bandwidth and inversely related to the pulse length; resolution usually improves with increasing frequency.
- Penetration, or the maximum depth in a material from which useful indications can be detected, is reduced by the use of high frequencies; this effect is most pronounced in the inspection of metals with coarse grain structure or inhomogeneous materials, such as composites, due to the resultant scattering of the UT waves.
- Beam spread, or the divergence of an UT beam from its central axis, is also affected by frequency: as frequency decreases, the shape of an UT beam increasingly departs from the ideal of zero beam spread. This characteristic is observed at almost all frequencies used in UT inspection. Other factors, such as transducer diameter and the use of focusing lens, also affect beam spread.

Sensitivity, resolution, penetration and beam spread are largely determined by the selection of the transducer and are only slightly modified by changes in other test variables.

3.4. UT inspection methods and data representation

A first difference between UT inspection techniques can be made with reference to the transducer or probe position [34, 36, 37]:

- Contact technique, where the probe is placed directly on the surface of the part to be examined.
- Immersion technique, where the probe is immersed in a liquid substance that separates it from the part surface.

The main operating techniques of UT NDT are the through-transmission method and the pulse-echo (or reflection) method.

In the through-transmission technique, two probes, positioned at opposite sides with respect to the part, are used: one probe transmits the UT beam into the part and the other probe receives it. A defect, reflecting a part of the incident beam, causes a decrease in the UT energy detected by the receiving probe. The presence of the defect is highlighted by comparing the received signal with a reference signal obtained from a standard, flaw-less sample. In this technique, two opposite surfaces of the part under examination must be accessible to the transducers.

The pulse-echo technique is based on the property of the UT beam to be reflected whenever it encounters a discontinuity or a defect in its path. The amount of reflected energy highly depends on the reflecting surface size, that is, on the dimensions of the encountered discontinuity perpendicularly to the UT beam propagation direction. To perform the test, it is sufficient that only one surface of the part is accessible, since a single probe is used to send the incident UT beam and, at the same time, receive the reflected UT signal. In **Figure 8**, the typical UT waveform generated during UT pulse-echo inspection of a defective part is shown. The UT waveform enters the material and a first echo, called interface or front echo, is visualised. The back echo corresponds to the final (last) surface of the part under examination. If a discontinuity is encountered inside the material, a defect echo is visualised between the front and the back echoes.

Pulse-echo UT inspection can be accomplished with longitudinal, shear, surface or Lamb waves. Straight-beam or angle-beam techniques can be used, depending on the part shape and the inspection objectives. The detected UT data can be analysed to obtain the required information on defect characteristics, such as type, size, location and orientation.

Diverse representations of UT data are available. The most common formats utilised are: A-scan, B-scan, C-scan, D-scan and FV-scan [8, 9, 34, 36, 37].

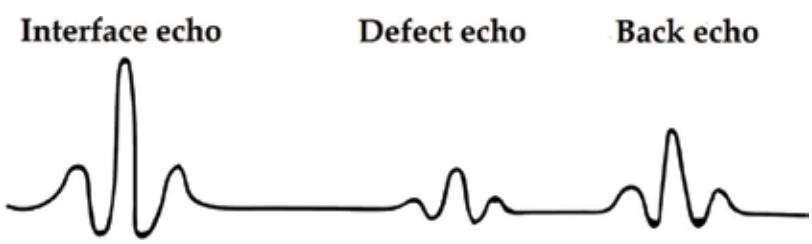

Figure 8. UT waveform generated during UT pulse-echo inspection of a defective part.

- A-scan. It provides a quantitative display of UT signal amplitudes (y axis) and time-of-flight information (x axis) obtained by UT material interrogation at a single point on the part surface. The A-scan can be used to analyse the type, size and location (chiefly depth) of flaws. A discontinuity in the material is indicated by a peak (echo) the distance of which from the zero of the time axis is proportional to the path that the UT beam performs before encountering the discontinuity itself. The amplitude of this defect peak is proportional to the acoustic energy reflected by the discontinuity.
- B-scan. This format provides a quantitative display of time-of-flight data reported along the y axis obtained during a linear scan (x axis) of the part. A B-scan provides information about the part thickness and the depth of a defect for a single plane that normally intersects the part arranged along the scan direction.
- C-scan. A semi-quantitative or quantitative display of UT signal amplitudes obtained over an area of the part surface is represented using a C-scan. The information can be used to map out the position of flaws in an UT image representing the plan view of the part. A C-scan format also records time-of-flight data, which can be converted and displayed by image processing techniques to provide information on flaw depth.
- D-scan. It is similar to a C-scan, but in this case the time-of-flight data obtained over an area of the part is utilised for UT image generation instead of the signal amplitude data.
- FV-scan. Full volume scan (FV-scan), or volumetric scan, is based on the detection and storage of the entire UT waveform in the propagation direction (z-direction) during x-y scanning of the part surface. FV-scan provides for the 2½ D representation of the material internal structure, based on the generation of C-scans at any depth along the z-axis for any portion of the material thickness.

3.5. UT inspection of composite materials

Due to the non-homogeneous and anisotropic nature of composites materials, the frequency range utilised in UT NDT of composites is markedly reduced due to the high damping and attenuation of the high-frequency signals. Usually, the employed frequency in industrial applications is 5 MHz or less, limiting the possibility to detect small flaws. The typical defects present in composite materials are: delamination, cracks, fibre-matrix debonding and fibres fractures [6, 12–15]. Delamination is probably the most investigated failure mode in composite material laminates [1, 4, 5, 16]. During UT NDT of a composite part, the presence of an extended delamination corresponds to a UT waveform with a reduction of the back echo amplitude together with the appearance of a defect echo located at the delamination depth. Other smaller defects such as voids and inclusions cause a loss of the UT back echo amplitude and/or can be weakly reflected [38, 39]. Flaws (e.g. delamination) lying parallel to the surface of the part subjected to UT inspection can be easily detected utilising normal incidence probes, whereas defects (e.g. cracks and fibre fractures) lying perpendicular to the surface are difficult to detect due to their small reflecting surface (this problem can be solved using angle-beam transducers) [40].

By employing UT through-transmission or pulse-echo techniques, it is possible to locate and size the defects based on the measurements of UT signal amplitude and/or time-of-flight.

The pulse-echo technique allows to characterise the matrix material proprieties (volume fraction, moisture content and porosity) of a composite by evaluating the UT velocity and/or attenuation. Knowing the composite thickness, the attenuation coefficient can be evaluated by measuring the amplitude reduction of the multiple back echoes, and the UT velocity by determining the time spacing between them.

A limitation of UT inspection consists of the difficulty to identify defects located very close to the front surface of the part (known as "dead zone") where the pulse length is approximately equal to the time period. This problem can be limited by using shorter pulses or immersion testing procedures. The anisotropic and inhomogeneous properties of composite laminates cause high attenuation of the UT waves, internal UT reflections and UT velocity variations due to the presence of different materials (fibres and matrix) and interfaces (fibre-matrix and inter-ply interfaces).

4. Applications

In the last several years, numerous studies were carried out on the application of UT NDT for defect detection in low-velocity impacted composite material laminates.

In 1998, the estimation of impact induced damage under low-velocity impact (impact energy: from 3 to 30 J) in carbon fibre reinforced polymer (CFRP) laminates was investigated in [41] through UT C-scans using the pulse-echo immersion method. Delamination areas were accurately quantified by processing the UT image data and the correlation between impact energy and delamination extension was established.

In [42], an UT NDT system for delamination evaluation in CFRP, glass fibre reinforced plastic (GFRP) and aramid fibre reinforced plastic (AFRP) laminates subjected to low-velocity impact tests (impact energy: 2, 3, 5 J) is described. The UT NDT analysis was performed using two different probes (5 and 15 MHz) to evaluate the influence of frequency on the reliable evaluation of delamination in these composites. The results confirmed the NDT system capabilities in terms of damage detection, location and evaluation.

In [40], the authors demonstrated that a combination of normal and oblique incidence pulse-echo UT techniques provide highly detailed volumetric images of the damage (matrix cracks and delaminations) induced in composite laminates by low-velocity and low-energy impacts. The tested specimens (quasi-isotropic carbon/polyetheretherketone (PEEK) laminates) were immersed in water and scanned at normal (to detect delaminations) and oblique (to identify matrix cracks) incidence using a focussed broadband transducer (3.2 mm diameter, 18 mm focal length) with a centre frequency of 22 MHz.

A comparative analysis of two different NDT techniques, UT air-coupled C-scan and X-ray radiography, applied to thin carbon/epoxy composite laminates, utilised in naval structures, for the detection of low-energy impact damage was carried out by [43]. The damage area was identified by the two NDT techniques but the UT inspection provided for an easier, faster and more accurate damage characterisation.

In [44], the response of CFRP laminates with different stacking sequences (unidirectional, cross-ply, quasi-isotropic and woven laminates) at low impact velocity and under low-temperature

conditions was examined. Low-velocity impact tests at different temperatures were carried out using an impact energy range from 1 to 13 J. After the impact tests, the damage extension was measured by UT C-scan inspection and the damage mechanisms were studied by optical and scanning electron microscopy. The results showed the influence of temperature, ply reinforcement architecture and stacking sequence on the mechanical behaviour of the CFRP laminates subjected to low-velocity impulsive loads.

A multi-functional non-linear UT testing approach was presented in [45] for in-situ and ex-situ detection of diverse defects (micro-cracking, delamination and disbonding) generated by different damage inducing loads (stress, impact and heat) in CFRP materials and structures for aeronautical applications. The impact tests were conducted using several impact loadings ranging from 4 to 69 J impact energy. The applied UT methodology proved to be a useful tool for the identification of damage for impact energy below 30 J where the visual evidence of damage is lacking.

The effect of temperature on low-velocity impact resistance properties and post-impact flexural performance of CFRP laminates was studied in [46] using UT C-scan and micro-focus X-ray computed tomography. A correlation between the impact temperature and the damage area was validated by the results obtained with the two NDT techniques.

A sparse digital signal model was presented in [47] as an efficient model for the estimation of UT measurements obtained from multi-layered composites. A CFRP laminate with stacking sequence $[0/90]_{4S}$ was impacted in a drop weight tower with 3.8 J impact energy. The laminate was excited by a low-frequency UT sine-burst with central frequency 5 MHz. The UT response signals were utilised for the validation of the developed digital signal model in order to obtain the damage identification. In [48], a multi-level Bayesian method was utilised to identify the through-the-thickness position and the effective mechanical properties of the damaged layers in the same composite laminates using through-transmission UT measurements.

In [49], the authors experimentally tested three composite structures with barely visible impact (BVI) damage and delaminations, using different NDT techniques including UT scanning, piezoelectric sensing, thermography and vibration-based inspection in order to analyse their applicability in the environmental conditions of aircraft elements inspection. The applied UT technique provided a detailed damage evaluation in terms of damage depth, size and location.

Infrared thermography and phased array UT techniques were employed in [50] to detect the impact damage in CFRP composites. Three values of impact energy (18, 29 and 39 J) were chosen for the tests. Both NDT methods presented advantages and limitations. Thermography is fast in detecting the impact damage over large panels, but it is affected by loss of contrast in case of deep defects. The UT technique is more effective in the estimation of thickness and in the inspection of thick parts, but it can be applied only over smooth surfaces and requires a coupling medium.

A laser-ultrasound (LU) scanner was used in [51] to obtain high-quality images of damage in CFRP composites subjected to low-velocity impact with energies 25 and 50 J. X-ray tomograms were also carried out for comparison with the results of the LU study. The high-speed and high-resolution LU scanning method proved to be efficient for in-situ non-contact imaging of the internal materials structure with resolution higher than 1 ply.

In [52], the response to repeated low-velocity impacts was studied for two types of hybrid laminates made of metal and composite layers specifically designed for aircraft structural applications. The damage was evaluated using visual inspection and UT C-scan procedures. Three categories of impact damage were observed: visible deformation without internal or external damage, visible internal damage (C-scan) without external damage and visible internal and external damages.

An UT technique was used in [53] to investigate the delamination caused by low-velocity impact tests on poly(lactic acid)/jute woven fabric composite laminates obtained by conventional film stacking and compression moulding techniques. Square specimens, 100 × 100 mm, were impacted in a falling dart test machine using 5 impact energy values: 2, 5, 10, 12 and 15 J. Delamination damage was evaluated through an UT technique employing a linear phased array probe. The delaminated area was correlated with both the impact energy and the measured indentation depth. The results allowed to identify a threshold energy value beyond which internal damage was detected. Moreover, a linear relationship between delaminated area, energy and indentation depth was found.

A delamination prediction method for composite laminates, utilised for application in unmanned aerial vehicles, subjected to low-energy impact was presented in [54]. UT C-scan tests were carried out with UT beam propagation direction from the bottom laminate surface to the top laminate surface that received the impact. Numerical models were built to simulate the delamination behaviour of the composite laminates, showing a good correlation with the experimental UT results. Delamination prediction can contribute to the evaluation of composite residual strength and the optimization of aircraft structures.

In [55], an UT NDT system was utilised to carry out the metrological characterisation of quadriaxial non-crimp fabric (NCF) CFRP composite laminates subjected to low-velocity impact. The scopes of the UT inspection were thickness estimation, stacking sequence and fibre orientation verification, and composite quality assessment in terms of impact damage development within the whole material volume. The same UT NDT system was considered in [33, 55, 56] for diverse UT testing procedures. **Figure 9** illustrates the specially designed hardware and custom-made software of the UT system operating as follows: the UT oscillator/detector excites the piezoelectric immersion UT probe which is displaced by a 6-axis robotic arm. After interacting with the tested material, the reflected UT pulses return to the oscillator/detector which forwards them to a digital oscilloscope for visualisation and digitisation of the UT waveforms. The digitised UT waveforms are then transferred to a PC where a custom-made software code provides for UT waveform signal storage and analysis.

Low-velocity impact tests were performed on rectangular composite specimens under a falling weight machine using a cylindrical indenter with hemispherical nose at different impact energies: 9, 12, 16, 20, 25, 30 and 40 J.

After impact testing, pulse-echo immersion FV-UT scanning was carried out on the impacted specimens with a focused high-frequency transducer (15 MHz) over a 110 × 155 mm area with scan step 1 mm. The delaminated area was measured through UT image processing. In **Figures 10–12**, four UT images of the impacted quadriaxial laminates are reported for

http://dx.doi.org/10.5772/intechopen.80573

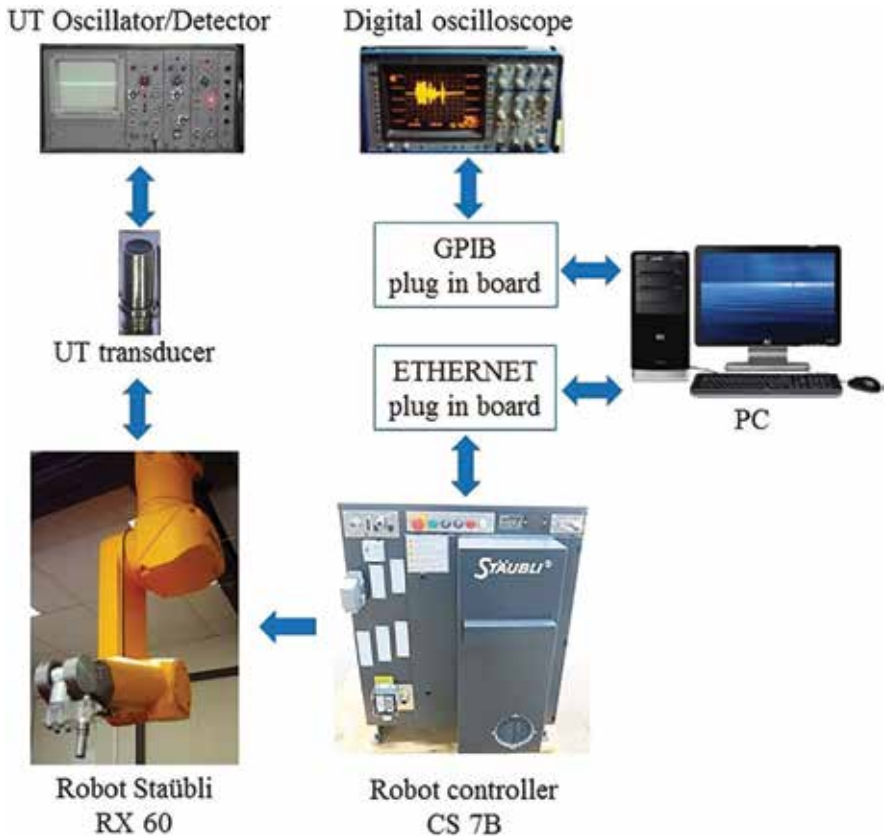

Figure 9. Specially designed UT NDT system.

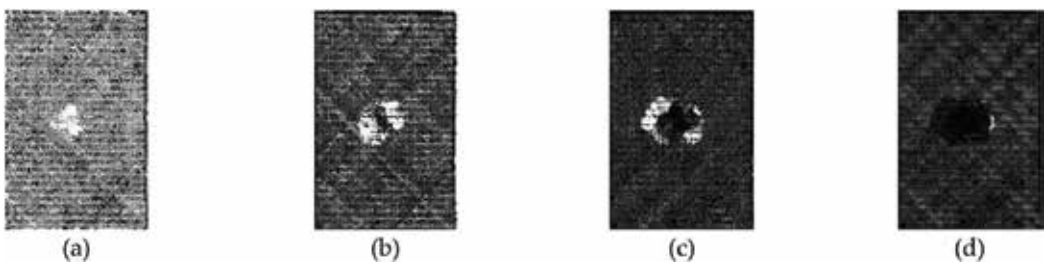

Figure 10. Four UT images for low-energy (9 J) impacted NCF laminate. Each image reports the internal structure of 1 mm thickness from upper (a) to lower laminate surface (d).

drop weight low-velocity impact tests with energy 9, 20 and 40 J, respectively. Each of the four images represents the internal structure of 1/4 (i.e. 1 mm) of the NCF laminate thickness starting from the upper surface (first image on the left) down to the opposite lower surface (last image on the right). In particular, in every figure, image (a) represents the surface damage, images (b) and (c) the internal damage and image (d) the in-plane projection of the total

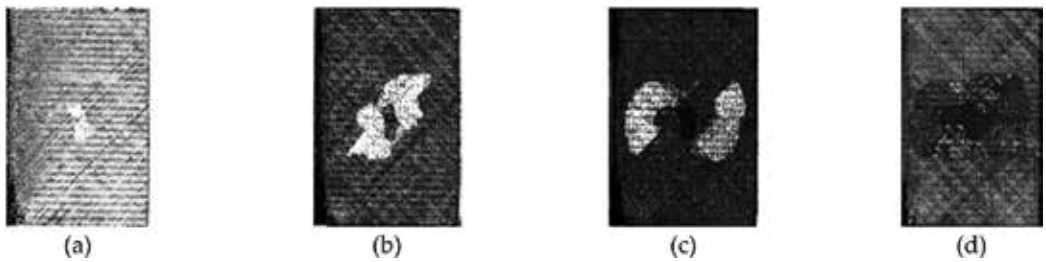

Figure 11. Four UT images for medium energy (20 J) impacted NCF laminate. Each image reports the internal structure of 1 mm thickness from upper (a) to lower laminate surface (d).

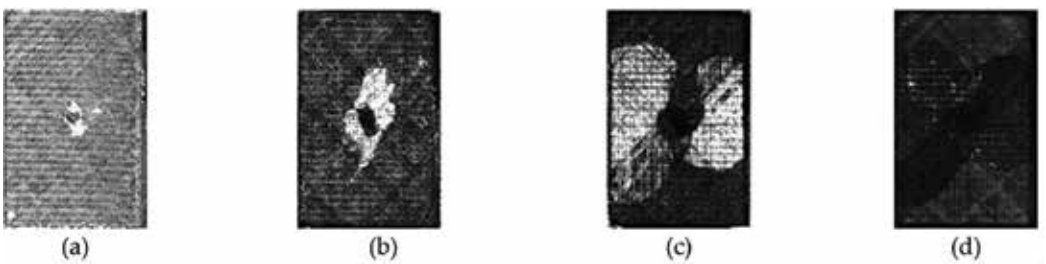

Figure 12. Four UT images for high energy (40 J) impacted NCF laminate. Each image reports the internal structure of 1 mm thickness from upper (a) to lower laminate surface (d).

internal damage. The analysis of the UT images shows that: (i) the impact damage develops differently at interfaces between layers characterised by diverse fibre orientations; (ii) the delamination area increases with rising distance (depth) from the impact surface as well as with growing impact energy and (iii) the delamination outline exhibits the well-known hat-shaped configuration [20]. The UT analysis also reveals the absence of delamination in a small zone directly below the impact surface contact point.

5. Conclusions

In low-velocity impacted composite materials, damages due to this type of loading usually develop inside the material structure and are difficult to detect. Delamination, arising from dynamic loading, is seemingly the most investigated impact failure mode due to its high criticality. However, other damage types such as matrix cracking, fibre-matrix debonding and fibre breakage can also occur due to impact loads. These damage mechanisms can interact with each other and lead to considerable reduction of the load-carrying capability of composite structures. Thus, the thorough material damage characterisation is essential to assess the impact damage criticality. This chapter focussed on the non-destructive characterisation and assessment of low-velocity impact damage in composite material laminates through ultrasonic testing and inspection. A general description of low-velocity impact damage generation in composite materials was presented. Ultrasonic testing methodologies for composite

materials were illustrated and compared in terms of accuracy, resolution and performance. Applications were presented and discussed for industrial areas where composite materials usage is highly relevant.

Author details

Tiziana Segreto[1,2]*, Roberto Teti[1,3] and Valentina Lopresto[3]

*Address all correspondence to: tsegreto@unina.it

1 Fraunhofer Joint Laboratory of Excellence on Advanced Production Technology (Fh-J_LEAPT UniNaples), Naples, Italy

2 Department of Industrial Engineering, University of Naples Federico II, Naples, Italy

3 Department of Chemical, Materials and Industrial Production Engineering, University of Naples Federico II, Naples, Italy

References

[1] Hong S, Liu D. On the relationship between impact energy and delamination area. Experimental Mechanics. 1989:115-120

[2] Cairns DS, Minuet PJ, Abdallah MG. Theoretical and experimental response of composite laminates with delaminations loaded in compression. Composite Structures. 1993;**25**:113-120

[3] Choi HY, Chang FK. A model for predicting damage in graphite/epoxy laminated composites resulting from low-velocity point impact. Journal of Composite Materials. 1992;**26**(14):2134

[4] Liu S, Kutlu Z, Chang FK. Matrix cracking and delamination propagation in laminated composites subjected to transversely concentrated loading. Journal of Composite Materials. 1993;**27**(5):436

[5] Stout MG, Koss DA, Liu C, Idasetima J. Damage development in carbon/epoxy laminates under quasi-static and dynamic loading. Composites Science and Technology. 1999;**59**:2339-2350

[6] Liu S. Quasi impact damage initiation and growth of thick-section and toughened composite materials. International Journal of Solids and Structures. 1994;**31**(22):3079-3098

[7] Castellano A, Fraddosio A, Piccioni MD. Ultrasonic goniometric immersion tests for the characterization of fatigue post-LVI damage induced anisotropy superimposed to the constitutive anisotropy of polymer composites. Composites Part B: Engineering. 2017;**116**:122-136

[8] Gholizadeh S. A review of non-destructive testing me<athods of composite materials. Procedia Structural Integrity. 2016;**1**:50-57. DOI: 10.1016/j.prostr.2016.02.008

[9] Shull PJ. Non-Destructive Evaluation: Theory, Techniques, and Applications. New York: CRC Press, Taylor and Francis Group; 2002

[10] Cairns DS. Simple elasto-plastic contact laws for composites. Journal of Reinforced Plastics and Composites. 1991;**10**(4):423-433

[11] Bucinell RB, Nuismer RJ, Koury JL. Response of composite plates to quasi-static impact events. ASTM STP 1110, TK O'Brien, ed.; 1991. pp. 528-549

[12] Abrate S. Impact on laminated composites: Recent advances. Applied Mechanics Reviews. 1994;**47**(11):517-544

[13] Hull D, Shi YB. Damage mechanism characterisation in composite damage tolerance investigations. Composite Structures. 1993:99-120

[14] Hitchen SA, Kemp RMJ. The effect of stacking sequence on impact damage in a carbon fibre/epoxy composite. Composites. 1995;**26**:207-214

[15] Richardson MOW, Wisheart MJ. Review of low-velocity impact properties of composite materials. Composites Part A Applied Science and Manufacturing. 1996;**27A**:1123-1131

[16] Caprino G. Residual strength prediction of impacted CFRP laminates. Journal of Composite Materials. 1984;**18**:508-518

[17] Cantwell WJ, Morton J. The impact resistance of composite materials - a review. Composites. 1991;**22**(5):347-362

[18] Kim JK, Mackay DB, Mai YW. Drop-weight impact damage tolerance of CFRP with rubber-modified epoxy matrix. Composites. 1993;**24**(6):485-494

[19] Choi HY, Downs RJ, Chang FK. A new approach toward understanding damage mechanisms and mechanics of laminated composites due to low velocity impact: Part I-experiments. Journal of Composite Materials. 1991;**25**:992-1011

[20] Abrate S. Impact on Composite Structures. Cambridge: Cambridge University Press;

[21] Choi HY, Chang FK. A model for predicting damage in graphite/epoxy laminated composites resulting from low-velocity point impact. Journal of Composite Materials. 1992;**26**(14):2134-2169

[22] Caprino G, Lopresto V. The significance of indentation in the inspection of CFRP panels damaged by low-velocity impact. Composites Science and Technology. 2000;**60**:1003-1012

[23] Cantwell WJ, Morton J. Impact perforation of carbon fibre reinforced plastics. Composites Science and Technology. 1990;**38**:119-141

[24] Caprino G, Lopresto V, Scarponi C, Briotti G. Influence of material thickness on the response of carbon-fabric/epoxy panels to low-velocity impact. Composites Science and Technology. 1999;**59**:2279-2286

[25] Caprino G, Langella A, Lopresto V. Elastic behaviour of circular composite plates transversely loaded at the Centre. Composites Part A Applied Science and Manufacturing. 2002;**33**:1191-1197

[26] Sjoblom PO, Hartness TM, Cordell TM. On low-velocity impact testing of composite materials. Journal of Composite Materials. 1998;**22**(1):30-52

[27] Herup EJ, Palazotto AN. Low-velocity impact damage initiation in graphite/epoxy/Nomex honeycomb-sandwiche plates. Composites Science and Technology. 1997;**57**(12):282-289

[28] Hashin Z. Failure criteria of unidirectional fiber composites. Journal of Applied Mechanics. 1975;**47**:329

[29] Graff KF. A history of ultrasonics. In: Physical Acoustics. Vol. XV. NY: Academic Press;

[30] Sokolov S. Phy. Z. 1935;**36**(142) and Techn. Physic USSR 1935;**2**:522

[31] Firestone FA. Patent n. US 2280226A. Flaw Detecting Device and Measuring Instrument

[32] Mcnulty JF. Patent n. US3260105A. Ultrasonic Testing Apparatus and Method; 1962

[33] Segreto T, Caggiano A, Teti R. Quality assurance of brazed copper plates through advanced ultrasonic NDE. Procedia CIRP. 2016;**55**:194-199. DOI: 10.1016/j.procir.2016.08.048

[34] Blitz J, Simpson G. Ultrasonic Methods of Non-Destructive Testing. London, UK: Chapman & Hall; 1995

[35] ASTM. E494-15 Standard Practice for Measuring Ultrasonic Velocity in Materials. PA: West Conshohocken; 2015. DOI: 10.1520/E0494-15

[36] Krautkrämer J, Krautkrämer H. Ultrasonic Testing of Materials. Berlin Heidelberg: Springer-Verlag; 1990. 677 p. DOI: 10.1007/978-3-662-10680-8

[37] Chaplin R. Industrial Ultrasonic Inspection: Levels 1 and 2. Canada: Friesen Press; 2017. 292 p

[38] Teti R. Ultrasonic identification and measurement of defects in composite material laminates. CIRP Annals. 1990;**39**(1):527-530

[39] Summerscales J. Non-Destructive Testing of Fibre-Reinforced Plastics Composites. Vol. 2. Springer Science & Business Media; 1990. 493 p

[40] Aymerich F, Meili S. Ultrasonic evaluation of matrix damage in impacted composite laminates. Composites Part B: Engineering. 2000;**31**(1):1-6. DOI: 10.1016/S1359-8368(99)00067

[41] Hosur MV, Murthy CRL, Ramamurthy TS, Shet A. Estimation of impact-induced damage in CFRR laminates through ultrasonic imaging. NDT and E International. 1998;**31**(5):359-374

[42] Scarponi C, Briotti G. Ultrasonic technique for the evaluation of delaminations on CFRP, GFRP, KFRP composite materials. Composites Part B: Engineering. 2000;**31**(3):237-243

[43] Imielińska K, Castaings M, Wojtyra R, Haras J, LeClezio E, Hosten B. Air-coupled ultrasonic C-scan technique in impact response testing of carbon fibre and hybrid: Glass,

carbon and Kevlar/epoxy composites. Journal of Materials Processing Technology. 2004;**157-158**:513-522

[44] Gómez-del Río T, Zaer R, Barbero E, Navarro C. Damage in CFRPs due to low velocity impact at low temperature. Composites Part B: Engineering. 2005;**36**(1):41-50

[45] Armitage PR, Wright CD. Design, development and testing of multi-functional non-linear ultrasonic instrumentation for the detection of defects and damage in CFRP materials and structures. Composites Science and Technology. 2013;**87**:149-156

[46] Suvarna R, Arumugam V, Bull DJ, Chambers AR, Santulli C. Effect of temperature on low velocity impact damage and post-impact flexural strength of CFRP assessed using ultrasonic C-scan and micro-focus computed tomography. Composites Part B: Engineering. 2014;**66**:58-64. DOI: 10.1016/j.compositesb.2014.04.028

[47] Bochud N, Gomez AM, Rus G, Peinado AM. A sparse digital signal model for ultrasonic nondestructive evaluation of layered materials. Ultrasonics. 2015;**62**:160-173

[48] Chiachío J, Bochud N, Chiachío M, Cantero S, Rus G. A multilevel Bayesian method for ultrasound-based damage identification in composite laminates. Mechanical Systems and Signal Processing. 2017;**88**:462-477. DOI: 10.1016/j.ymssp.2016.09.035

[49] Katunin A, Dragan K, Dziendzikowski M. Damage identification in aircraft composite structures: A case study using various non-destructive testing techniques. Composite Structures. 2015;**127**:1-9. DOI: 10.1016/j.compstruct.2015.02.080

[50] Meola C, Boccardi S, Carlomagno GM, Boffa ND, Monaco E, Ricci F. Nondestructive evaluation of carbon fibre reinforced composites with infrared thermography and ultrasonics. Composite Structures. 2015;**134**:845-853. DOI: 10.1016/j.compstruct.2015.08.119

[51] Pelivanov I, Ambroziński L, Khomenko A, Koricho EG, Cloud GL, Haq M, et al. High resolution imaging of impacted CFRP composites with a fiber-optic laser-ultrasound scanner. Photoacoustics. 2016;**4**(2):55-64. DOI: 10.1016/j.pacs.2016.05.002

[52] Sadighi M, Tooski MY, Alderliesten RC. An experimental study on the low velocity impact resistance of fibre metal laminates under successive impacts with reduced energies. Aerospace Science and Technology. 2017;**67**:54-61. DOI: 10.1016/j.ast.2017.03.042

[53] Papa I, Lopresto V, Simeoli G, Langella A, Russo P. Ultrasonic damage investigation on woven jute/poly (lactic acid) composites subjected to low velocity impact. Composites Part B: Engineering. 2017;**115**:282-288. DOI: 10.1016/j.compositesb.2016.09.076

[54] Wang HR, Long SC, Zhang XQ, Yao XH. Study on the delamination behavior of thick composite laminates under low-energy impact. Composite Structures. 2018;**184**:461-473

[55] Segreto T, Bottillo A, Teti R. Advanced ultrasonic non-destructive evaluation for metrological analysis and quality assessment of impact damaged non-crimp fabric composites. Procedia CIRP. 2016;**41**:1055-1060. DOI: 10.1016/j.procir.2015.12.125

[56] Segreto T, Bottillo A, Caggiano A, Teti R, Ricci F. Full-volume ultrasonic technique for 3D thickness reconstruction of CFRP aeronautical components. Procedia CIRP. 2018;**67**:434-439. DOI: 10.1016/j.procir.2017.12.238

Chapter 5

Drilling of Fiber-Reinforced Composite Materials for Aeronautical Assembly Processes

Alessandra Caggiano, Luigi Nele and Roberto Teti

Additional information is available at the end of the chapter

http://dx.doi.org/10.5772/intechopen.80466

Abstract

Composite materials such as fiber-reinforced plastics (FRP) are increasingly employed in the aeronautical industry, where the reduction of aircraft weight is essential to meet environmental and cost requirements related to lower emissions and fuel consumption. Due to structural requirements, aeronautical assembly processes on FRP components are based on the wide use of mechanical joints such as rivets. As the latter require a former hole making process, drilling is extensively applied to FRP composites in the aeronautical industry. The main challenges in FRP composite drilling are related to rapid tool wear and damage generation which affects material integrity and surface quality, with particular reference to delamination damage generation. In this chapter, case studies of drilling of CFRP/CFRP stacks for aeronautical assembly are presented to investigate and discuss the influence of drilling parameters, tool type and geometry on tool wear development, hole quality and surface integrity, and the opportunity to implement advanced sensor monitoring procedures for tool condition monitoring based on the acquisition and processing of thrust force and torque signals.

Keywords: FRP composite materials, drilling, assembly processes, CFRP/CFRP stacks

1. Introduction

In the aeronautical industry, aircraft weight reduction is essential to meet environmental and cost requirements related to lower emissions and fuel consumption. The use of innovative light-weight materials such as fiber-reinforced plastics (FRP) has then significantly increased in recent aircraft components [1].

The assembly of FRP components for the aeronautical industry is generally performed by means of mechanical joining processes like riveting, which offer higher performance and less challenges compared to welding and adhesive joining techniques. As a consequence, hole making is a central process since a large number of holes is required to allow for riveting of aircraft components. Mechanical drilling using conventional or innovative drill bits is the most commonly employed hole making process for FRP components, although alternative nontraditional machining processes, such as laser and water-jet machining, have been developed in the last years [2, 3].

Despite the large application of FRP mechanical drilling processes, still efforts are required to optimize them since tool wear typically develops very fast, and severe damages can be easily generated on the workpiece, affecting material integrity and surface quality [4–7].

Numerous critical defects such as geometric/dimensional errors, entry/exit delamination, interlaminar delamination, fiber pullout, uncut fibers, spalling, and cracking and thermal damage can be generated by drilling of FRP laminates [8–11]. Drilled holes of low quality result in out-of-tolerance assembly and long-term weakening of structural properties, which are not acceptable in the aeronautical sector. Tight geometrical/dimensional tolerances and surface integrity need to be met as they are a key requirement to guarantee the functionality of the assembled components.

In the last years, several research studies have investigated the role of drilling process parameters, including cutting speed, feed rate, drill bit geometry, and composition, on the output product quality, with particular reference to carbon fiber-reinforced plastic (CFRP) laminates, which are the most commonly utilized in aerospace applications [1, 12].

Different types of tools, distinguished by diverse geometry and material, have been investigated for FRP composite drilling. A complete analysis of delamination produced by drills of different geometry, including traditional twist drills and innovative drills as candle stick drill, saw drill, core drill, and step drill was reported in [13]. To reduce the high wear rate of the sintered carbide drills, TiN and DLC coatings were employed in [14] for drilling of CFRP laminates, studying material damage, thrust force, and torque generated during processing. The experimental results showed that tool wear or damage was not significantly improved by using coatings. In [15], the performance of uncoated and diamond-coated carbide tools was investigated: the diamond coating provided significantly better results achieving a tool life 10–12 times higher than uncoated carbide drills and much higher cutting speeds (170 m/min against 56 m/min).

Drilling of CFRP laminates was also investigated in [16] to identify the most suitable drilling parameters satisfying the hole quality requirements, including surface integrity and roughness, hole roundness and diameter error, showing that the thrust force and the delamination damage were in agreement with the tool wear zones.

The studies in [17] on high speed drilling of CFRP laminates using K20 carbide drill bits under different drilling parameters (spindle speed and feed rate) showed that feed rate has a major influence on thrust force, push-out delamination, and hole diameter, whereas spindle speed is one of the key factors of the drilled hole roundness.

A thorough study on the cutting mechanism and the influence of cutting parameters on delamination in CFRP drilling was presented in [18], showing that thrust force is highly

http://dx.doi.org/10.5772/intechopen.80466

dependent on feed rate because higher feed rates cause greater undeformed chip thickness, while delamination is dependent on both spindle speed and feed, and the effect of feed is amplified at higher spindle speed.

Efforts have also been spent to model the thrust force engaged in drilling, recognized as a major factor affecting the quality of drilled holes [15, 19, 20]. However, modeling was most often limited to drilling of unidirectional laminates with simple geometry drill bits, and complex mathematical relationships were required to fully describe the complex mechanisms occurring during drilling of fiber-reinforced plastic laminates.

In this framework, the aim of this chapter is to investigate more complex industrially relevant FRP drilling processes such as drilling of multidirectional CFRP/CFRP stacks for assembly of aircraft fuselage panels, discussing the employment of innovative procedures based on the multiple sensor process monitoring for cognitive tool wear prediction and hole quality assessment.

2. Drilling of CFRP/CFRP stacks for aeronautical assembly

In the aeronautical industry, in order to assemble two CFRP components, the latter are typically superimposed and then drilled together in a "one-shot" process so as to allow for easier subsequent riveting avoiding misalignment issues. Accordingly, to reproduce the real operating conditions of the aeronautical industry, wide experimental campaigns have been focused on drilling of CFRP/CFRP stacks made by two overlaid CFRP laminates [21–23].

In the following subsections, drilling of CFRP/CFRP stacks for aeronautical assembly is discussed with reference to experimental studies on the influence of drilling parameters, tool type and geometry on tool wear development, hole quality and surface integrity, and the opportunity to implement advanced sensor monitoring procedures for tool condition monitoring based on the acquisition and processing of thrust force and torque signals.

2.1. Tool wear monitoring

In the aeronautical industry, the practice for CFRP/CFRP stack drilling is typically based on manual drilling processes, where tools are replaced largely in advance to avoid any risks of material damage due to early tool failure, since severe geometrical and dimensional tolerances need to be met, and surface integrity is crucial. To fully exploit the entire tool life and increase the productivity of the aeronautical industry through a higher automation of drilling processes able to preserve the integrity of the workpiece, a reliable on-line tool condition monitoring procedure is required [21].

With the aim to perform tool condition monitoring in drilling of CFRP/CFRP stacks, different methodologies have been developed [21, 22, 24]. Such methodologies are based on the employment of multiple sensor monitoring systems for the acquisition of thrust force and torque sensor signals to be used for tool wear estimation. The different procedures of advanced sensor signal processing and feature extraction implemented in the time and frequency domain are described in the following sections. On the basis of the features extracted

from the force and torque sensor signals, it is possible to develop an artificial neural network (ANN)-based cognitive paradigm for pattern recognition with the aim to find correlations between the extracted sensor signal features and tool condition [21, 22, 24].

2.1.1. Analysis of cutting force and torque signals in CFRP/CFRP stack drilling

Advanced methodologies for tool condition monitoring were developed with reference to an extensive experimental campaign of drilling of CFRP/CFRP stacks for aeronautical industry assembly [21–26]. The CFRP/CFRP stacks employed in the tests were made of two superimposed symmetrical and balanced laminates of 5 mm each. The laminates consisted of 26 unidirectional prepreg plies made of Toray T300 carbon fibers and CYCOM 977-2 epoxy matrix, with stacking sequence $[\pm 45_2/0/90_4/0/90/0_2]_s$ and a 0°/90° fiberglass fabric (80 g/m^2) on the top and bottom. Following vacuum bag molding and autoclave curing, the laminates displayed an uneven surface finish on the bag side. To test the hardest condition, as requested by the industry, CFRP/CFRP stack drilling was performed by facing the laminates with their uneven sides [21].

The drilling tests were performed on a CNC drilling center with a 2-flute 6.35 mm diameter with 125° point angle twist drill made of tungsten carbide (WC).

To assess the impact of the cutting parameters on the machinability of the CFRP stack laminates as concern tool wear and hole quality, different cutting conditions were adopted for the experimental drilling tests: feed = 0.11, 0.15, and 0.20 mm/rev; spindle speed = 2700, 6000, and 9000 rpm. For each cutting condition, 60 holes were realized with the same drill bit in order to evaluate the tool wear development.

During the experimental stack drilling tests, a multiple sensor monitoring system was utilized, consisting of a Kistler-9257A piezoelectric dynamometer to acquire the thrust force along the z-direction, Fz, and a Kistler-9277A25 piezoelectric dynamometer to acquire the cutting torque about the z axis, and T. A National Instruments NI USB-6361 DAQ board was employed to digitalize the analogue signals acquired by the force and torque sensors at 10 kS/s.

Figure 1 shows an example of thrust force signal acquired during the CFRP/CFRP drilling tests. Both the force and torque sensor signals displayed high frequency oscillations as those highlighted in **Figure 2**. This characteristic, not observed when drilling homogeneous and isotropic materials, is associated to the anisotropic nature of the CFRP laminates, which exhibit superior mechanical properties along the fiber directions.

As shown in earlier studies on cutting of FRP composites, the fiber orientation with regard to the cutting direction regulates the mechanism of chip formation and the quality of the cut surface [5]. Based on the angle formed between the cutting edge and the carbon fibers, also known as fiber cutting angle, different cutting modes can be identified [27].

In CFRP drilling, the fiber cutting angle changes during a half revolution of the drill, and the interaction mechanism between the tool and the laminate varies accordingly, causing diverse conditions of mechanical loading and resulting surface quality [27]. As a matter of fact, loading is influenced by cutting edge geometry and cutting mode and therefore varies during a drill revolution, as observed in the sensor signals acquired in CFRP drilling, which display high amplitude oscillations.

http://dx.doi.org/10.5772/intechopen.80466

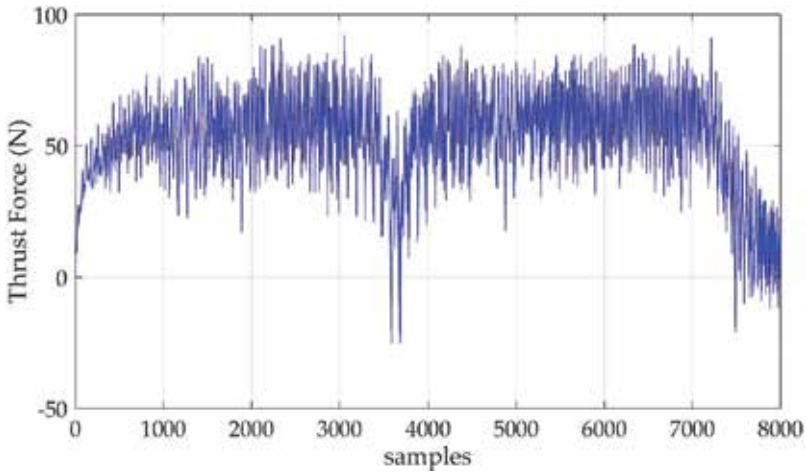

Figure 1. Thrust force sensor signal in CFRP/CFRP stack drilling (6000 rpm–0.15 mm/rev).

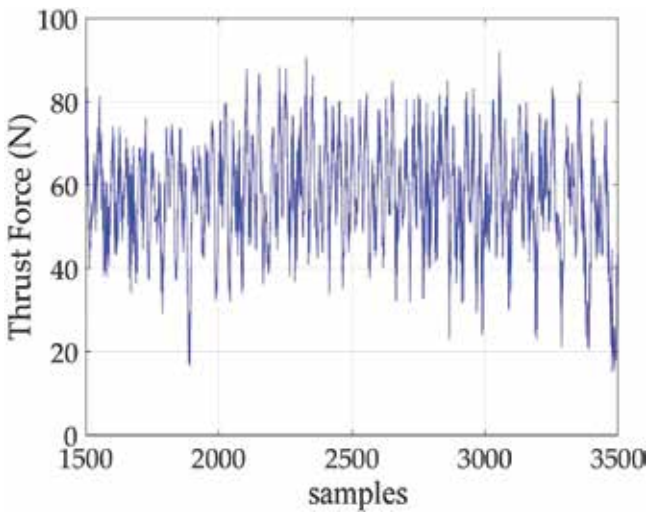

Figure 2. Enlarged thrust force signal: high frequency oscillations (6000 rpm–0.15 mm/rev).

Experimental studies have been performed with the aim to model the relationship between fiber cutting angle and cutting force in drilling of unidirectional CFRP laminates, obtaining the calculation of force coefficients as a sine wave function of 2θ, where θ is the fiber cutting angle [28]. In [27], in order to investigate the effect of local feed force on delamination in drilling of unidirectional CFRP laminates, a model was proposed by resolving cutting forces into steady and transient components, the first associated to the progressive engagement of the cutting edge, and the second associated to the cutting modes. Drilling of multidirectional CFRP laminates is far more complex: different cutting modes take place at the same time along the cutting edge, due to the diverse fiber orientations of the multiple plies simultaneously cut by the drill cutting edge.

Because of the overlap of different cutting modes in both space and time, the high amplitude oscillations that can be observed in the thrust force and torque signals acquired during drilling of the multidirectional CFRP laminates are the sum of multiple waves having a phase difference dependent on the different fiber orientations (e.g., 0, 45, 90, −45°) and having an amplitude related to the number of plies with same fiber orientations concurrently cut by the drill cutting edge.

2.1.2. Sensor signal feature extraction and selection in the frequency domain and neural network pattern recognition for tool wear estimation

With the purpose to explore the complex frequency content of the thrust force and torque sensor signals acquired in the multidirectional CFRP/CFRP stack drilling experimental tests, advanced signal feature extraction in the frequency domain was carried out in [21] with the final objective to find correlations between the extracted frequency domain sensor signal features and the tool wear state. The fast Fourier transform (FFT) algorithm was applied to translate the signals into the frequency domain. Following this transformation, a number of significant peaks were detected at frequencies equal to 1, 2, 3, 4, 5, and 6 times the revolution frequency of the tool. For instance, on the FFT of the thrust force signals acquired in the CFRP/CFRP stack drilling tests carried out at 6000 rpm and 0.15 mm/rev, in which the revolution frequency is 6000 rpm/60 = 100 Hz, the tallest frequency peaks were found at 100, 200, 300, 400, 500, and 600 Hz, that is, 1x-6x the revolution frequency, as visible in **Figure 3**.

As regards the torque signals, the tallest frequency peaks were found at 1x-4x the revolution frequency (100, 200, 300, and 400 Hz).

This seemed to confirm the tight connection between the peaks of the signal frequency transform and the effect of the cutting angle variation during the drilling process due to the several fiber orientations in the multidirectional laminates.

The amplitudes of the identified force and torque frequency peaks with increasing number of holes were investigated, showing a notable growth of some of the peaks, as shown in **Figure 4** with reference to the thrust force signals of the experimental drilling tests carried

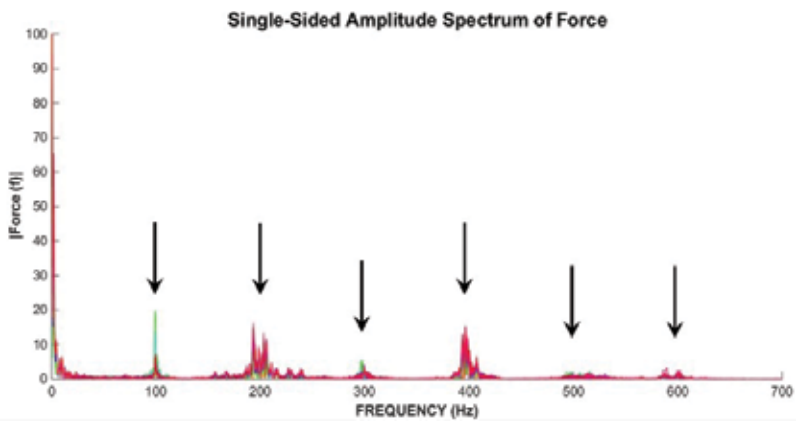

Figure 3. Single-sided amplitude spectrum of thrust force signal (6000 rpm–0.15 mm/rev) [21].

http://dx.doi.org/10.5772/intechopen.80466

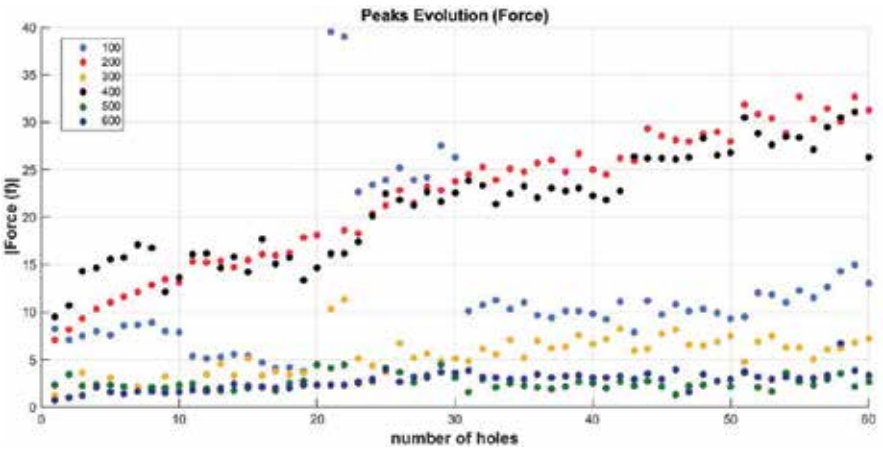

Figure 4. Amplitude of the peaks detected in the frequency transform of the thrust force signal vs. hole number (6000 rpm–0.15 mm/rev) [21].

out at 6000 rpm and 0.15 mm/rev, suggesting a potential correlation of the frequency peak amplitude with tool wear progression.

A statistical feature selection procedure based on the Pearson's correlation coefficient was applied to evaluate the statistical correlation between the extracted features and the output tool flank wear, VB.

Substantial correlations with tool wear state were identified for the following set of features: $Fpeak_{2x,}$ $Fpeak_{4x}$, $Fpeak_{6x}$, $Tpeak_{2x}$, and $Tpeak_{4x}$. The subset composed the first three features extracted from the thrust force signal displayed the highest correlation with tool wear. The selected features were used to build two different feature pattern vectors, FPV_1 and FPV_2, to feed cognitive paradigms for the estimation of tool wear. FPV_1 was made of three features extracted from the thrust force signal, and FPV_2 was a sensor fusion feature pattern vector containing the five features extracted from the thrust force and the torque signals.

The FPVs were fed to three-layer cascade-forward backpropagation artificial neural networks (ANN) to find correlations between the extracted and selected frequency domain sensor signal features and tool wear state through pattern recognition [29]. ANN training was performed using the Levenberg-Marquardt optimization algorithm. Each FPV was associated to its corresponding flank wear (VB) to create input-output vectors for ANN learning. For each drilling condition, 60 input-output vectors (i.e., one for each drilled hole) were built to create the related ANN learning set. Training and testing were performed with different ANN configurations by varying the number of hidden layer nodes. In particular, the number of hidden layer nodes was varied between 3, 6, and 9 for FPV_1 and 5-10-15 for FPV_2, that is, equal to the 1, 2, and 3 times the number of input features.

Cross validation of the NN was carried out by means of the leave-k-out method with $k = 1$. The global pattern recognition performance was evaluated by merging the recognition rates achieved across all trials.

The ANN performance was evaluated in terms of mean square error (MSE), that is, the variance of the differences between the VB values predicted by the ANN and the target VB values. The very low MSE values, between 9.82E-07 and 1.57E-05, confirmed the robust correlation between the sensor signal features extracted in the frequency domain and the tool wear, due to the interaction between the drill bit and the anisotropic CFRP material.

Through pattern recognition based on the frequency domain signal features extracted from the multiple sensor monitoring signals, the ANN accurately reconstructed the tool wear curve. **Figure 5** presents the reconstructed tool wear curve for the drilling test performed at 6000 rpm and 0.11 mm/rev, obtained by applying the leave-k-out method with $k = 1$ to the ANN with three hidden layer nodes trained with the three features extracted from the thrust force signal (MSE = 1.57E-05). **Figure 6** presents the reconstructed tool wear curve for the same drilling test obtained by applying the leave-k-out method with $k = 1$ to the ANN with 5 hidden layer nodes trained with the five features extracted from the thrust force and the torque signal (MSE = 3.79E-06).

For all drilling conditions, the sensor fusion pattern vector FPV_2, including frequency domain features coming from both thrust force and torque signals, provided better results than FPV_1.

The accurate tool wear curve reconstruction achieved by the ANN can be effectively utilized to determine the end of useful tool life through on-line diagnosis during CFRP/CFRP stack drilling, identifying the transition of the tool flank wear between the second and the third phase of the wear curve.

2.1.3. Sensor signal feature extraction and selection in the time domain and neural network pattern recognition for tool wear estimation

Sensor signal feature extraction can also be carried out in the time domain with the aim to find correlations between the extracted sensor signal features and the tool wear state.

In [22], sensor signal feature extraction in the time domain was applied to CFRP/CFRP stack drilling performed with a traditional twist drill bit, usually employed in the aircraft industry

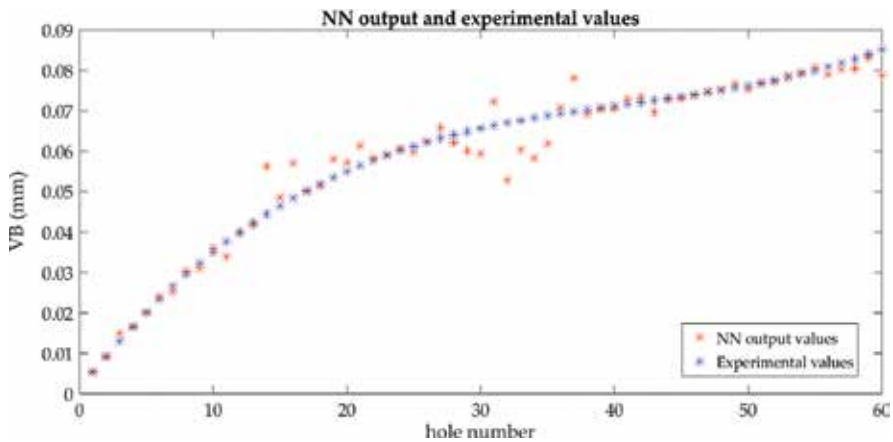

Figure 5. Reconstructed tool wear curve obtained by the ANN trained with the three features extracted from the thrust force signal (6000 rpm–0.11 mm/rev).

http://dx.doi.org/10.5772/intechopen.80466

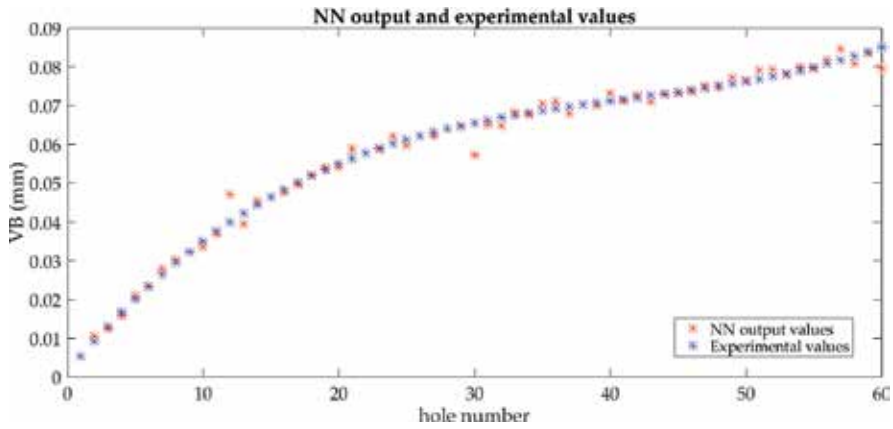

Figure 6. Reconstructed tool wear curve obtained by the ANN trained with the five features extracted from the thrust force and the torque signal (6000 rpm–0.11 mm/rev).

and an innovative geometry step drill bit. The traditional tool was a 2-flute 6.35-mm diameter twist drill with 125° point angle and 30° helix angle tungsten carbide (**Figure 7a**), while the innovative step drill bit was a 2-flute 6.35-mm diameter drill bit with 120° point angle and 20° helix angle made of tungsten carbide (WC) (**Figure 7b**). Different cutting parameters were used for the experimental drilling tests: three feed values (0.11, 0.15, and 0.20 mm/rev) and three spindle speeds (2700, 6000, and 7500 rpm).

A statistical approach in the time domain was applied for feature extraction from the thrust force and torque sensor signals acquired during the drilling tests. The following five statistical signal features were extracted: arithmetic mean, variance, skewness, kurtosis, and signal energy. For each extracted feature, the Spearman correlation coefficient, r_s, was calculated to assess its correlation with tool wear ($0 < r_s < 0.3$, weak correlation, $0.3 < r_s < 0.7$, moderate correlation, and $0.7 < r_s < 1$, strong correlation). Based on the r_s coefficient, five features showed a strong correlation with tool wear: thrust force average (F_{z_av}), torque average (T_{av}), thrust force variance (F_{z_var}), torque variance (T_{var}), and thrust force kurtosis (F_{z_kurt}).

Every 10 holes, a magnified picture of the tool was acquired through an optical measuring machine (Tesa Visio V-200) to measure the flank wear [21]. A 3rd order polynomial interpolation of the VB values was applied to reconstruct the tool wear curves for each drill bit under the tested drilling conditions (**Figures 8** and **9**).

The graphical analysis of the selected sensor signal features, with particular reference to the thrust force average (**Figures 10** and **11**), which is the most correlated feature, shows that the behavior of the features and the behavior of tool wear (**Figure 8** and **9**) display the same increasing trend with increasing number of holes. The average thrust force is higher for the innovative drill bits.

The selected statistical features were employed to construct, for each drilling condition, 60 sensor fusion feature pattern vectors (SFPVs), that is, one for each drilled hole. Each SFPV was built by combining the selected statistical signal features and the corresponding hole number, n. Each SFPV was associated to its matching flank wear value (VB) to create input-output

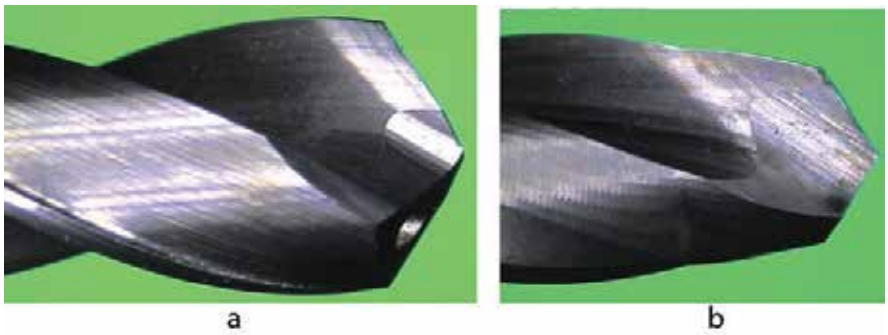

Figure 7. (a) Traditional twist drill bit; (b) innovative step drill bit [22].

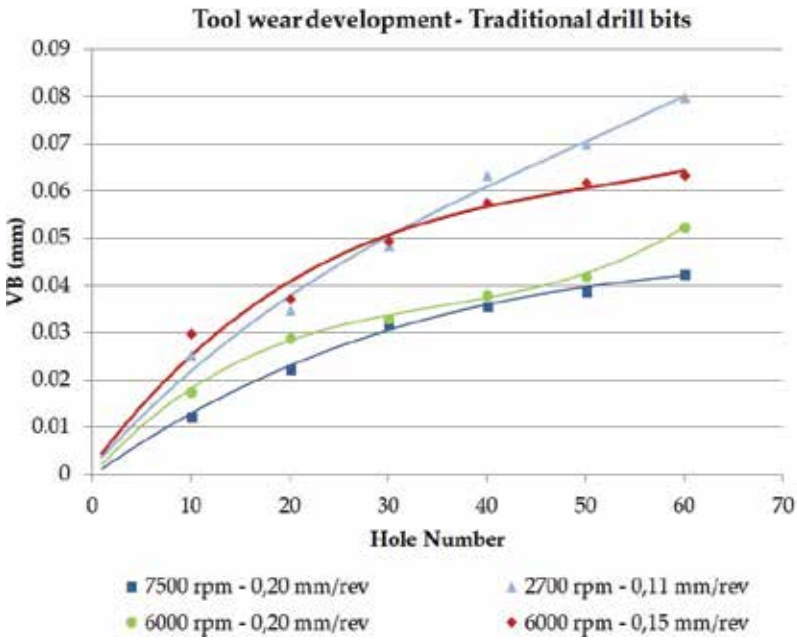

Figure 8. Tool wear values and interpolated curves. Traditional drill bits.

vectors for ANN learning. Three-layer cascade-forward backpropagation artificial neural networks (ANN) using the Levenberg-Marquardt training algorithm were setup [20]. For each drilling condition, 60 input-output vectors (i.e., one for each drilled hole) were built.

To assess the performance of the ANN in properly forecasting the upcoming tool wear values based on a restricted number of initial training input-output vectors and define the smallest number of vectors required to get a reliable tool wear forecast, the number, m, of input-output vectors utilized for ANN training was gradually increased by steps of 10 from $m = 20$ to $m = 50$.

The pattern recognition performance was measured by the root mean squared error (RMSE), that is, the sample standard deviation of the differences between the ANN predicted tool wear values and the experimental tool wear values.

http://dx.doi.org/10.5772/intechopen.80466

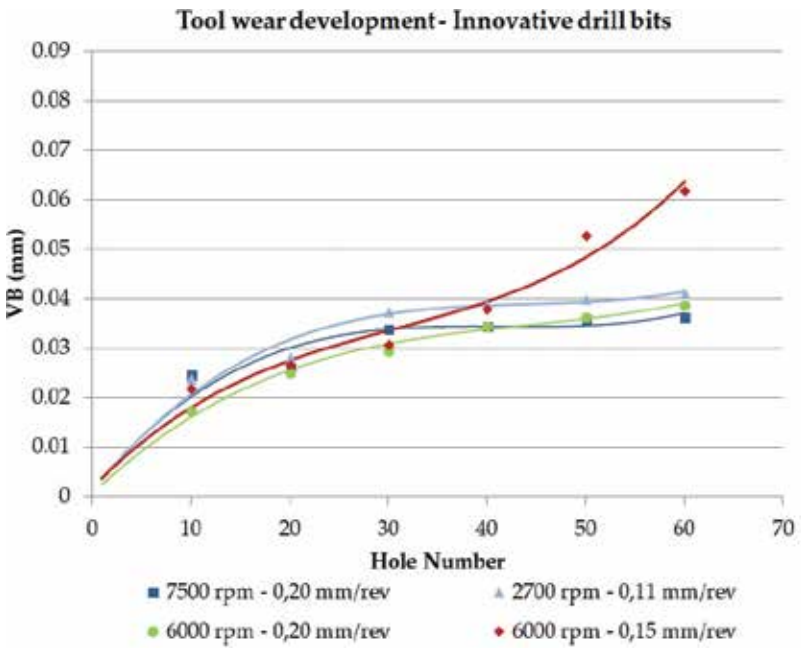

Figure 9. Tool wear values and interpolated curves. Innovative step drill bits.

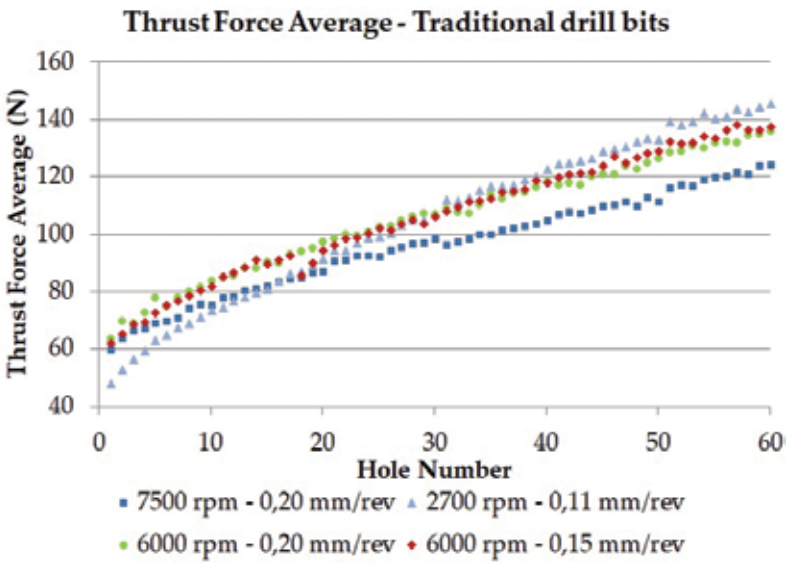

Figure 10. Thrust force average vs. hole number. Traditional drill bits.

In general, the prediction performance improved by increasing *m* since, by enlarging the number of input-output vectors used for training the ANN, the latter was able to enhance the forecast of future tool wear values. Also in the case of the experimental tests carried out

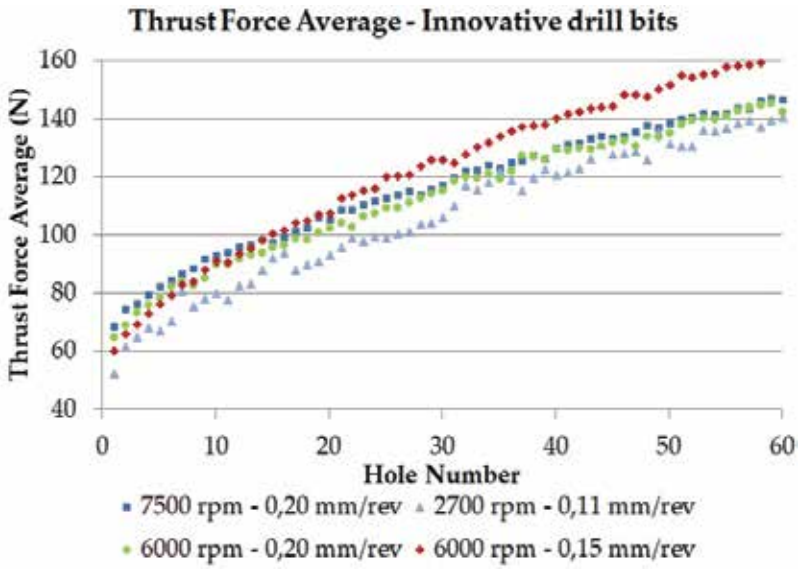

Figure 11. Thrust force average vs. hole number. Innovative drill bits.

with the innovative drill bits, the prediction performance notably improved by enlarging the number of input-output vectors utilized for training the ANN.

The best and the worst ANN prediction performances were found for the innovative drill bits. In the worst case (2700 rpm and 0.11 mm/rev), a maximum RMSE of 0.0164 for m = 20 and of 0.0056 for m = 50 were obtained due to some outliers (**Figure 12**). In the best case (6000 rpm and 0.20 mm/rev), a minimum RMSE of 0.00023 for m = 50 was obtained. **Figure 13** shows the tool wear curves predicted by the ANN for this case. The final curve relative to m = 50 is essentially overlaid to the measured tool wear curve, meaning that the ANN is capable to accurately forecast the future 10 tool wear values.

Even though the ANN prediction can be considered as more demanding in the case of the innovative drill bits, which have a more complex geometry and tool wear development, the ANN performance was still suitable, showing very low prediction errors (minimum RMSE = 0.00023 and maximum RMSE = 0.0164).

The decision making procedure for identifying the end of the tool life based on the ANN prediction can operate in a safe manner, allowing the multiple sensor monitoring procedure to be valuably utilized for on-line tool condition monitoring aimed at the implementation of a condition-based tool substitution strategy instead of a time-based strategy.

In [24], the sensor signal feature extraction methodology in the time domain was applied to drilling of CFRP/CFRP stacks performed using a traditional twist drill bit with different drilling conditions (rotational speed: 2700, 6000, and 9000 rpm and feed: 0.11, 0.15, 0.20 mm/rev).

In this case, thrust force, torque, and acoustic emission sensor signals were acquired during the experimental drilling tests. On these signals, statistical feature extraction and data fusion were implemented to construct sensor fusion pattern vectors in order to make predictions

http://dx.doi.org/10.5772/intechopen.80466

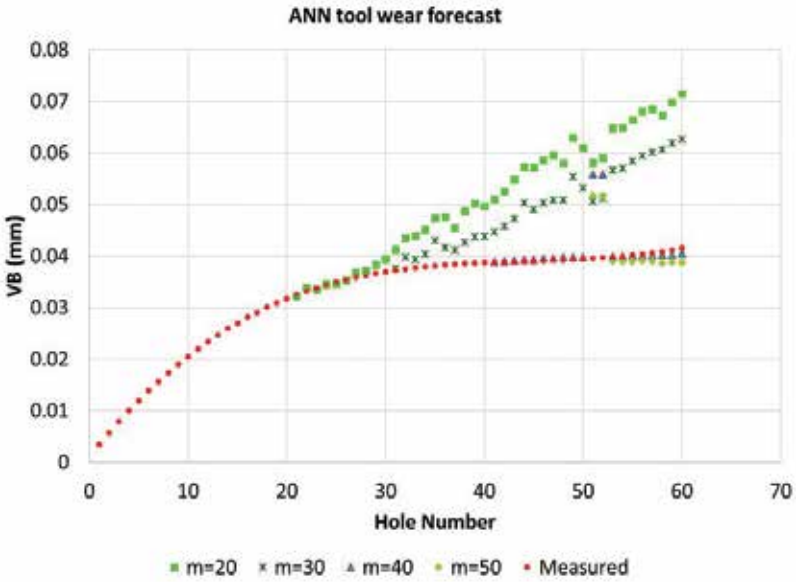

Figure 12. Worst case ANN forecast: experimental tests at 2700 rpm–0.11 mm/rev with innovative drill bit [22].

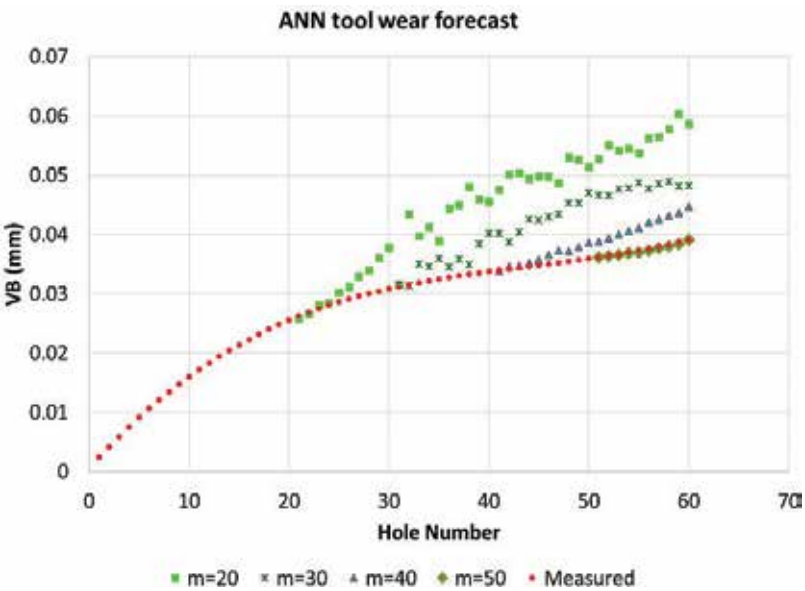

Figure 13. Best case ANN forecast: experimental tests at 6000 rpm–0.20 mm/rev with innovative drill bit [22].

about the state of the tool via artificial neural network-based pattern recognition paradigms. Based on the calculation of the Pearson's correlation coefficient, five best correlated features were identified (thrust force average, thrust force variance, thrust force skewness, torque average, and acoustic emission average), and they were utilized to form the input sensor fusion pattern vector for ANN pattern recognition. The ANN prediction of tool wear was highly

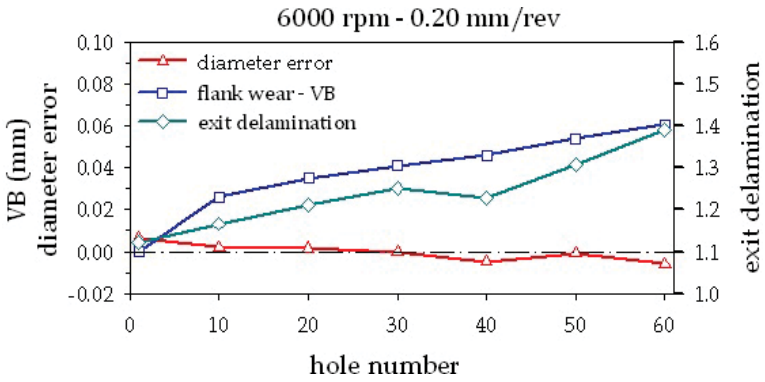

Figure 14. Exit diameter error, tool flank wear, and exit delamination (6000 rpm–0.20 mm/rev).

accurate, with an RMSE <4e-3, showing reliable correlations between fused signal features and tool wear level. The reliable predictions of tool wear development can be used to support on-line decision making on drill bit replacement need.

Moreover, the prediction of tool wear can be functionally utilized to forecast the quality of the drilled holes. The latter was assessed considering dimensional accuracy and entry/exit delamination, which both have an effect on the performance of the CFRP assembly. Dimensional accuracy was measured with reference to hole diameter error, that is, the difference between actual and nominal hole diameter divided by nominal hole diameter [30]. The entry/exit delamination was assessed with reference to the delamination factor, Fd, that is, the ratio between the diameter of the circle encompassing the damaged area and the nominal diameter of the hole [25].

The drilled hole quality evaluations were utilized to set up a criterion for tool replacement need, which is required when the tool wear is responsible for a drilled hole, the quality of which is no longer acceptable. As the lower limit of the tolerance range corresponds to the nominal diameter of the hole, any negative hole diameter error is unacceptable. For each drilling condition, the occurrence of negative hole diameter errors was detected and associated with the corresponding flank wear value and the exit delamination factor.

Under all drilling conditions, the hole diameter error became negative when the flank wear, VB, reached the typical value of 0.04 mm (see **Figure 14**). The latter can be used as a threshold to determine the need for tool change due to an undersized hole diameter. For all drilling conditions, the exit delamination factor grew with increasing number of holes and reached a value between 1.3 and 1.4 when the flank wear reached 0.04 mm. This suggests that the flank wear threshold could also be associated with the second hole quality parameter represented by the exit delamination factor.

Hence, a correspondence between hole diameter error and exit delamination factor with tool wear level was observed. As a result, via on-line prediction of tool wear during drilling, taking into account the identified flank wear threshold, the cognitive sensor monitoring paradigm can provide diagnosis and prognosis services to support decision making on tool replacement need, which is essential for drilling automation.

http://dx.doi.org/10.5772/intechopen.80466

3. Conclusions

This chapter provided an overview of the main challenges related to drilling of fiber-reinforced plastic composite materials which are extensively employed in the aeronautical industry. Rapid tool wear is generated due to the abrasiveness of the reinforcing fibers, and different types of damages affecting material integrity and surface quality, with particular reference to delamination damage generation, are often produced by drilling.

With reference to aeronautical industry applications, where the assembly of CFRP components requires "one-shot" drilling processes so as to allow for easier subsequent riveting avoiding misalignment issues, drilling of CFRP/CFRP stacks made of two superimposed laminates was investigated.

Based on a wide experimental drilling campaign, the case studies analyzed the influence of drilling parameters, tool type and geometry on tool wear development, hole quality and surface integrity, and the opportunity to implement advanced sensor monitoring procedures for tool condition monitoring based on the acquisition and processing of thrust force and torque signals.

Diverse multiple sensor process monitoring procedures were implemented in the drilling of CFRP/CFRP stacks for the assembly of aircraft components, with the aim to support on-line decision making on tool replacement time through cognitive tool wear estimation and hole quality assessment. The monitoring procedures were based on the acquisition and processing of thrust force, torque, and acoustic emission sensor signals during the experimental drilling tests.

With the purpose to explore the complex frequency content of the thrust force and torque sensor signals acquired in the multidirectional CFRP/CFRP stack drilling experimental tests, advanced signal processing was also carried out in the frequency domain.

The sensor signal processing techniques, comprising signal conditioning, feature extraction in the time and frequency domain and data fusion, were implemented to construct sensor fusion feature pattern vectors—made of sensor signal features coming from sensors of different nature—with the aim to find correlations with tool state via artificial neural network-based pattern recognition paradigms.

The ANN performance results achieved in the case studies indicated that, for all CFRP/CFRP stack drilling conditions, by using sensor fusion pattern vectors made of selected features extracted from force and torque sensor signals, a very accurate ANN prediction of tool wear is achieved. As a matter of fact, these procedures demonstrated reliable correlations between sensor signal features and tool wear level both in the case of the features extracted from the time domain and in the case of the features extracted from the frequency domain.

The prediction of tool wear can be functionally utilized to forecast the quality of the drilled holes. As a matter of fact, a correspondence between exit delamination factor and tool wear transition between the second and third phase of the wear curve was observed. In this transition, an exit delamination factor value, Df = 1.4, was identified and set as threshold beyond which unacceptable hole quality is generated.

As a result, taking into account the identified threshold, cognitive tool wear prediction via artificial neural networks can be used for on-line decision making on tool replacement to avoid unacceptable hole quality.

Acknowledgements

The Fraunhofer Joint Laboratory of Excellence on Advanced Production Technology (Fh-J_ LEAPT UniNaples) at the Department of Chemical, Materials and Industrial Production Engineering, University of Naples Federico II, is gratefully acknowledged for its contribution and support to this research activity.

Conflict of interest

The authors declare no conflict of interest.

Author details

Alessandra Caggiano[1,2]*, Luigi Nele[3] and Roberto Teti[1,3]

*Address all correspondence to: alessandra.caggiano@unina.it

1 Department of Industrial Engineering, University of Naples Federico II, Naples, Italy

2 Fraunhofer Joint Laboratory of Excellence on Advanced Production Technology (Fh-J_LEAP T UniNaples), Naples, Italy

3 Department of Chemical, Materials and Industrial Production Engineering, University of Naples Federico II, Naples, Italy

References

[1] M'Saoubi R, Axinte D, Soo SL, et al. High performance cutting of advanced aerospace alloys and composite materials. CIRP Annals - Manufacturing Technology. 2015;**64**: 557-580

[2] Herzog D, Jaeschke P, Meier O, et al. Investigations on the thermal effect caused by laser cutting with respect to static strength of CFRP. International Journal of Machine Tools and Manufacture. Epub ahead of print. 2008. DOI: 10.1016/j.ijmachtools.2008.04.007

[3] Azmir MA, Ahsan AK. A study of abrasive water jet machining process on glass/ epoxy composite laminate. Journal of Materials Processing Technology. 2009;**209**(20): 6168-6173. https://doi.org/10.1016/j.jmatprotec.2009.08.011

[4] Teti R. Machining of composite materials. CIRP Annals - Manufacturing Technology. 2002;**51**(2):611-634. https://doi.org/10.1016/S0007-8506(07)61703-X

[5] Lopresto V, Caggiano A, Teti R. High performance cutting of fibre reinforced plastic composite materials. In: Procedia CIRP. Elsevier B.V. 2016; Vol. 46. pp. 71-82. https://doi.org/10.1016/j.procir.2016.05.079

[6] Ho-Cheng H, Dharan CHK. Delamination during drilling in composite laminates. Journal of Engineering for Industry. 1990;**112**:236-239

[7] Jain S, Yang DCH. Delamination-free drilling of composite laminates. Journal of Engineering for Industry. 1994;**116**:475-481

[8] Shyha IS, Aspinwall DK, Soo SL, Bradley S. Drill geometry and operating effects when cutting small diameter holes in CFRP. International Journal of Machine Tools and Manufacture. 2009;**49**(12-13):1008-1014. https://doi.org/10.1016/j.ijmachtools.2009.05.009

[9] Shyha I, Soo SL, Aspinwall D, Bradley S. Effect of laminate configuration and feed rate on cutting performance when drilling holes in carbon fibre reinforced plastic composites. Journal of Materials Processing Technology. 2010;**210**(8):1023-1034. https://doi.org/10.1016/j.jmatprotec.2010.02.011

[10] Davim JP, Rubio JC, Abrao AM. A novel approach based on digital image analysis to evaluate the delamination factor after drilling composite laminates. Composites Science and Technology. 2007;**67**(9):1939-1945. https://doi.org/10.1016/j.compscitech.2006.10.009

[11] Hocheng H, Tsao CC. Effects of special drill bits on drilling-induced delamination of composite materials. International Journal of Machine Tools and Manufacture. 2006; **46**:1403-1416

[12] Faria PE, Rubio JCC, Reis P, et al. Drilling of fiber reinforced plastics: A review. Journal of Materials Processing Technology. 2007;**186**:1-7

[13] Davim JP. Drilling of Composite Materials. New York, NY, USA: NOVA Publishers; 2009

[14] Murphy C, Byrne G, Gilchrist MD. The performance of coated tungsten carbide drills when machining carbon fibre-reinforced epoxy composite materials. Proceedings of the Institution of Mechanical Engineers, Part B: Journal of Engineering Manufacture. 2002;**216**(2):143-152. https://doi.org/10.1243/0954405021519735

[15] Iliescu D, Gehin D, Gutierrez ME, et al. Modeling and tool wear in drilling of CFRP. nternational Journal of Machine Tools and Manufacture. 2010;**50**:204-213

[16] Brinksmeier E, Fangmann S, Rentsch R. Drilling of composites and resulting surface integrity. CIRP Annals - Manufacturing Technology. 2011;**60**:57-60

[17] Krishnaraj V, Prabukarthi A, Ramanathan A, et al. Optimization of machining parameters at high speed drilling of carbon fiber reinforced plastic (CFRP) laminates. Composites. Part B, Engineering. 2012;**43**:1791-1799

[18] Phapale K, Ahire A, Singh R. Experimental characterization and finite element modeling of critical thrust force in cfrp drilling. Machining Science and Technology. 2018;**22**:249-270

[19] Karpat Y, Bahtiyar O, Deger B, Kaftanoğlu B. A mechanistic approach to investigate drilling of UD-CFRP laminates with PCD drills. CIRP Annals - Manufacturing Technology. 2014;**63**: 81-84

[20] López De Lacalle LN, Rivero A, Lamikiz A. Mechanistic model for drills with double point-angle edges. International Journal of Advanced Manufacturing Technology. 2009; **40**:447-457

[21] Caggiano A, Centobelli P, Nele L, et al. Multiple sensor monitoring in drilling of CFRP/ CFRP stacks for cognitive tool wear prediction and product quality assessment. Procedia CIRP. 2017;**62**:3-8

[22] Caggiano A, Napolitano F, Nele L, et al. Multiple sensor monitoring for tool wear forecast in drilling of CFRP/CFRP stacks with traditional and innovative drill bits. Procedia CIRP. 2018;**67**:404-409

[23] Caggiano A, Rimpault X, Teti R, et al. Machine learning approach based on fractal analysis for optimal tool life exploitation in CFRP composite drilling for aeronautical assembly. CIRP Annals. 2018:1-4

[24] Caggiano A, Nele L, Nele L. Artificial neural networks for tool wear prediction based on sensor fusion monitoring of CFRP/CFRP stack drilling. International Journal of Automation Technology. 2018;**12**:275-281

[25] Caggiano A, Angelone R, Teti R. Image analysis for CFRP drilled hole quality assessment. In: Procedia CIRP. Elsevier B.V. 2017. Vol. 62. pp. 440-445. https://doi.org/10.1016/j.procir.2017.03.045

[26] Angelone R, Caggiano A, Improta I, et al. Temperature measurements for the tool wear and hole quality assessment during drilling of CFRP/CFRP stacks. Procedia CIRP. 2018; **67**:416-421

[27] Bonnet C, Poulachon G, Rech J, et al. CFRP drilling: Fundamental study of local feed force and consequences on hole exit damage. International Journal of Machine Tools and Manufacture. 2015;**94**:57-64

[28] Karpat Y, Bahtiyar O, Deger BKB. A mechanistic approach to investigate drillingof UD-CFRP laminates with PCD drills. CIRP Annals - Manufacturing Technology. 2014; **63**:81-84

[29] Teti R, Jemielniak K, O'Donnell G, et al. Advanced monitoring of machining operations. CIRP Annals - Manufacturing Technology. 2010;**59**:717-739

[30] Sadek A, Meshreki M, Attia MH. Characterization and optimization of orbital drilling of woven carbon fiber reinforced epoxy laminates. CIRP Annals - Manufacturing Technology. 2012;**61**:123-126

Chapter 6

Nanocomposite Polyimide Materials

Anton Yegorov, Marina Bogdanovskaya,
Vitaly Ivanov, Olga Kosova, Kseniia Tcarkova,
Vasily Retivov and Olga Zhdanovich

Additional information is available at the end of the chapter

http://dx.doi.org/10.5772/intechopen.79889

Abstract

The transition to nanosized fillers allows to significantly improve the characteristics of composites while reducing their degree of filling, and in some cases to achieve new properties unattainable with the use of traditional fillers and modifiers. Polymeric nanocomposites have unique barrier properties, electrical conductivity, thermal conductivity, increased strength, heat resistance, and thermal stability, as well as reduced flammability. It is known that the addition of nanodispersed layered silicates and various forms of carbon nanofillers to polymeric matrices can significantly affect the mechanisms of thermal and thermooxidative destruction and burning of nanocomposites. In this chapter, we compare the properties of composite materials based on nanostructured silicon carbide and carbon nanotubes with modified and unmodified surfaces obtained on three types of polyimide matrices (matrix No. 1 based on pyromellitic dianhydride and 4,4′-oxydianiline, matrix No. 2 based on 3,3′,4,4′-benzophenone tetracarboxylic acid dianhydride and p-phenylenediamine, and matrix No. 3 based on pyromellitic dianhydride and 4-[4-(4-aminophenoxy) phenoxy] phenylamine). The dynamic viscosity of polyamide acid, the physicomechanical characteristics of film polymer composite materials, the determination of thermal stability, and thermooxidative destruction mechanism of composites were determined.

Keywords: polyimides, polyimide matrix, nanocomposites, composite materials, carbon nanotubes, silicon carbide, fillers

1. Introduction

The wide introduction of polymer materials in various fields of production is due to their special mechanical and physicochemical characteristics, such as elasticity, low brittleness,

directional changes in structure and properties under physicochemical effects. To reduce the cost of material and give it special properties, various fillers are actively used.

Most of the composite materials are developed for the aerospace industry, which has always been and still is the most high-tech branch of modern production. At the same time, these materials and technologies for their production are also innovative drivers in many other sectors, such as construction, engineering, energy, instrumentation, medicine.

To produce materials with increased rigidity, impact, and tribological properties, during the last decade a lot of research has been devoted to the modification of polymers by nanoparticles. These composites exhibit unique properties that combine the advantages of inorganic fillers, such as stiffness, high thermal stability, and mechanical properties with processability, flexibility, and plasticity of organic polymers. Due to the influence of nanosized fillers on the bulk properties of polymer nanocomposites, it is possible to achieve such unique properties by adding small amounts of nanofillers to the polymer matrix.

Polymeric nanocomposites representing a new class of materials have unique barrier properties, electrical conductivity, thermal conductivity, increased strength, heat resistance, and thermal stability, as well as reduced combustibility. It is known that the addition of nanodispersed layered silicates and various forms of carbon nanofillers to polymeric matrices can significantly affect the mechanisms of thermal and thermooxidative destruction and burning of nanocomposites.

One of the most important issues facing nanotechnology is how to get molecules to group themselves in a certain way, to organize themselves, in order to eventually obtain new materials or devices capable of long-term preservation of their performance properties under the action of high and very low temperatures, chemical agents, increased radiation, and other factors. One of the main ways to solve this problem is the creation of composite materials based on a polyimide (PI) matrix. Adding different amounts of nanoparticles at different stages of polymerization of the matrix, increasing the number of available monomers (dianhydrides acid), and reversibility of the imidization reaction (the second stage of the synthesis reaction) will allow to vary the molecular and molecular mass characteristics and, as a consequence, their thermal resistance and solubility to processing, deformation-strength, and other properties of future composites.

In the world literature, examples of nanocomposite materials based on polyimide matrix filled with carbon nanotubes (CNTs), carbon fibers, and nanostructured silicon carbide (SiC) are known, and their thermal and deformation strength and other properties have been measured. Expanding the diversity of polyimide matrices and varying the content of nanostructured materials allow us to obtain a huge variety of composite materials.

Thus, creation of new composite materials with high performance characteristics and technology for their production is a very urgent and important task.

During the last decade, a lot of research has been devoted to the combination of polymers with nanoparticles to produce materials with increased rigidity, impact, and tribological properties [1]. The growing demand for nanomaterials is due to the fact that new chemical and physical properties are achievable with the addition of nanosized fillers to the polymer matrix, even if the same material without a nanofiller does not have such advantages. This is due to the influence of the unique nature of the nanosized filler on the bulk properties of nanocomposites on

a polymer basis [2, 3]. Polymer nanocomposites are extensively studied for a potentially wide range of applications due to their ease of processing, low production costs, good adhesion to the substrate, and unique physicochemical properties. Dispersing of inorganic materials in a polyimide matrix is a complex task and a key factor affecting the final properties of hybrid materials. The addition of a cross-linking agent is a solution to overcome the difficulties associated with dispersing. By adding a cross-linking agent, organic and inorganic materials can be covalently bonded and compatibility between these two phases can be improved [4, 5].

The transition to nanofillers has significantly improved the performance of composites and achieved new properties unattainable with the use of traditional fillers and modifiers.

With the development of industries, an increase in the operating temperature range occurs, as a result of which the requirements for materials increase.

2. Polyimides: the structure of polyimide matrices

Polyimides are one of the most interesting polymers, which have increased heat resistance and are widely used in the manufacture of high-temperature plastics, adhesives, dielectrics, and other materials.

Currently, polyimide resins are used as matrices to create reinforced composites based on lightweight carbon fibers, as a replacement for metal parts in the aerospace industry and airframe, due to their outstanding thermal and mechanical resistance, as well as resistance to the action of ionizing radiation. Polyimide resins are widely used in such areas as microelectronics, aerospace, gas separation, and the production of fuel cells. They are used in the cable industry for the production of electrical insulating varnishes and enamels, which have high heat resistance, elasticity, and good dielectric properties.

As is known, polyimides (PI) can be aliphatic, alicyclic, or aromatic, depending on the chemical structure. Depending on the structure of the chain, polyimides can be linear or three-dimensional [6]. There are polyimides with aliphatic links in the main chain of the macromolecule and purely aromatic polyimides. The first are solid, readily crystallizable substances of white or yellow color. Polypyromellitimides based on aliphatic diamines containing less than seven carbon atoms in the molecule have high melting points that are higher than the temperatures of their onset of decomposition (above 350°C) and do not dissolve in known organic solvents. Polypyromellitimides based on aliphatic diamines containing, in the chain, more than seven carbon atoms or having a branched hydrocarbon chain (at least seven carbon atoms), as well as polyimides of other aromatic tetracarboxylic acids and various aliphatic diamines, soften at temperatures of 300°C.

Aromatic polyimides are characterized by high heat resistance, and the most heat-resistant polyimides based on pyromellitic acid (**Figure 1**) and 1,4,5,8-naphthalenetetracarboxylic (**Figure 2**) acids, practically not softening before the onset of thermal decomposition, have a glass transition temperature of 500°C.

The heat resistance of other polyimides is well regulated by varying the nature of the monomers and is usually 300–430°C [7]. Most aromatic polyimides, especially high-heat-resistant,

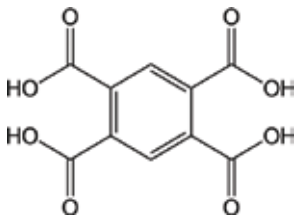

Figure 1. Structural formula of pyromellitic acid.

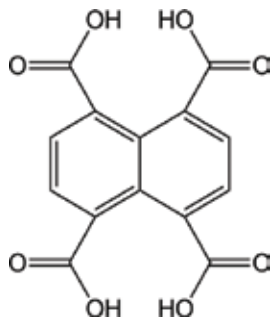

Figure 2. Structural formula of 1,4,5,8-naphthalenetetracarboxylic acid.

are insoluble in known organic solvents and are inert to the action of oils, and also hardly change under the action of dilute acids.

With the introduction of various substituents into the side chain, especially card groups (phthalide, phthalimidine, fluorene, anthrone), the solubility of polyimides is substantially improved. Thus, polypyromellitimide aniline phthalate is soluble in dimethylformamide (DMF), m-cresol, sym-tetrachloroethane, and hexafluoro-2-propanol. Polyimides based on 3,3′,4,4′-benzophenone tetracarboxylic acid or 3,3′,4,4′-diphenyloxide tetracarboxylic acid and anilinfluorene polyimides are also dissolved in methylene chloride and chloroform [8]. Under the influence of alkalis and superheated steam, aromatic polyimides hydrolyze. However, the propensity for hydrolysis depends significantly on their nature. Thus, polyimides with five-membered imide cycles are much less hydrolytically stable than analogous polyimides with six-membered rings.

Aromatic polyimides are distinguished by high radiation resistance [9]. Thus, poly(4,4′-diphenylene oxide pyromellitimide) films retain good mechanical and electrical characteristics after irradiation with high-energy electrons at a dose of 102 MJ/kg (films of polystyrene and polyethylene terephthalate become brittle after irradiation with a dose of 5 MJ/kg). Polyimides are resistant to the action of ozone, i.e., retain 50% strength after exposure to 3700 hours in air with an admixture of 2% ozone; they are also resistant to UV radiation. An important feature of aromatic polyimides is their high thermal stability.

The most heat-resistant are polyimides containing only imide rings and aromatic rings. In a vacuum and an inert atmosphere, aromatic polypyromellitimides are resistant to 500°C, and a significant reduction in mass (up to ~65% of the initial one) occurs above this temperature, after

http://dx.doi.org/10.5772/intechopen.79889

which the mass of the residue remains practically unchanged up to 3000°C. Aromatic polyimides are also stable under conditions of prolonged isothermal heating; there is a decrease in the mass of poly-4,4′-diphenylene oxide-pyromellitimide after heating in an inert atmosphere for 15 hours at 400, 450, and 500°C by 1.5, 3.0, and 7.0%, respectively. Significantly more intensive polyimides decompose during thermal oxidation. The main products of destruction of aromatic polyimides are CO and CO_2.

To date, a wide range of polymers have been obtained by changing the chemical structure of the dianhydride (Q) and diamine (R) fragments of macromolecules (**Figure 3**), differing in structure and properties.

By chemical structure and physical properties (softened and melted), they are divided into four groups.

- Group A: polyimides consist only of aromatic groups and imide cycles. These polyimides are non-softening, Tm > Td, hard, brittle with maximum heat resistance (**Figure 4**).
- Group B are the PI with hinges (connections around which a chain turn is possible) in the dianhydride fragment. These are non-softening, rigid polymers, with some elasticity (**Figure 5**).
- Group C are the PI with hinges in the diamine fragment. These are rigid, strong, and elastic polymers that do not have a clearly defined range of softening temperatures (**Figure 6**).
- Group D are the PI with hinges in the diamine and in the dianhydride fragment. These polymers are elastic and have a clear region of softening and melting (**Figure 7**).

So, all the cyclic structures can be divided into several types, the thermostability of which will decrease in the following order: conjugated carbocycles (carbon) ≥ ladder structures > condensed heterocycles > isolated heterocycles > non-conjugated carbocycles [6].

As noted above, the stability of polyimides at high temperatures is naturally determined primarily by their chemical structure. The data on the dependence of thermal stability on the chemical structure are of great importance both in determining the ways of further synthesis of thermostable polyimides and in selecting among them the most practically promising ones.

A huge number of polyimides obtained on the basis of a large number of dianhydrides of tetracarboxylic acids have been synthesized and characterized. The main practical application

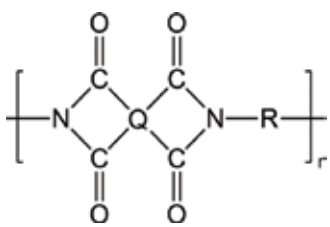

Figure 3. General structural formula of polyimide.

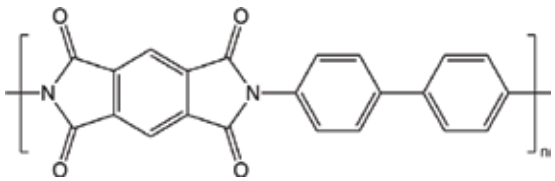

Figure 4. Benzidine polypyromellitimide (Group A).

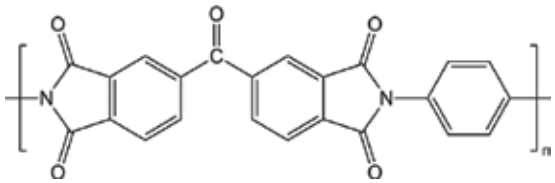

Figure 5. 3,3′,3,4′-Benzophenone tetracarboxylic acid dianhydride and p-phenylenediamine polyimide (Group B).

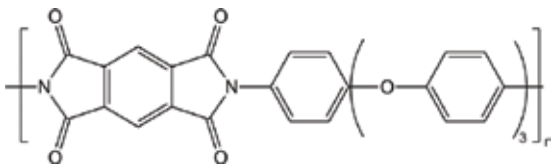

Figure 6. Polyimide based on pyromellitic dianhydride (Group C).

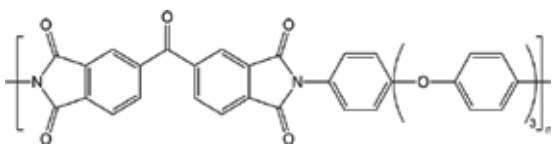

Figure 7. Polyimide based on 3,3′,4,4′-benzophenone tetracarboxylic acid dianhydride (Group D).

was found for polyimides made of pyromellitic acid dianhydrides; 3,3′,4,4′-diphenyloxide tetracarboxylic acid; and 3,3′,4,4′-benzophenone tetracarboxylic acid.

3. Composite materials containing nanosized filler

The introduction of small amounts of modern fillers, such as carbon nanotubes, carbon fibers, and nanostructured silicon carbide, increases the thermal stability, which makes it possible to obtain a composite material with high performance properties.

Recently, carbon nanotubes (CNTs) have attracted attention, since nanocomposites based on them will have improved mechanical properties. In addition, they can provide a certain type of electrical conductivity. It is expected that the combination of CNTs and polyimides will play an important role in the development of new, highly effective nanocomposites [10].

http://dx.doi.org/10.5772/intechopen.79889

There are two general methods for obtaining composites. One is the mixing of CNTs with a polymer matrix in a molten form to produce a composite. The other is the dispersion of CNTs in the polymer solution, curing the resulting solution and removing the solvent.

Park et al. have reported on a method of effective dispersion of single-walled carbon nanotubes (SWNTs) in a polyimide matrix [11]. The obtained SWNT polyimide films are electrically conductive and optically transparent. A jump in the conductivity was observed between 0.02 and 0.1 vol.% SWNT; during this process the nanocomposite was converted from a capacitor to a conductor. Appending 0.1 vol.% SWNT increased the conductivity by 10 orders of magnitude, which exceeds the antistatic criterion for thin films for space applications (1×10^{-8} S cm^{-1}). A polyimide film containing 1.0 vol.% SWNT still passed 32% of visible light at 500 nm, while the film obtained by direct mixing passed less than 1%. A dynamic mechanical test showed that elastic modulus increases by 60% by addition of 1.0 vol.% SWNT; also the thermal stability of polyimide improves in the presence of SWNT.

Connel et al. [12] have reported on a synthesis of alkoxysilane polyamide acid (PAA), with SWNTs added to the previously prepared polyamide acid solution. When the loading was 0.05 wt.% SWNT, the percolation barrier was reached, which is evident from the sharp drop in the surface resistance of the material. Surface resistance and bulk resistance indicate that the SWNT polyimide composite is conductive. However, the presence of SWNT in polyimide has very small influence on Tg and the tensile strength of the polymer [12]. Increase in ionic strength of the polyimide matrix by adding an inorganic salt ($CuSO_4$) led to the formation of an SWNT network sufficient for conductivity. The addition of 0.014 wt.% $CuSO_4$ into a composite containing 0.03 wt.% SWNT led to films, reduced by four orders of magnitude of the surface and bulk resistance [13, 14]. There is an increased electrical conductivity of nanocomposite films; however, electric percolation occurs at larger loads than those that are commonly used in SWNT polyimide nanocomposites. The parameters of the film modulus slightly increase with growth of SWNT content. Electrospun fibers were obtained from the same SWNT polyimide suspensions used for the preparation of films. Images obtained by high-resolution scanning electron microscopy showed that SWNT are inside fibers and can have an orientation parallel to the fiber axis [15].

Sun and coworkers [16] have reported on the production of functionalized CNT by using polyimides with side hydroxyl groups. It was found that the obtained polyimide functionalized CNT are soluble in the same solvents as the original polyimide. A significant advantage of this method is that these functionalized nanotubes can be used directly to produce polyimide-CNT composites with relatively high content of nanotubes.

Electrically conductive polyimide composites are made from corresponding polyimides and electrically conductive fillers, such as carbon nanotubes, graphite, and acetylene black. The polyimide precursor (polyamide acid) was synthesized from 3,4,3′,4′-biphenyl tetracarboxylic dianhydride and 4,4′-diaminodiphenyl ether by means of intensive mechanical stirring at −5°C. The results of the experiments showed that the electrically conductive composites based on carbon nanotubes and polyimide possess better electrical, mechanical, and adhesive properties than the other two composites [17].

In addition to carbon nanotubes, one of the promising fillers is nanostructured silicon carbide (SiC). SiC nanoparticles are chosen because of their unique physical properties, such as

excellent chemical stability, heat resistance, high electron mobility, excellent thermal conductivity, outstanding mechanical properties. They are used to produce high-performance composites and are used in electronics [18, 19]. These properties make SiC nanoparticles a suitable material for the production of polymer nanocomposites with a reinforced structure [20].

There are reports of the nanocomposite films' properties, which were obtained by two simple methods from a new polyimide and nanoparticles of silicon carbide, SiC. In the first method, the SiC nanoparticles were initially functionalized with epoxy end groups using 3-glycidoxypropyltrimethoxysilane (mSiC); then, this solution was mixed with polytriazoles. A homogeneous solution for preparation of the film based on polytriazoles and mSiC was heated in vacuo. In the second method, a new diamine containing the 1,2,4-triazole ring, and the commercially available dianhydride (4,4′-(hexafluoroisopropylidene) diphthalic dianhydride) reacted in situ in the presence of SiC nanoparticles to form a homogeneous mixture of polyamide acid and silicon carbide (PAA/SiC). Next, after a high-temperature process in a vacuum, the mixture turned into a film based on polytriazoles and SiC. The research results showed that a strong chemical bond between the SiC nanoparticles and the polymer matrix leads to an increase in the glass transition temperature Tg from 300°C to higher than 350°C, the tensile strength from 108 MPa to 165 MPa, and the temperature of 5% weight loss (Td5%) from 380 to 500° C. The intensity of photoluminescence also increased, and moreover, with an increase of the SiC content, a shift in the blue region of the spectrum can be observed [21].

A highly effective composite material based on silicon carbide (SiC) and bismaleinimide, modified with allylic novolak for abrasive tools and wear-resistant elements, was developed and characterized. The research results showed that the residual strength at 440°C (1 hour) decreased to 64%, and the thermooxidative stabilities, compared to SiC/polyimide composites, which were made in a similar way, were also better. The ratio of polymer in the composite affects the mechanical properties—its flexural strength increases with the increase of bismaleinimide ratio. However, the excess content of bismaleinimide results in the formation of bubbles in the composite structure. The best composite with a flexural strength of 82.4 MPa was obtained by using 13 wt.% bismaleinimide. After treatment at 280°C for 1 hour, the flexural strength increased by 34% because of the further polymer cross-linking at a higher temperature [22].

It is expected that the combination of polyimides and other organic/inorganic compounds will play an important role in the development of innovative high-performance nanocomposites for various applications.

One of the main problems in obtaining nanocomposites is the prevention of aggregation of particles. It is quite difficult to obtain a monodisperse distribution of nanoparticles in a polymer matrix. This problem can be solved by modifying the nanoparticle surface, which allows improving the interaction of the inorganic modifier and the polymer. There are two main versions of modification. The first is carried out by adsorption or reaction of the surface layer with small molecules (for example, with silanizing agents). The second option is based on grafting polymer molecules through covalent bonds to hydroxyl groups existing on the surface of nanoparticles. The second method has the advantage that it allows one to obtain particles with necessary and predictable properties, due to the possibility of fine selection of the type of particles, grafted monomer, and process conditions.

http://dx.doi.org/10.5772/intechopen.79889

4. Preparation of composite materials based on a polyimide matrix modified by inorganic nanofillers

There are two basic mixing mechanisms: simple and dispersive.

Simple mixing is the process in which a random distribution of the particles of the initial components in the volume of the mixture occurs without changing their initial dimensions.

Dispersive mixing is a process of mixing, which is accompanied by a change (decrease) in the initial particle sizes of the components, due to their fragmentation, aggregate destruction, deformation, and disintegration of the dispersed phase, etc. The main task of dispersive mixing is to destroy aggregates of solid particles and distribute them in the volume of a liquid polymer [23].

When creating polymer nanocomposites with an already prepared nanofiller, three main methods are used:

- Mixing in solution (for solubles in organic solvents of polymers)
- Melt mixing (for thermoplastic polymers)
- In-situ polymerization

Since the polyimide matrixes used are insoluble in organic solvents and their softening temperature exceeds 300°C, it is advisable to use in-situ polymerization.

4.1. Methods for producing composite materials based on a polyimide matrix modified with carbon nanotubes and silicon carbide

Carbon nanotubes have excellent mechanical, electrical, and magnetic properties, as well as a nanometer scale with a high length-to-diameter ratio, which makes them an ideal reinforcing agent for high-strength polymer composites. However, CNTs usually form bundles stabilized by van der Waals forces, which are extremely difficult to disperse in the polymer matrix. The biggest problem in the production of reinforced CNT composites is the efficiency of the dispersion of CNTs in the polymer matrix. There are several methods for dispersing nanotubes in a polymer matrix, such as mixing in solution, melt mixing, electroforming, in-situ polymerization, and chemical functionalization of carbon nanotubes.

4.1.1. Mixing in solution

With this approach, the dispersion of carbon nanotubes in a suitable solvent and the polymer are mixed in solution. The CNT/polymer composite is formed by precipitation or by evaporation of the solvent. It is well known that it is very difficult to efficiently disperse nanotubes in a solvent by simple mixing. Processing with high-power ultrasound is more effective in the formation of the dispersion of CNTs. Ultrasonic treatment is widely used for dispersing, emulsifying, crushing, and activating particles. With the help of ultrasound, it is possible to effectively destroy aggregates and coils of carbon nanotubes.

The chemical effects of ultrasonic dispersion are associated with a rapid (on a scale of microseconds) intensive collapse of cavitation bubbles created during the passage of ultrasonic waves through a liquid medium [24]. Sonochemical theory and related studies have shown that ultrasonic cavitation can generate high local temperature and pressure [25].

Nanomaterials tend to agglomerate with stirring in a liquid, while the creation of nanocomposites requires efficient dispersion and a uniform distribution of nanoparticles in the liquid.

To overcome the strength of the bonds after wetting the powder, effective ways of deagglomeration and dispersion are needed. The ultrasonic disintegration of agglomerates in suspensions allows full use of the potential of nanomaterials. Studies on various dispersions of agglomerates of nanoparticles with different solids content have demonstrated significant advantages of ultrasound compared to other technologies, such as rotary agitators, piston homogenizers, ball mills, and colloidal mills.

4.1.2. Melt mixing

For mixing in solution, the polymer matrix must be soluble in at least one solvent. This is problematic for many polymers. Melt mixing is generally applicable and fairly simple, especially when used in the case of thermoplastic polymers. In the melt spinning process, carbon nanotubes are mechanically dispersed in the polymer matrix using a high-shear mixer at high temperature [26]. This approach is simple and compatible with existing industrial technologies. Shear forces destroy CNT aggregates and prevent their formation.

The disadvantage of this method is that this method produces a dispersion of carbon nanotubes in the polymer matrix, which is significantly worse than the dispersion that can be achieved by mixing in solution. In addition, carbon nanotubes should be smaller because of the high viscosity of the composites with a higher content of carbon nanotubes.

4.1.3. In-situ polymerization

Using this method, carbon nanotube or nanostructured silicon carbide is dispersed in the monomer followed by polymerization. Moreover, a higher percentage of fillers can be easily dispersed, and they form a strong interaction with the polymer of the matrix. This method is used for the preparation of composites with polymers that cannot be processed by mixing in solution or melt mixing, for example insoluble and thermally unstable polymers.

In the case of using a polyimide matrix, which is obtained by polycondensation, it is expedient to use the in-situ polymerization method.

4.2. Modification of the nanofiller surface

4.2.1. Modification of the surface of carbon nanotubes

To date, there are no generally accepted standards describing the characteristics and properties of manufactured nanotubes. Their properties are individual for each manufacturer. Nanotubes can initially differ in diameter (and number of layers), average length, content of

http://dx.doi.org/10.5772/intechopen.79889

impurities (primarily amorphous carbon, metal catalyst residues and adsorbates), degree of aggregation, and other less important parameters.

In order to effectively use carbon nanotubes as a component of polymer composites, it is considered advisable to modify their surface to increase the strength of the nanotube and polymer matrix interaction, as well as to improve the dispersibility of nanotubes. To solve this problem, a functionalization method has been chosen that allows the creation of carboxyl functional groups on the surface of nanotubes, since this allows binding of the filler with covalent bonds to the polymer molecule; this is achieved by oxidation of the initial nanotubes with a mixture of nitric and sulfuric acids. Such functionalization of nanotubes is accompanied by the opening of their ends and, in some cases, by "cutting" nanotubes during oxidation. Also, oxygen-containing groups create a negative electrostatic charge on the surface, which contributes to less aggregation and better dispersibility. Oxidative functionalization also reduces the amount of residual amorphous carbon.

The presence of the ─C(O)OH group is judged by the presence in the IR spectrum of the characteristic bands $\nu_{c=o}$ = 1614–1620 cm $^{-1}$ (─COO^{-}) and $\nu_{c=o}$ = 1710–1735 cm $^{-1}$ (─COOH), and also bands at 1585–1590, 1200–1205 and 1800 cm^{-1}.

4.2.2. Modification of the surface of nanostructured silicon carbide

As a modifying agent capable of forming strong contacts with inorganic particles, organosilicon compounds containing alkoxysilyl groups are most often used. The interaction of organosilicon compounds with silicon oxide, which is present on the surface of nanostructured silicon carbide, chemically binds the organosilicon fragment and the surface hydroxyl groups of the particle. This leads to the hydrophobization of the surface of the filler particle, which makes it possible to form a strong contact with the polymer. In addition, a reactive amino group appears on the surface of the particles, allowing additional covalent binding to be achieved.

In this case (3-aminopropyl) triethoxysilane (trade name: Silane coupling agent KN-550) was used as the modifying agent, which has a wide field of application in the field of composites production. This cross-linking agent is very sensitive to moisture; therefore, it is necessary to use dried solvents to modify the filler surface with it.

To evaluate the effectiveness of surface modification of nanostructured silicon carbide, infrared spectroscopy and the CHNS method were used (the nitrogen content of the final compound was estimated).

4.3. Preparation of composite materials based on silicon carbide and carbon nanotubes

The main process for obtaining dispersion-filled plastic masses (for the preparation of composites based on polyimide and CNT or nanostructured silicon carbide) is mixing. These are complex physicomechanical and physicochemical processes associated with the action of force fields, the displacement of the original components of the mixture in the reactor volume along complex trajectories, with the formation of a system characterized by a randomly distributed distribution of components.

As noted earlier, the polyimide matrices used are insoluble in organic solvents, and their softening temperature exceeds 300°C, which means that it is expedient to use the in-situ polymerization method as a basis.

The technologies of obtaining a composite material in the form of a powder and in the form of films were studied.

The process of obtaining a powder of composite material was divided into four stages:

- Modification of the surface of nanostructured silicon carbide or carbon nanotubes
- Dispersion of inorganic filler in a solution of high-boiling solvent and diamine
- Carrying out the polymerization and imidization reaction
- Isolation of the resulting composite in the form of a powder

The process of obtaining a film composite material was divided into five stages:

- Modification of the surface of nanostructured silicon carbide or carbon nanotubes
- Dispersion of inorganic filler in a solution of high-boiling solvent and diamine
- Carrying out the polymerization reaction to obtain a precursor solution (polyamide acid)
- Application of the resulting polyamide acid solution to the substrate
- Drying of the solvent followed by stepwise imidization in a vacuum drying cabinet

Experiments were carried out to produce composites based on nanostructured silicon carbide with a modified and unmodified surface, and also based on carbon nanotubes with a modified and unmodified surface. These experiments were conducted to study the effect of different contents of inorganic fillers with varying degrees of surface modification on the properties of the resulting composite materials (**Table 1**).

All the composites obtained were characterized by the methods of elemental analysis, IR spectrometry. Thermal and thermooxidative destruction was evaluated, and the glass transition temperature of the resulting materials was determined.

As initial polymer matrices, polyimide matrices with different degrees of structural rigidity were chosen.

1. matrix No. 1 was obtained by the interaction of pyromellitic dianhydride and 4,4′-oxydianiline (PMDA/ODA) (**Figure 8**);
2. matrix No. 2 was obtained by the interaction of 3,3′,4,4′-benzophenone tetracarboxylic acid dianhydride and p-phenylenediamine (BTDA/pPDA) (**Figure 9**);
3. matrix No. 3 was obtained by the interaction of pyromellitic dianhydride and 4-[4-(4-aminophenoxy)phenoxy] phenylamine (PMDA/AFFA) (**Figure 10**).

No.	Type of inorganic filler	Surface state of inorganic filler	Inorganic filler content, wt.%
1	Matrix No. 1 (pyromellitic dianhydride and 4,4′-oxydianiline (PMDA/ODA))		
	Nanostructured SiC	Unmodified	0.05%, 0.1%, 0.25%, 0.5%, 1%, 2%
	Nanostructured SiC	Modified	0.05%, 0.1%, 0.25%, 0.5%, 1%, 2%
	Single-walled carbon nanotubes	Unmodified	0.1%, 0.25%, 0.5%, 0.75%, 1%, 2%
	Single-walled carbon nanotubes	Modified	0.1%, 0.25%, 0.5%, 0.75%, 1%, 2%
2	Matrix No. 2 (3,3′, 4,4′-benzophenone tetracarboxylic acid dianhydride and p-phenylenediamine (BTDA/pPDA))		
	Nanostructured SiC	Unmodified	0.05%, 0.1%, 0.25%, 0.5%, 1%, 2%
	Nanostructured SiC	Modified	0.05%, 0.1%, 0.25%, 0.5%, 1%, 2%
	Single-walled carbon nanotubes	Unmodified	0.1%, 0.25%, 0.5%, 0.75%, 1%, 2%
	Single-walled carbon nanotubes	Modified	0.1%, 0.25%, 0.5%, 0.75%, 1%, 2%
3	Matrix No. 3 (pyromellitic dianhydride and 4-[4-(4-aminophenoxy)phenoxy] phenylamine (PMDA/AFFA))		
	Nanostructured SiC	Unmodified	0.05%, 0.1%, 0.25%, 0.5%, 1%, 2%
	Nanostructured SiC	Modified	0.05%, 0.1%, 0.25%, 0.5%, 1%, 2%
	Single-walled carbon nanotubes	Unmodified	0.1%, 0.25%, 0.5%, 0.75%, 1%, 2%
	Single-walled carbon nanotubes	Modified	0.1%, 0.25%, 0.5%, 0.75%, 1%, 2%

Table 1. Experiments of producing powders of composite materials based on nanostructured SiC and CNT.

4.4. Properties of the resulting composite materials

4.4.1. Effect of nanosized filler on the viscosity of the precursor for the production of film composite materials

Solutions of polyamide acids (PAAs) are precursors in the preparation of polyimide films and composites based on them, and the degree of viscosity of this solution is an important parameter for the success of this experiment.

The effect of different contents of nanosized silicon carbide and carbon nanotubes on the viscosity of a precursor in the preparation of film composite materials was studied.

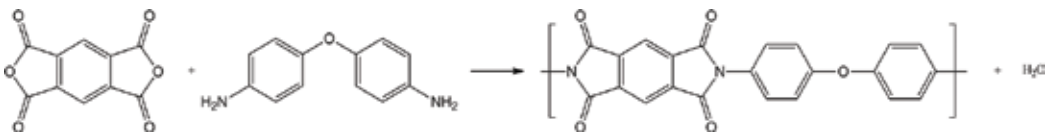

Figure 8. Structural formula of matrix No. 1.

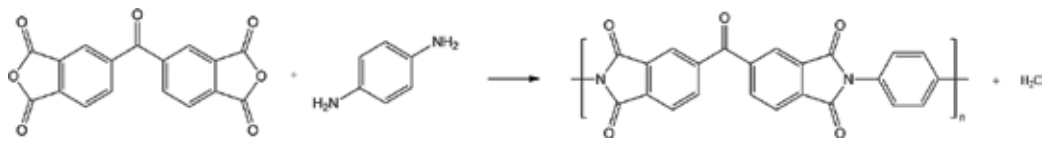

Figure 9. Structural formula of matrix No. 2.

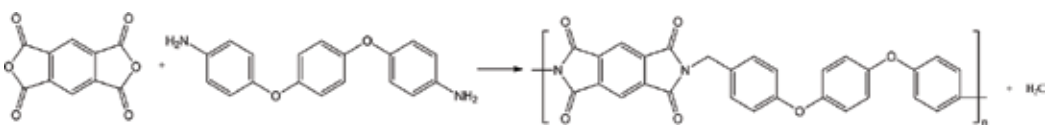

Figure 10. Structural formula of matrix No. 3.

To assess the effect of different inorganic filler contents on the viscosity of the precursor solution, the filler, dianhydride, diamine, and solvent were mixed in such proportions during the experiment so that a 20 wt.% polyamide acid solution was obtained. Precursors were obtained for two kinds of matrices (matrix No. 1 and matrix No. 2).

As can be seen from the data presented in **Figures 11** and **12**, for each filler with different types of modification on different matrices, there are areas of extremum in which, apparently, the percolation limit value for a given filler in a given polymer is found. The filler with the modified surface binds to the matrix with "hard" covalent bonds, and the filler with the unmodified surface is bound to the matrix by the intermolecular Van der Waals interaction, so the maximum value of the viscosity for the latter is much lower.

It can be seen from these graphs that in some cases there are two extrema (matrix No. 1 filler carbon nanotubes and matrix No. 2 filler nanostructured SiC and CNT). Probably, this is due to the fact that the filler content that lies between these peaks somehow inhibits the growth of the polymer chain, which has a very negative effect on the viscosity of the PAA solution.

The increase in the viscosity of PAA when CNT is introduced (more than 0.75 wt.%) is associated with the large surface area of carbon nanotubes, which "swell" in the solvent, and this increases the viscosity of the solution. It negatively affected the physico-mechanical properties of the composites.

4.4.2. Influence of nanosized filler on physicomechanical characteristics of film composite materials

The effect of different contents of nanostructured silicon carbide and carbon nanotubes on the physicomechanical characteristics of the resulting film composite materials was studied.

http://dx.doi.org/10.5772/intechopen.79889

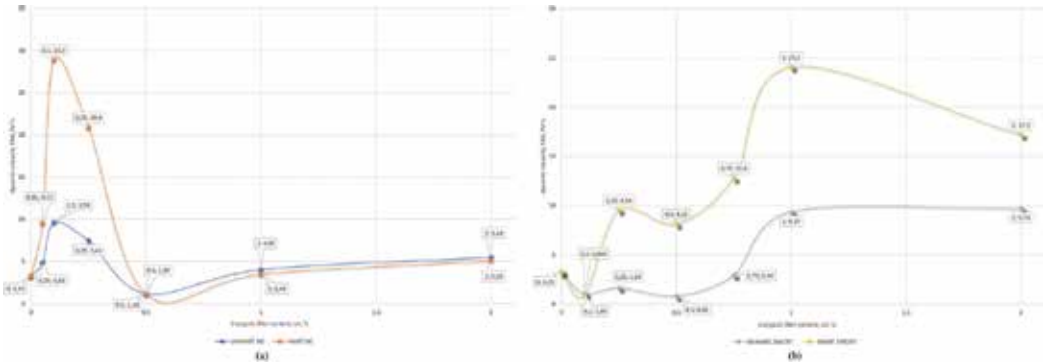

Figure 11. Dependence of the dynamic viscosity of a precursor for a matrix based on polyimide PMDA/ODA on the content of inorganic fillers.

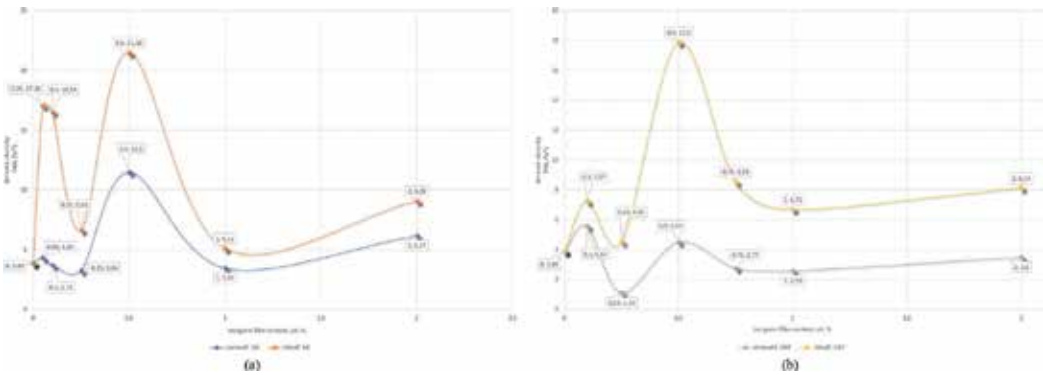

Figure 12. Dependence of the dynamic viscosity of a precursor for a matrix based on polyimide BTDA/pPDA on the content of inorganic fillers.

From the precursor solutions, the films were cast and subjected to stepwise imidization in a vacuum oven at 80°C for 6 hours, then at 150, 200, 250, and 300°C for 1 hour at each temperature and then at 350°C for 15 min.

Film composite materials were also produced on two types of matrices (matrix No. 1 and matrix No. 2).

To assess the effect of nanostructured filler (degree of filling) on strength characteristics, polymer films were tested in terms of basic physicomechanical properties (elongation, tensile strength).

It is established that the strength characteristics of the material are significantly influenced by the introduction of a filler into the polymer system. The effective action of the filler is determined by such factors as the shape and size of the particles, the interaction of the filler particles with the polymer, the interaction between the filler particles in the polymer medium, and the amount of filler.

Based on the data obtained, it can be seen that when the content of the active filler increases to the optimum value, an increase in strength occurs. After achieving the optimum filling, the strength is reduced, and the indicator is subsequently saved at the achieved level. An increase

in the content of filler (more than 1%) promotes the agglomeration of particles, causing significant difficulties in obtaining a homogeneous system; this leads to a deterioration in the physicomechanical parameters.

As can be seen from **Figures 13** and **14**, the type of filler has a significant effect on the nature of the intermolecular interaction. Fillers with a modified surface make it possible to increase the intermolecular interaction, increase the number of intermolecular bonds that carry a mechanical load upon deformation, and also reduce the probability of thermofluctuation rupture of macromolecules in defective areas. From the data obtained, it can be seen that the tensile strength increases significantly in samples containing modified fillers, which is explained by an increase in the dispersibility of the filler particles when the surface is modified. The increase in strength indexes with the use of modified fillers is also associated with an increase in the degree of dispersion of the filler and an increase in the degree of homogeneity of the polyamide acid.

Thus, it was found that the optimal content of nanostructured SiC in the samples PMDA + ODA, BTDA + pPDA is 0.1 wt.%, which provides the maximum increase in tensile strength and elongation at break due to the alignment of internal stresses in the films. For composites with carbon nanotubes based on matrix No. 1, it is 0.25 wt.%, and for matrix No. 2, it is 0.1 wt.%. A different optimum of filling of polymer matrices is associated with different sizes of SiC and CNT particles.

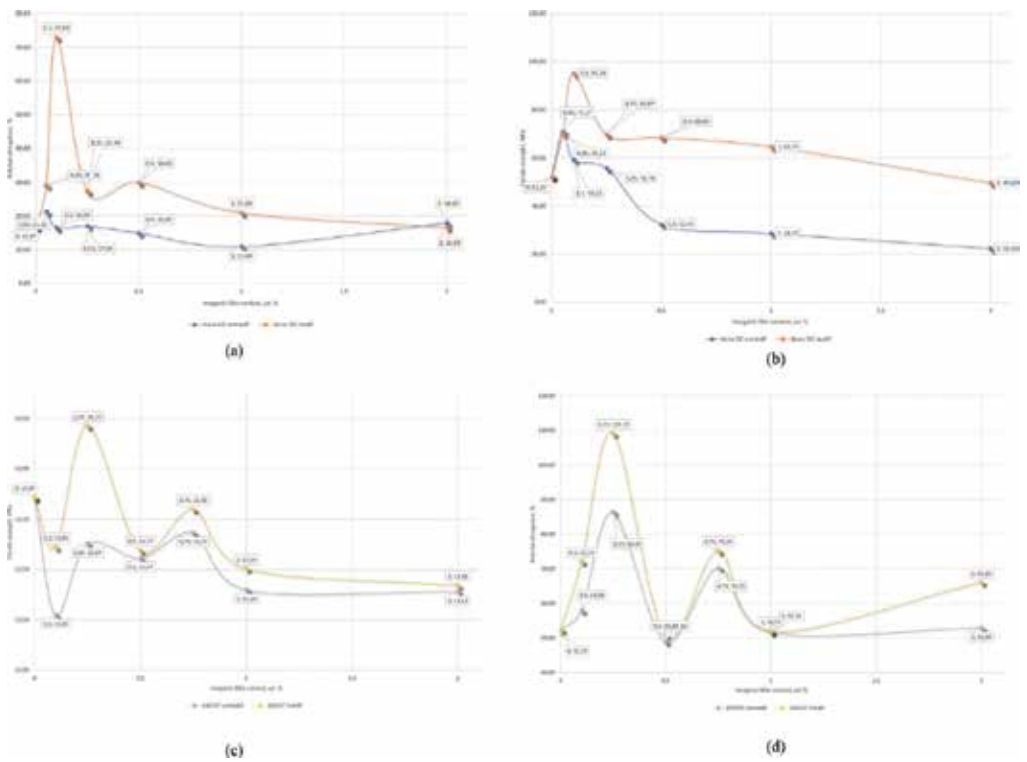

Figure 13. Dependence of physicomechanical properties of the composite based on the PMDA/ODA matrix on the content of the filler.

http://dx.doi.org/10.5772/intechopen.79889

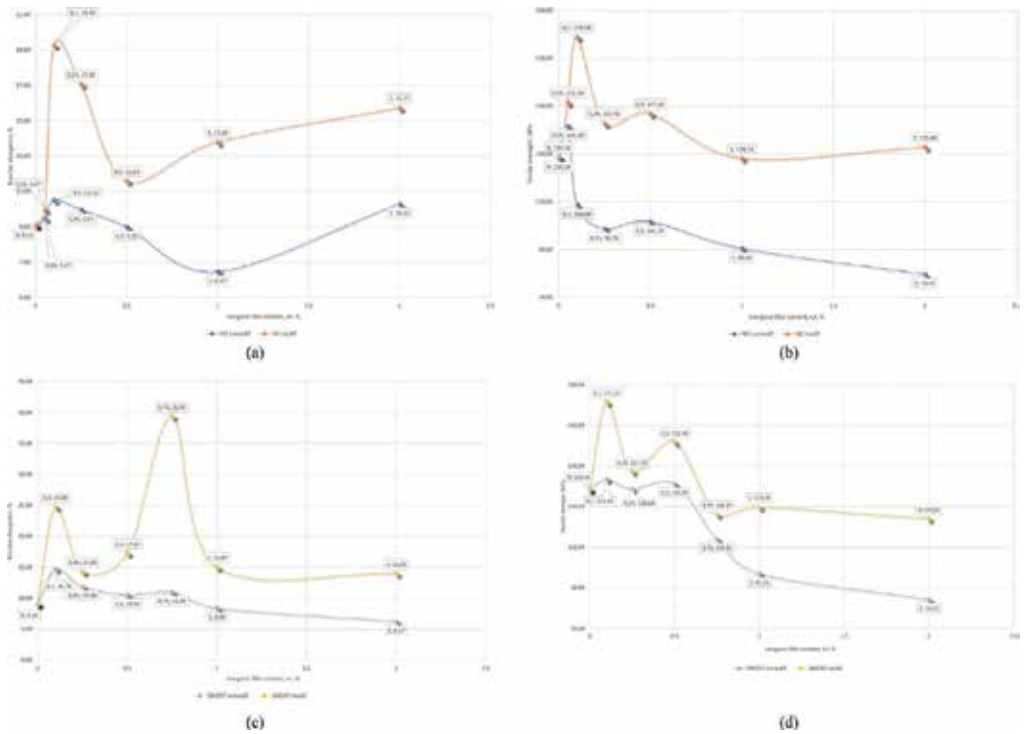

Figure 14. Dependence of physicomechanical properties of the composite based on the BTDA/pPDA matrix on the content of the filler.

4.4.3. Influence of nanosized filler on thermal stability and thermooxidative stability of the resulting composites

The influence of the content of inorganic fillers with modified and unmodified surfaces on the thermal stability in an inert gas atmosphere (argon) and thermooxidative stability in air was studied. Composite materials were obtained in two ways (two-stage method—in the form of films and one-step method—in the form of powders).

Powders of composite materials on three types of matrices were obtained by a one-stage synthesis method (matrix No. 1, matrix No. 2, matrix No. 3).

Due to the low activity of 4-[4-(4-aminophenoxy) phenoxy] phenylamine, it is not possible to obtain a composite based on it by a two-step synthesis.

Two-stage synthesis composites on two kinds of matrices were obtained (matrix No. 1 and matrix No. 2).

To evaluate the effect of nanostructured fillers on thermal stability and thermooxidation stability, differentiation of thermogravimetric curves of the resulting composite materials was carried out, which are registered in an inert and oxidizing atmosphere.

The dependence of thermooxidative stability and thermal destruction of the composite on the content of the filler is shown below in **Figures 15–17**.

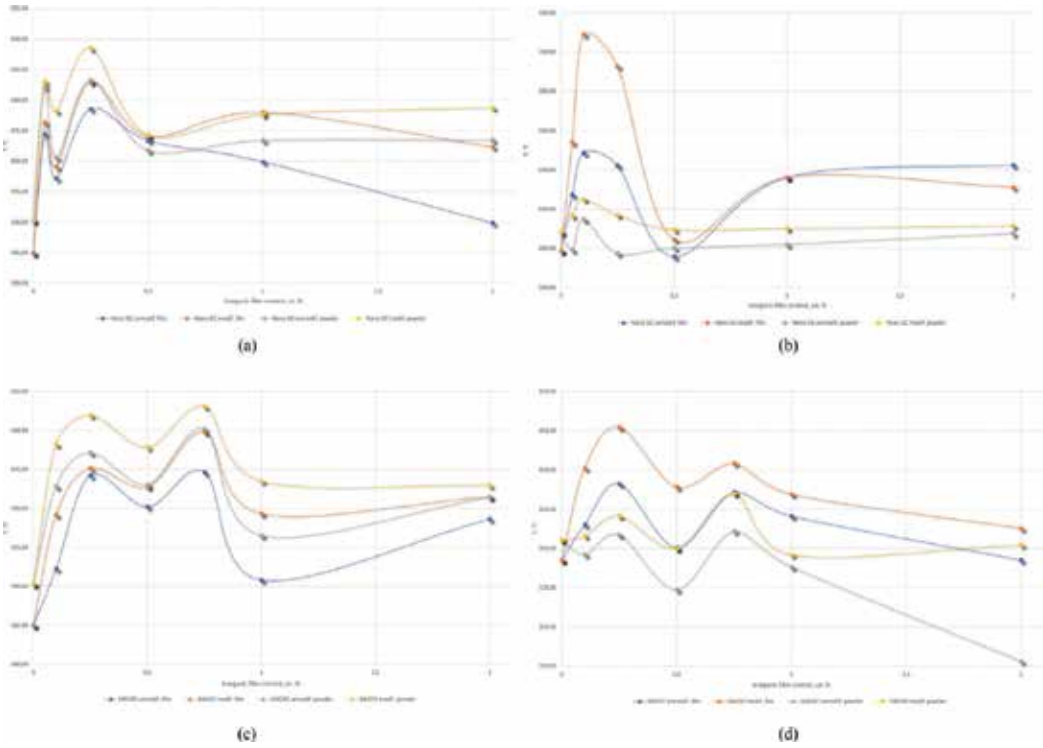

Figure 15. Dependence of thermooxidative stability (left) and thermal destruction (right) of the composite based on the PMDA/ODA matrix on the content of the filler.

The dependence of the effect of carbon nanotubes on thermal stability and thermal oxidation stability of composite materials based on matrix No. 1 is similar to the effect of the introduction of nanostructured silicon carbide. However, in view of the different particle sizes of these fillers, the percolation threshold for carbon nanotubes is higher and the maximum point is 0.75 wt.%. Also, in the case of introducing carbon nanotubes, a decrease in the thermal properties at 0.5 wt.% is observed in all samples with different degrees of surface modification. This is probably due to the fact that with this filler content, it is not possible to obtain a high-molecular weight polymer.

When studying the effect of nanostructured silicon carbide on the properties of thermal stability of composite materials based on No. 2 (BTDA/pPDA) matrix, it was shown that the introduction of this filler into the polymer in a one-step synthesis does not significantly affect the thermooxidative stability of the resulting composite materials, which cannot be said about a two-stage method of production where a maximum is observed with a modified filler content of 0.5 wt.%, and an increase of more than 60°C. The effect of nanostructured silicon carbide on thermal degradation turned out to be completely opposite (**Figure 16**).

Due to the high thermal and oxidative stability of matrix No. 2, the introduction of carbon nanotubes affects negatively this parameter, and it decreases with increasing filler content. At the same time, the influence of the content of CNTs with different degrees of surface modification on the thermal destruction of a composite based on the BTDA/pPDA matrix can be

http://dx.doi.org/10.5772/intechopen.79889

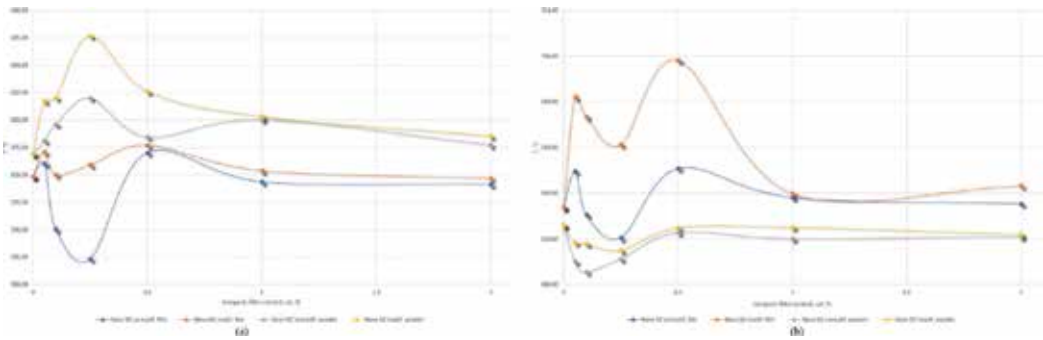

Figure 16. Dependence of thermooxidative stability (left) and thermal destruction (right) of the composite based on the BTDA/pPDA matrix on the content of nanostructured silicon carbide.

described as follows. The graph has a maximum at 0.75 wt.%, which corresponds to the percolation threshold of carbon nanotubes in this matrix; this does not depend on the degree of modification of the filler nor on the method of its preparation (**Figure 17**).

To confirm the revealed regularities, the effect of nanostructured silicon carbide and carbon nanotubes on a polyimide matrix with a more "flexible" structure, which is matrix No. 3 (PMDA/AFFA), was studied.

It was shown that the percolation threshold with the introduction of nanoSiC is in the range of 0.05 wt.% and there is a significant increase in thermooxidative stability and resistance to thermal destruction of powders of composites obtained by a single-step process. The addition of carbon nanotubes to matrix No. 3 also increases these material properties up to 0.75 wt.%, with a decrease in these parameters at 0.5 wt.%, which was also observed in other experiments.

As can be seen from the presented data, the effect of nanostructured silicon carbide and carbon nanotubes on different matrices is very different, but practically does not depend on the method of obtaining the composite material. The difference exists only in the numerical value

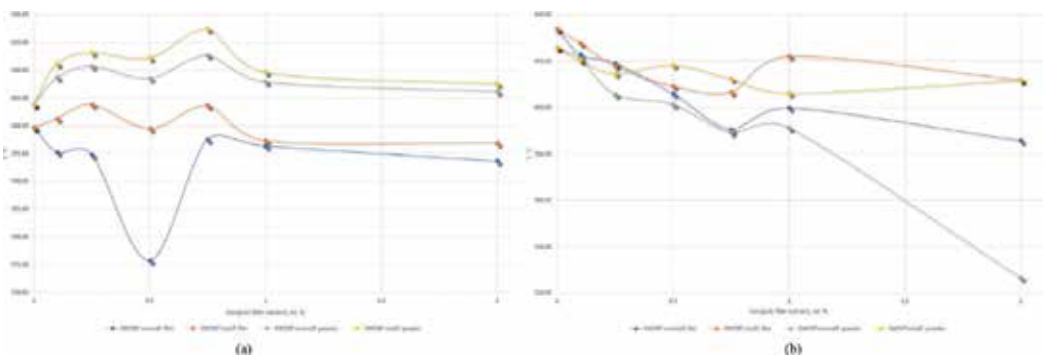

Figure 17. Dependence of thermooxidative stability (left) and thermal destruction (right) of the composite based on the BTDA/pPDA matrix on the content of nanostructured carbon nanotubes.

of the parameter being determined, but not in the character of the curve and the extremum points.

Thus, it was found that to increase thermal and oxidative stability and resistance to thermal degradation:

- for matrix No. 1, the optimal content of nanostructured silicon carbide is 0.1 wt.%, and for carbon nanotubes, it is 0.25 wt.%;
- for matrix No. 2, the extremum content of nanostructured silicon carbide is 0.05 and 0.5 wt.%, and for carbon nanotubes, it is 0.25 and 0.75 wt.%;
- for matrix No. 3, the optimal content of nanostructured silicon carbide is 0.05 wt.%, and for carbon nanotubes, it is 0.25 and 0.75 wt.%.

5. Conclusion

In this chapter, we compared the properties of composite materials based on nanostructured silicon carbide and carbon nanotubes with modified and unmodified surfaces obtained on three types of polyimide matrices (matrix No. 1 based on pyromellitic dianhydride and 4,4′-oxydianiline; matrix No. 2 based on 3,3′,4,4′-benzophenone tetracarboxylic acid dianhydride and p-phenylenediamine; and matrix No. 3 based on pyromellitic dianhydride and 4-[4-(4-aminophenoxy) phenoxy] phenylamine).

The influence of different amounts of nanostructured silicon carbide and carbon nanotubes on the viscosity of the intermediate precursor (polyamide acid solution), as well as the thermal stability and mechanical properties of final composites based on the polyimide binder, was obtained and tested on three types of polyimide matrices.

It was found that for composites based on nanostructured silicon carbide and carbon nanotubes, the optimal content of inorganic filler is the interval for silicon carbide from 0.05 to 0.1 wt.%, for single-walled carbon nanotubes from 0.1 to 0.75 wt.%.

It was found that the effect of inorganic fillers on the properties obtained by thermal imidization in a high-temperature solvent of powders of composite materials depends to a large extent on the chemical nature of the polyimide matrix. The influence of the inorganic filler on the properties of the film composite material obtained by the stepwise high-temperature imidization in a vacuum medium is the same and practically independent of the structure of the matrix.

Acknowledgements

Applied researches are carried out with state financial support by the Ministry of Education of Russia under the Agreement on granting subsidies No. 14.625.21.0037 of October 3, 2016 and unique identifier for Applied Scientific Researches (project) RFMEFI62516X0037.

Author details

Anton Yegorov*, Marina Bogdanovskaya, Vitaly Ivanov, Olga Kosova, Kseniia Tcarkova, Vasily Retivov and Olga Zhdanovich

*Address all correspondence to: egorov@irea.org.ru

The Federal State Unitary Enterprise, Institute of Chemical Reagents and High Purity Chemical Substances of National Research Centre «Kurchatov Institute» (NRC «Kurchatov Institute» – IREA), Moscow, Russian Federation

References

[1] Zou H, Wu S, Shen J. Polymer/silica nanocomposites: Preparation, characterization, properties, and applications. Chemical Reviews. 2008;**108**:3893-3957. DOI: 10.1021/cr068035q

[2] Wang PJ, Lin CH, Chang SL, Shih SJ. Facile, efficient synthesis of a phosphinated hydroxyl diamine and properties of is high-performance poly(hydroxylimides) and polyimide–SiO_2 hybrids. Polymer Chemistry. 2012;**3**:2867-2874. DOI: 10.1039/C2PY20156A

[3] Agag T, Koga T, Takeichi T. Studies on thermal and mechanical properties of polyimide–clay nanocomposites. Polymer. 2001;**42**:3399-3408. DOI: 10.1016/S0032-3861(00)00824-7

[4] Zhu J, Wei S, Haldolaarachchige N, Young DP, Guo Z. Electromagnetic field shielding polyurethane nanocomposites reinforced with core–shell Fe–silica nanoparticles. The Journal of Physical Chemistry C. 2011;**115**:15304-15310. DOI: 10.1021/jp2052536

[5] Kobayashi Y, Katakami H, Mine E, Nagao D, Konno M, Liz-Marzan LM. Silica coating of silver nanoparticles using a modified Stöber method. Journal of Colloid and Interface Science. 2005;**283**:392-396. DOI: 10.1016/j.jcis.2004.08.184

[6] Bessonov MI, Koton MM, Kudryavcev BB, Lajus LA. Poliimidy – klass termostojkih polimerov. Nauka. 1983;**310**:5-80 (Russian)

[7] Hsiao SH, Chen YJ. Structure–property study of polyimides derived from PMDA and BPDA dianhydrides with structurally different diamines. European Polymer Journal. 2002;**38**:815-828. DOI: 10.1016/S0014-3057(01)00229-4

[8] Liaw DJ, Wang KL, Huang YC, Lee KR, Lai JY, Ha CS. Advanced polyimide materials: Syntheses, physical properties and applications. Progress in Polymer Science. 2012; **37**:907-974. DOI: 10.1016/j.progpolymsci.2012.02.005

[9] Myakin SV, Sychev MM, Zagranichek AL, Vasil'eva IV. Issledovanie radiacionnoj stojkosti plenok poliimida pod vozdejstviem vysokih doz uskorennyh ehlektronov. Tekhnologiya vysokomolekulyarnyh soedinenij. (Russian)

[10] Shigeta M, Komatsu M, Nakashima N. Individual solubilization of single-walled carbon nanotubes using totally aromatic polyimide. Chemical Physics Letters. 2006;**418**:115-118. DOI: 10.1016/j.cplett.2005.10.088

[11] Park C, Ounaies Z, Watson KA, Crooks RE, Smith J, Lowther SE, Connell JW, Siochi EJ, Harrison JS, Clair TLS. Dispersion of single wall carbon nanotubes by in situ polymerization under sonication. Chemical Physics Letters. 2002;**364**:303-308. DOI: 10.1016/S0009-2614(02)01326-X

[12] Smith JG, Connell JW, Delozier DM, Lillehei PT, Watson KA, Lin Y, Zhou B, Sun YP. Space durable polymer/carbon nanotube films for electrostatic charge mitigation. Polymer. 2004;**45**:825-836. DOI: 10.1016/j.polymer.2003.11.024

[13] Smith JG, Delozier DM, Connell JW, Watson KA. Carbon nanotube–conductive additive-space durable polymer nanocomposite films for electrostatic charge dissipation. Polymer. 2004;**45**:6133-6142. DOI: 10.1016/j.polymer.2004.07.004

[14] Watson KA, Ghose S, Delozier DM, Smith JG, Connell JW. Transparent, flexible, conductive carbon nanotube coatings for electrostatic charge mitigation. Polymer. 2005;**46**:2076-2085. DOI: 10.1016/j.polymer.2004.12.057

[15] Delozier DM, Watson KA, Smith JG, Clancy TC, Connell JW. Investigation of aromatic/aliphatic polyimides as dispersants for single wall carbon nanotubes. Macromolecules. 2006;**39**:1731-1739. DOI: 10.1021/ma051826u

[16] Hill D, Lin Y, Qu L, Kitaygorodskiy A, Connell JW, Allard LF, Sun YP. Functionalization of carbon nanotubes with derivatized polyimide. Macromolecules. 2005;**38**:7670-7675. DOI: 10.1021/ma0509210

[17] Qiao-Hui G, Xiao-Ping Z, Su-Qin W, Hong-Wei F, Yong-Hong L, Hao-Qing H. Heat-resistant polyimide electrical conductive composites. Polymer Materials Science and Engineering. 2009;**25**:52-54

[18] Rittenhouse TL, Bohn PW, Hossain TK, Adesida I, Lindesay J, Marcus A. Surface state origin for the blue shifted emission in anodically etched porous silicon carbide. Journal of Applied Physics. 2004;**95**:490-496. DOI: 10.1063/1.1634369

[19] Fan JY, Wu XL, Kong F, Qiu T, Huang SG. Luminescent silicon carbide nanocrystallites in 3C-SiC/polystyrene films. Applied Physics Letters. 2005;**86**:171903. DOI: 10.1036/1.1914962

[20] Guo Z, Kim TY, Lei K, Pereira T, Sugar JG, Hahn HT. Strengthening and thermal stabilization of polyurethane nanocomposites with silicon carbide nanoparticles by a surface initiated-polymerization approach. Composites Science and Technology. 2008;**68**:164-170. DOI: 10.1016/j.compscitech.2007.05.031

[21] Bazzar M, Ghaemy M. 1,2,4-Triazole and quinoxaline based polyimide reinforced with neat and epoxide-end capped modified SiC nanoparticles: Study thermal, mechanical and photophysical properties. Composites Science and Technology. 2013;**86**:101-108. DOI: 10.1016/j.compscitech.2013.07.005

[22] Zheng HF, Li ZH, Zhu YM. High performance composite of silicon carbide/bismaleimide. Key Engineering Materials. 2007;**336**:1377-1379. DOI: 10.4028/www.scientific.net/KEM.336-338.1377

[23] Berlina AA. Polimernye kompozicionnye materialy: struktura, svojstva, tekhnologiya: ucheb. posobie. SPb.: CO «Professiya»; 2014. p. 592 (Russian)

[24] Xia H, Wang Q, Qiu G. Polymer-encapsulated carbon nanotubes prepared through ultrasonically initiated in situ emulsion polymerization. Chemistry of Materials. 2003;**15**:3879-3886. DOI: 10.1021/cm0341890

[25] Suslick KS. Sonochemistry. Science. 1990;**247**:1439-1445. DOI: 10.1126/science.247.4949.1439

[26] Andrews R, Jacques D, Minot M, Rantell T. Fabrication of carbon multiwall nanotube/polymer composites by shear mixing. Macromolecular Materials and Engineering. 2002;**287**: 395-403. DOI: 10.1002/1439-2054(20020601)287:6<395::AID-MAME395>3.0.CO;2-S

Chapter 7

Synthesis and Characterization of Polymeric Material Consisting on Acrylamide Catalyzed by Maghnite (Algerian MMT) under Microwave Irradiation

Rahmouni Abdelkader and Belbachir Mohammed

Additional information is available at the end of the chapter

http://dx.doi.org/10.5772/intechopen.80033

Abstract

Intercalation of acrylamide into interlayer spaces of natural montmorillonite called maghnite (Algerian MMT) by the free solvent polymerization technique under microwave irradiation was studied. The transformation was carried out with using both the raw (maghnite-Na fin) and treated clay (maghnite-Na^+ fin) in aqueous sodium hydroxide NaOH solution (1 M). It was shown that no initial modification of the layered mineral (by ion-exchange with Na^+ cations or organophilization) is needed for the successful introduction of anionic hydrogels into the interlayer gallery. The goal of the present study was to synthesis anionic polyacrylamide/maghnite composite with similar composition and structure to that synthesized of other catalyst. Maghnite catalyst has a significant role in the industrial scale. In fact, the use of maghnite is preferred for its many advantages: a very low purchase price compared to other catalysts, the easy removal of the reaction mixture. The anionic sodium-clay polyacrylamide material exhibited a tendency to the formation of exfoliated structure. The synthesized hydrogels, as monitored by the swelling behavior were characterized by Fourier transform infrared and ^{1}HNMR analysis.

Keywords: green catalysis, anionic polyacrylamide, hydrogel, maghnite-H^+, microwave irradiation, cationic polyacrylamide

1. Introduction

Green chemistry for chemical synthesis addresses our future challenges in working with chemical processes and products by inventing novel reactions that can maximize the desired products and minimize by products [1], designing new synthetic schemes and apparatus that

can simplify operations in chemical productions [2] and seeking greener solvents that are inherently environmentally and ecologically benign [3]. In addition, a desirable green solvent should be natural [4, 5], nontoxic [6, 7], cheap and readily available with additional benefits of aiding the reaction, separation or catalyst recycling. Most of the cationic initiators used in the synthesis of polymers and copolymers are expensive. They may be poisoned by products of the reaction or impurities present in the monomer feed, and contain heavy metals, such as chromium, mercury, antimony, etc., that presents environmental disposal problems for the user. As clay catalysts, montmorillonite a class of inexpensive and non-corrosive solid acids, have been used as efficient catalysts for organic reactions. Montmorillonite catalysts are easily recovered and reused [8]. In continuation of our studies on environmentally and green methods using solid supports, we report that acid-exchanged montmorillonite Mag-H+ is a novel and efficient solid catalyst for the synthesis of anionic polyacrylamide from acrylamide monomer. In contrast to the more usually used catalyst, maghnite-H^+ can be easily separated from the polymer and regenerated by heating to a temperature above 100–105°C [9]. Microwave irradiation has been widely used in the synthesis of organic–inorganic hybrid materials because of its well-known advantages over conventional synthetic route towards well defined PAm (polyacrylamide) containing polymers include living anionic [10] and group transfer [11] polymerization techniques, both operating using protected analogues of the acrylamide monomers. However, traditional polymerization techniques show some practical disadvantages (e.g. requirement for extremely pure reagents, low functional group tolerance, limited combination with other monomers or polymer segments...). It has long been known that molecules undergo excitation with electromagnetic radiation. This effect is utilized in household microwave ovens to heat up food. However, chemists have only been using microwaves as a reaction methodology for a few years. Some of the first examples gave amazing results, which led to a flood of interest in microwave accelerated synthesis. Microwave heating has been found to be particularly advantageous for reactions under "dry" media. Enormous accelerations in reaction time can be obtained if overheating is carried out in closed containers under high pressure; a reaction which takes several hours under conventional conditions can be completed in a few minutes, in addition in the absence of solvent on a solid support with or without a catalyst, it offers a certain number of advantages: the solvents are often expensive, toxic, difficult to in the case of high-boiling aprotic solvents [12]. Moreover, the absence of solvent reduces the risk of explosions when reaction takes place in a microwave oven [13]. Reactions under "dry" conditions were originally developed in the late 1980s [14]. Synthesis without solvents under microwave irradiation offers several advantages [15]. The absence of solvent reduces the risk of explosions when the reaction takes place in a closed vessel in an oven [16]. Moreover, aprotic dipolar solvents with high boiling points are expensive and difficult to remove from the reaction mixtures [17]. During microwave induction of reactions under dry conditions, the reactants adsorbed on the surface of alumina, silica gel, clay [18]. Consequently, such supported reagents efficiently induce reactions under safe and simple conditions with domestic microwave ovens instead of specialized expensive commercial microwave systems [9]. Many researchers have studied cationic copolymerization of anionic polyacrylamide using "H_2O"/KPS initiator system and CH_2Cl_2 solvent [19, 20]. Frequently, these initiators require the use of very high or very low temperature and high pressures during the polymerization reaction. The separation of the initiators from the polymer is not always possible. Therefore, the presence of toxic initiators presents problems in the manufacture of polymers used especially in medical and veterinary procedures.

http://dx.doi.org/10.5772/intechopen.80033

There is still a great demand for heterogeneous catalysis under mild conditions and in environmentally friendly processes. Montmorillonite, a class of inexpensive and noncorrosive solid acids, have been used as efficient catalysts for a variety of organic reactions. The reactions catalyzed by montmorillonite are usually carried out under mild conditions with high yields and high selectivity's, and the workup of these reactions is very simple; only filtration to remove the catalyst and evaporation of the solvent are required. Montmorillonite catalysts are easily recovered and reused [21, 22]. The purpose of this paper is to study the polymerization of anionic acrylamide catalyzed by maghnite-H^+ as proton exchanged montmorillonite clay. This new non-toxic cationic catalyst has exhibited higher efficiency via the polymerization of vinylic and hetero-cyclic monomers [18, 19]. This catalyst can be easily separated from the polymer product and regenerated by heating at a temperature above 100°C [23]. The effects of different synthesis parameters, such as the amount of maghnite-H^+, the molar ratio (acrylamide/maghnite), reaction time, on the yield of polymerization are discussed together with the mechanism of polymerization.

2. Experimental section

2.1. Microwave apparatus

Microwave irradiation was performed in a single mode focused CEM reactor (Model Discover, CEM Co., Matthew, NC) operating at 2.45 GHz with ability to control output power. Temperature in the system was measured by a fiber optic temperature sensor preventing interaction with MWs and influence on the temperature reading. The heat capacity Cp of the solution was approximated as the heat capacity of water. All experiments were done under the same conditions by keeping constant irradiation power, temperature, and initial reaction mixture volume (12 mL). With the experimental design that was used, the temperature was maintained at 160°C in all experiments. The experimental equipment of microwave irradiation taking place is shown in **Scheme 1**.

2.2. Materials

All reagents in this work were of analytical grade and used as received without further purification. NaOH (98%) was used as the initiator, which was obtained from Sigma Aldrich (French). The maghnite-Na^+ (MMT-Na^+) used in this work came from a quarry located in Maghnia (North West of Algeria) and was supplied by the company "ENOF" (Algerian manufacture specialized in the production of nonferric products and useful substances). The chemical composition, structure of the MMT-Na^+ and comparison with American and French MMT were shown in (**Tables 1** and **2** and **Figure 1**). The cation exchange capacity (CEC) and

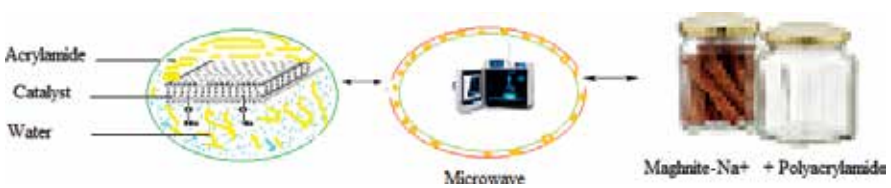

Scheme 1. Experimental equipment of microwave irradiation for synthesis of anionic polyacrylamide (APAm).

surface area of the clay was found to be 84 mEq (100 g^{-1}) of dried clay and 786 m^2 g^{-1} respectively, and its X-ray diffraction (XRD) analysis shows that the interlayer spacing of MMT-Na^+ is 1.29 nm [26].

2.3. Physical and chemical characterization of Maghnite

This clay has been characterized to determine the moisture content, pH, swelling, colloidality, loss on ignition and cation exchange capacity.

2.3.1. Humidity rate

The protocol consists in drying a sample of 20 g of maghnite (W_0) in the oven at 105°C for 24 h; the weight (W_1) is the weight of the dry sample. The moisture content (H% weight) is given by the following formula (i) [27].

$$H(\%) = (W_0 - W_1)/W_0 \times 100 \quad (1)$$

where W_0 = weight initial and W_1 = weight after drying.

When weight of catalyst is stoped 24 h at (9.50 and 9.72) for maghnite (100 μm) and maghnite (200 μm) respectively, we can calculate the humidity rate according to the formula (1).

Maghnite (100 μm): H (%) = $(W_0 - W_1)/W_0 \times 100 = (20–19.5)/20 \times 100 = 2.5\%$.

Maghnite (200 μm): H (%) = $(W_0 - W_1)/W_0 \times 100 = (20–19.72)/20 \times 100 = 1.4\%$.

The results obtained allow us to draw two conclusions:

- The humidity rate depends on the diameter of the maghnite (MMT).
- The second conclusion allows us to say that the maghnite it's no hygroscopic as show in (**Table 3**).

Sample	SiO_2	Al_2O_3	$F_{e2}O_3$	CaO	MgO	Na_2O	K_2O	TiO_2	SO_3	PF*
Raw-Mag	69.39	14.67	1.16	0.30	1.07	0.50	0.79	0.16	0.91	11
Mag-H^+	71.70	14.03	0.71	0.28	0.80	0.21	0.77	0.15	0.34	11

*PF: Pert in fire [24].

Table 1. Elementary compositions of protons exchanged samples "maghnite" (compositions wt%).

Sample	SiO_2	Al_2O_3	Fe_2O_3	FeO	CaO	MgO	Na_2O	K_2O	TiO_2	SO_3
Wyoming (USA) (%)	50.04	20.16	0.68	00	1.46	0.23	Tr	1.27	00	00
Vienne (France) (%)	57.49	20.27	2.92	0.19	0.23	3.13	1.32	0.28	0.12	00
Raw-Mag (Algeria) (%)	69.39	14.67	1.16	00	0.30	1.07	0.5	0.79	0.16	0.91
Mag-H^+ (Algeria) (%)	71.7	14.03	0.71	00	0.28	0.80	0.21	0.77	0.15	0.34

Table 2. Comparison in the composition (in %) of American, French and Algerian MMT [19].

http://dx.doi.org/10.5772/intechopen.80033

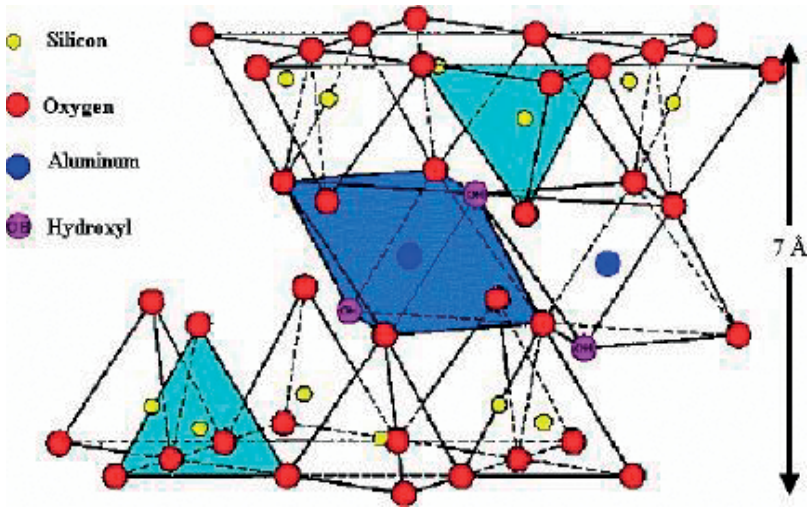

Figure 1. Crystallographic structure of maghnite (basic repeating unit is $[Si_4O_{10}Al^{3+}(2-x)Mg^{2+}x(OH)_2])$ [25] .

	S_1	S_2	S_3	S_4	S_5	S_6
Maghnite (100 µm)	19.56	19.53	19.49	19.51	19.50	19.50
Maghnite (200 µm)	19.82	19.79	19.70	19.72	19.72	19.72

Table 3. The weight obtained after 24 h of steaming stabilized.

Sample	pH
Distilled water	7.00
Maghnite (100 µm)	9.90
Maghnite (200 µm)	10.23

Table 4. The pH results obtained at room temperature.

2.3.2. pH measurement

Our method for pH measurement consists of stirring 10 g of maghnite (MMT) with 500 mL of distilled water for 20 min. After 24 h, the pH of the support is measured using a pH meter. The pH results obtained at room temperature show us a great basicity of the samples studied compared with distilled water. This may be due to carbonates, alkaline bicarbonates or silicates which usually go into the composition of the maghnite (MMT) as shown in **Table 4**.

3. Preparation of catalyst

The preparation of the "maghnite-H^+ 0.25 M" was carried out by using a method similar to that described by Belbachir and coworkers [28]. Indeed, the raw-maghnite (20 g) was crushed

for 20 min using a Prolabo ceramic balls grinder. It was then dried by baking at 105°C for 2 h. The maghnite was then weighed and placed in an Erlenmeyer flask together with 500 ml of distilled water. The maghnite/water mixture was stirred using a magnetic stirrer and combined with 0.25 M of sulfuric acid solution, until saturation was achieved over 2 days at room temperature, the mineral was washed with distilled water until it became sulfate free, and then dried at 105°C [29, 30].

4. Characterization spectroscopic and thermal of catalyst

The best value of copolymer yield was obtained with maghnite-H^+ 0.25 M, in which there is a complete saturation of montmorillonite with protons without destruction of catalyst structure [31]. Maghnite-H^+ was found to have a BET surface area (SSA) of 59.45 m^2/g, an average pore diameter of 62.46 Å and total pore volume of 0.00772 cm^3/g. The SSA of maghnite-H^+ is close to that (61 m^2/g) obtained by Belbachir et al. [32] for montmorillonite.

After the activation process and filtration, the samples were washed until pH close to 7 and dried at 105°C overnight. According to experimental data, chemical composition of clay varies with the H_2SO_4 concentration. Two regions can be revealed. In the region of 0.05–0.15 M H_2SO_4 the change of Si/Al molar ratio is a small-scale due to the leaching of interlayer Ca^{2+}, Mg^{2+} and Na^+ cations by H_2SO_4. At the same time when H_2SO_4 concentration is higher than 0.2 M the change of Si/Al molar ratio is pronounced that can be related to the dissolution of Al^{3+} cations from the octahedral sheet. Effect of the acid activation on the textural properties is also confirmed by XRD method. The X-ray of the samples are shown in **Figure 2a** and **b**. The position of the basal (001) reflection, i.e. interlayer distance, strongly depends on the H_2SO_4 concentration. The increasing H_2SO_4 concentration from 0.05 to 0.25 M leads to increase the basal spacing, from 12.5 to 15.0 Å. However the basal spacing decreases again for higher acid concentrations. Probably, this phenomenon can be attributed to the "cleaning" of the solid due to the elimination of possible soluble impurities and the substitution of interlayer ions (Na^+ and Ca^{2+}) by H^+.

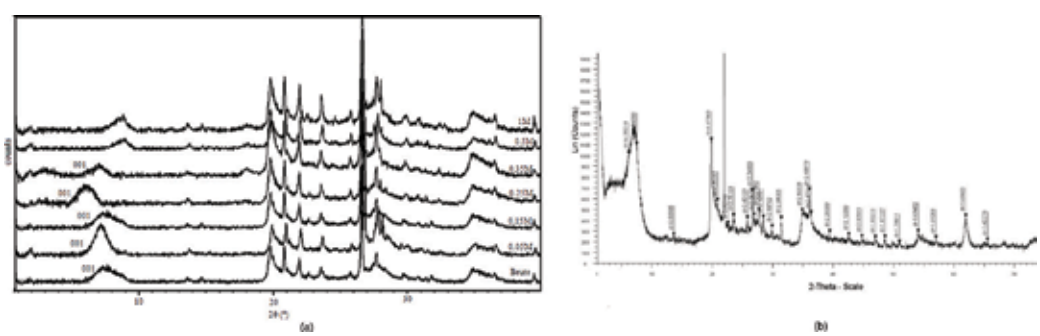

Figure 2. (a) XRD pattern of raw maghnite and activated maghnite (maghnite-H^+) [33] and (b) XRD profiles of maghnite-Na^+ [34].

http://dx.doi.org/10.5772/intechopen.80033

The thermal characterizations of the catalyst include thermogravimetric analysis (TGA). **Figure 3** shows the weight losses (%) versus temperature (°C) curves for pure maghnite-Na^+. The TGA of pure maghnite-Na^+ show two stages of weight loss. The first weight loss in Na^+-Mag below 100°C is a result of the release of free water. The second weight loss around 600°C is associated with the dehydroxylation of silicate structure [35]. The total weight loss is only 13.94% up to 800°C. As can be expected, maghnite-Na^+ shows a high thermal stability.

Figure 4 shows the characteristic FT-IR spectra of Magh-Na^+ and Magh-H^+. The characteristic absorption peaks of MMT are assigned to the Si–O–Si skeleton vibration at 1043–1116 cm^{-1}, the strong absorption bands of Si–O and Al–O bending vibration at 525–628 cm^{-1} and the OH stretching vibration at 3425 cm^{-1} [36, 37].

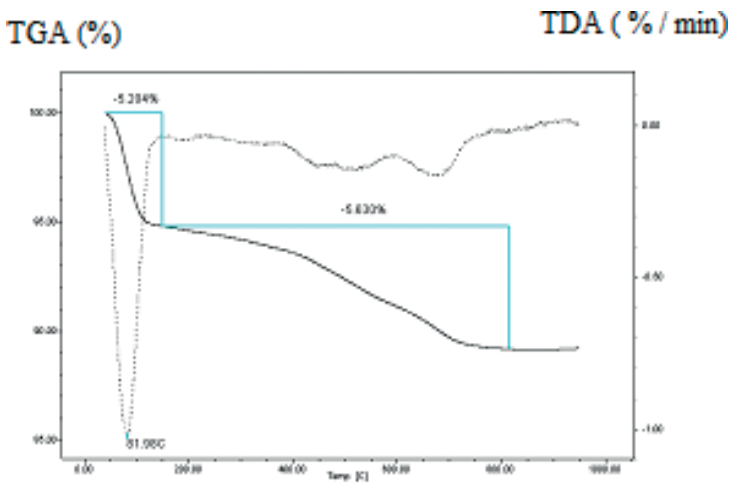

Figure 3. TGA curves of a maghnite-Na^+ obtained in nitrogen atmosphere at heating rate of 10°C/min.

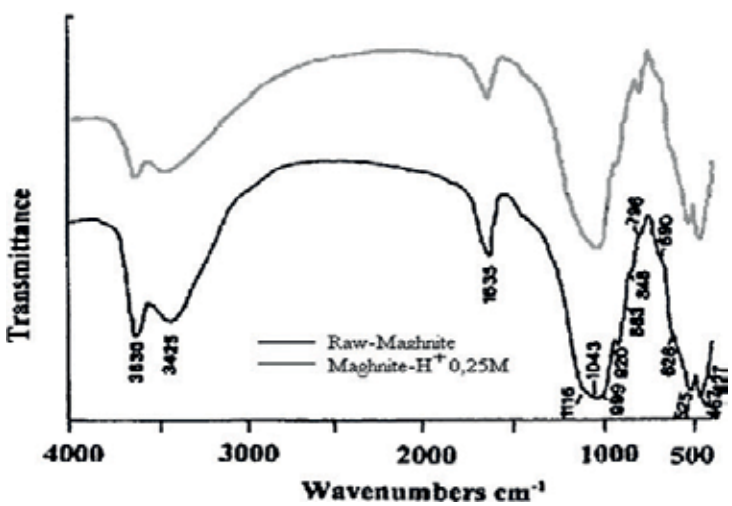

Figure 4. FTIR spectra of raw-maghnite and maghnite-H^+.

5. Synthesis of polymeric material

A solution of 2 g of acrylamide containing 0.5 M of sodium hydroxide (NaOH) was prepared and (2 w%) of maghnite-Na^+ (Algerian MMT) was then added. The mixture of (Am, maghnite-Na^+ and NaOH) was put into a flask with 100 mL and stirred to allow proper mixing. The mixture was subjected to several short burst of microwave irradiation using a microwave oven at frequency of 2.45 GHz at power output of 200 W. The reaction mixture was then submitted to microwave irradiation at 160°C and for 4 min. The mixture was cooled (4–10 min at room temperature), filtered and washed extensively with distilled water and methanol to remove any unreacted acrylamide until the washing solution became neutral and air dried. The reaction taking place is shown in **Scheme 2**.

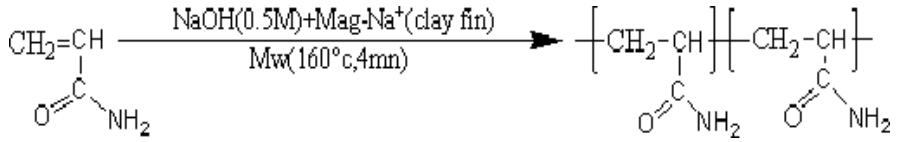

Scheme 2. Synthesis of anionic polyacrylamide (APAm) induced by maghnite-Na^+ (2 wt%) under microwave irradiation.

6. Results and discussion

Under conventional conditions (CS), the polymer was produced with 75% yield after 5 h, if the reaction was continued the yield was 87.6% after 24 h at ambient temperature. By contrast, under microwave irradiation the material was produced with the remarkable yield 80.56% after only 2 min after the beginning of the reaction, and 92.58% after 20 min at ambient temperature.

6.1. Spectroscopic characterization

The functional groups of the synthesized product were investigated by Fourier transform infrared spectrophotometer. The spectrums of the product confirm the existence of the carbonyl and amide functionalities. **Figures 5** and **6** show the FTIR spectra for the final product and the monomer. The peaks at 3191–3331 cm^{-1} were due to amine group, whereas, the absorption peak at 1651 cm^{-1} is strong and sharp and is attributed to the carbonyl (C═O) of the carboxyl group [38]. The peaks at 2868.68 and 2909.55 and 2931.10 cm^{-1} are assigned to υ-CH_2 [39].

The ^1H NMR spectrum of (APAm) induced by maghnite-Na^+ (2 wt%) under microwave irradiation was recorded in deuterated deionized water (D_2O) solution using a Bruker Avance 300 MHz Spectrometer. Chemical shifts (δ) were given in ppm with tetramethylsilane (TMS) as a standard. **Figure 7** represents ^1H NMR spectrum of APAm, which was obtained from purified polymer dispersion. The ^1H NMR spectrum was in accordance with the proposed structures of the product. The Methylene group of APAM was observed at 1.20–1.40 ppm and (CH) group from APAm appeared at 2.40–2.60 ppm. The strong peaks of 4.60–4.80 ppm were attributed to the solvent (D_2O) [40, 41].

http://dx.doi.org/10.5772/intechopen.80033

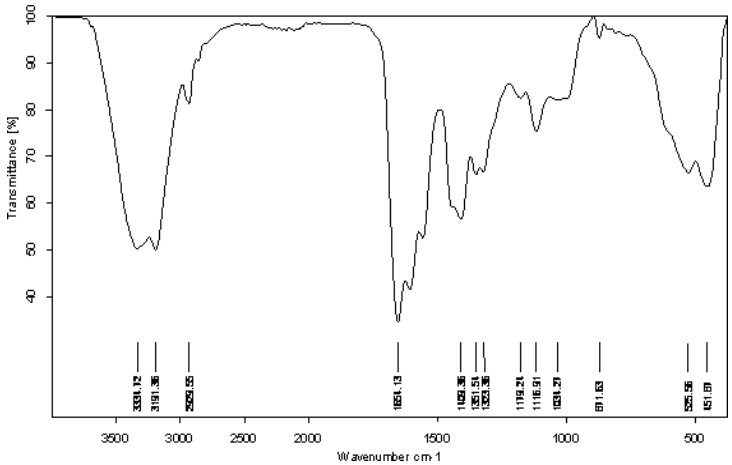

Figure 5. FTIR spectrum of anionic polyacrylamide (APAm) induced by maghnite-Na^+ (5 wt%) under microwave irradiation.

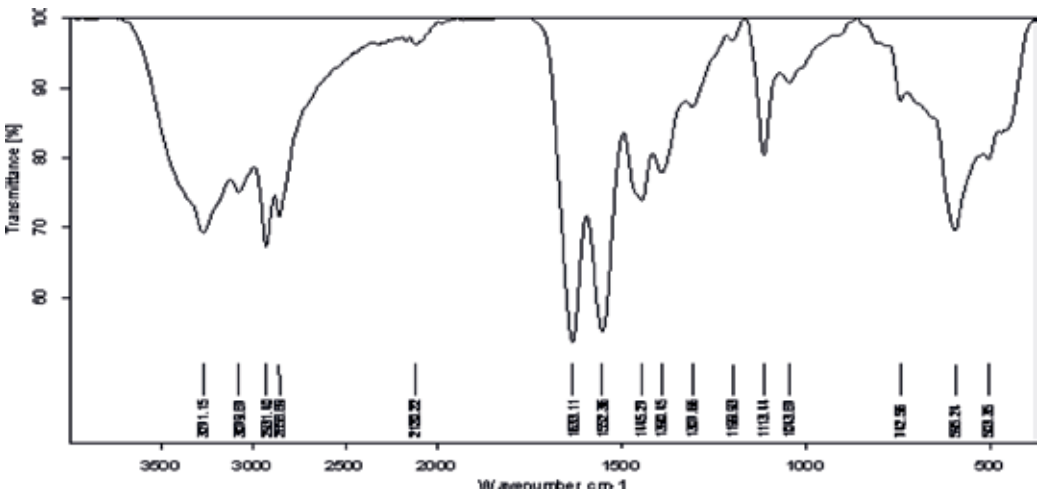

Figure 6. FTIR spectrum of acrylamide (Am).

A thermal property of anionic polyacrylamide was characterized by TGA. According to **Figure 8**, crude dry particles were obtained by removing free water and solvent isothermally at 110°C. As the nonpolar solvent used to wash the products, chloroform would be expected to constitute the major part of volatile solvents since it could remain absorbed during synthesis but was not observed [42]. There are three main thermal degradations of the anionic polyacrylamide. The first degradation is at 186.53–252.51°C with a weight loss of 0.721% due to absorbed and bonded water in polyacrylamide [43]. The second degradation temperature (T_d) is onset at 252.51–311.97°C with a weight loss of 8.556%. The degradation evolves ammonia from thermal imidization of polyacrylamide [44, 45] removing of unreacted monomer or absorbed solvent. The main weight loss of 19.6% onset at 390.15–487.93°C results from degradation of the polymer chain backbone [46].

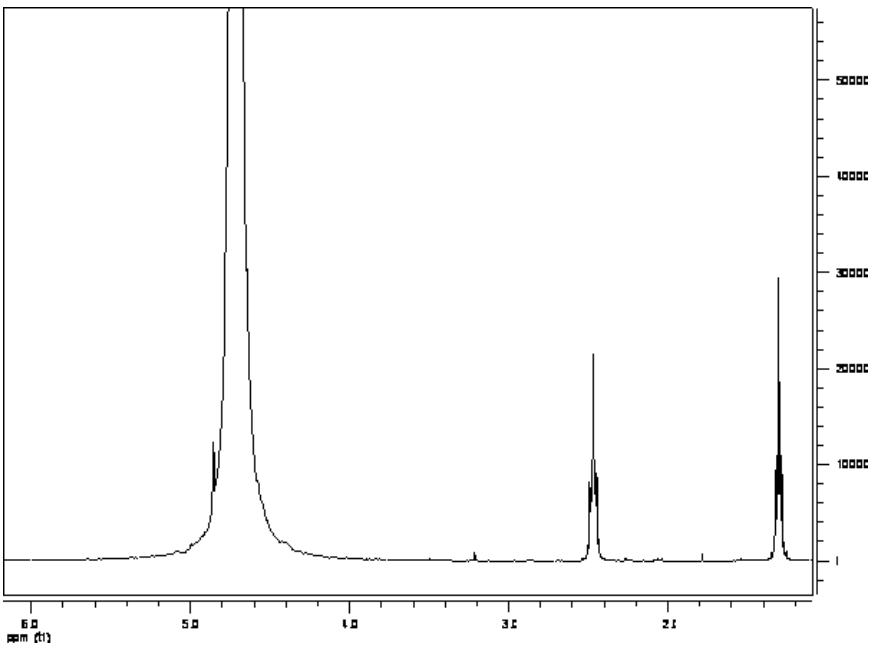

Figure 7. [1]H-NMR spectrum of anionic polyacrylamide (APAM) induced by maghnite-Na+ (5 wt%) under microwave irradiation.

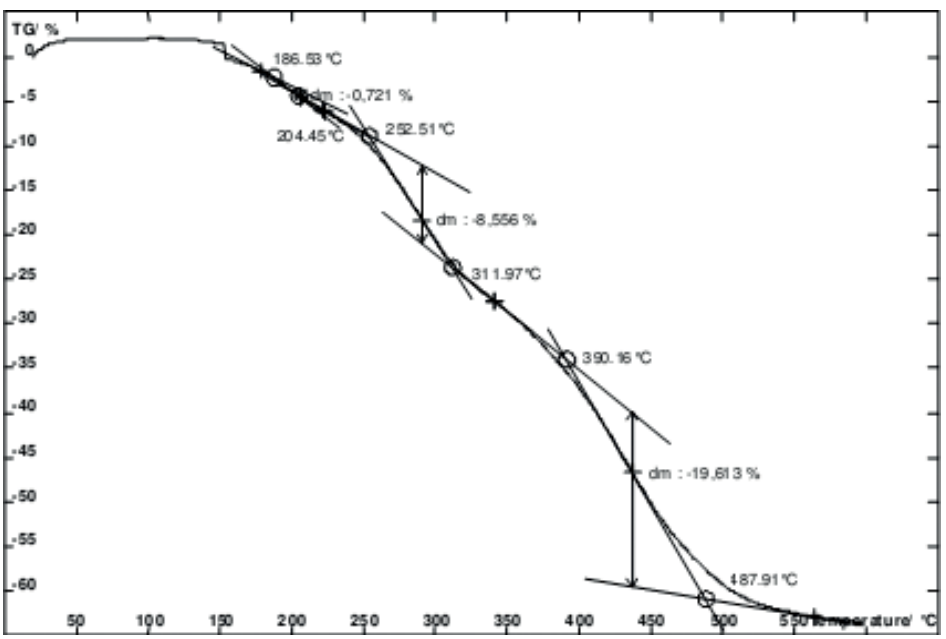

Figure 8. Thermogravimetric curve of the APAm, obtained after samples treated isothermally at 110°C for 20 min.

http://dx.doi.org/10.5772/intechopen.80033

6.2. Kinetics studies

Table 5 shows the effect of the amount of Magh-Na^+ on the polymerization yield under effect of microwave irradiation. Indeed, using various amounts of Magh-Na^+: 1.5, 2, 3, 4 and 5% yield increased with the amount of maghnite-Na^+, thus clearly showing the effect of Mag-Na^+ as a catalyst. This phenomenon is probably the result of an increase in the number of "initiating active sites" responsible of inducing polymerization, a number that is pro rata to the amount of catalyst used a reaction [47]. In the other hand the viscosimertic molecular weight are inversely proportional to the amount of Magh-Na^+. This finding is in good agreement with the proposal that MMT-Na^+ is present as the active initiator species since the number of those species by weight, the polymerization was carried under microwave irradiation in bulk at 160°C. The polymerization should be related to their surface area. Ayat et al. obtain similar results [48].

Effect of temperature on the polymerization of anionic polyacrylamide under effect of maghnite-Na^+ (5% by weight) for 5 min in microwave irradiation is shown in **Table 6**. Polymerization yield reach maximum value around 160–164°C. On the other hand, with the increase in the reaction temperature above 160°C, viscosity of the obtained polymer increase and decrease the molecular weight of the polymer progressively, suggesting the possible occurrence of thermal degradation [49, 50]. On the basis these results, subsequent polymerization were carried out at 160°C under effect of microwave irradiation.

The percentage moisture retains of maghnite-Na^+ and APAm/maghnite-Na^+ with increasing Am (acrylamide) and catalyst content are shown in **Figures 9–12**. It was observed that moisture retain gradually [51].

The decreases in moisture retain and water uptake can be attributed to the percentage of clay in the composite being limited, which reflects that the quantity of the polymer introduced in the layers reaches a limit and is enough to achieve maximum opening of the interlayer of clay and the formation of a cross-linked structure of a certain extent which prevents the insert on of water molecules [52, 53]. Finally, water resistance of these composites which as defined the decreases in moisture retain and water uptake values can be greatly improved [54, 55].

Time (min)	**1**	**2**	**3**	**4**	**5**
Catalyst (%)	1.5	2	3	4	5
Yield (%)	15.09	34.86	52.93	77.95	84.82

Table 5. Effect of amount of catalyst on polymerization yield of anionic polyacrylamide (APAm) under microwave irradiation.

Time (min)	**5**	**5**	**5**	**5**	**5**
Temperature (°C)	100	130	145	160	164
Yield (%)	19.34	39.06	59.81	79.91	84.94

Table 6. Effect of temperature on polymerization yield of anionic polyacrylamide under microwave irradiation.

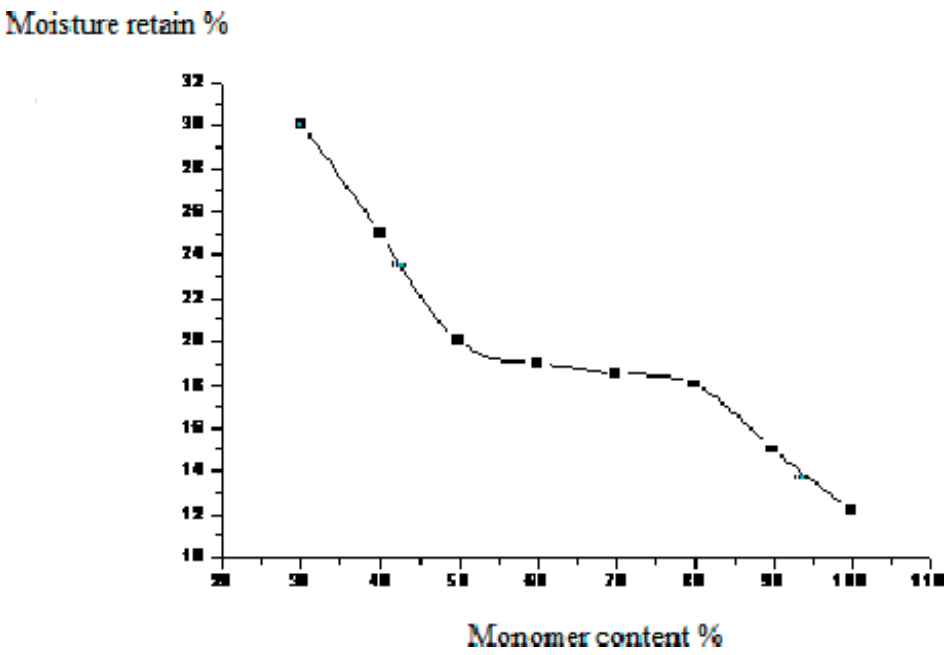

Figure 9. The percentage moisture retains values of acrylamide (Am) obtained including different percentages of (Am).

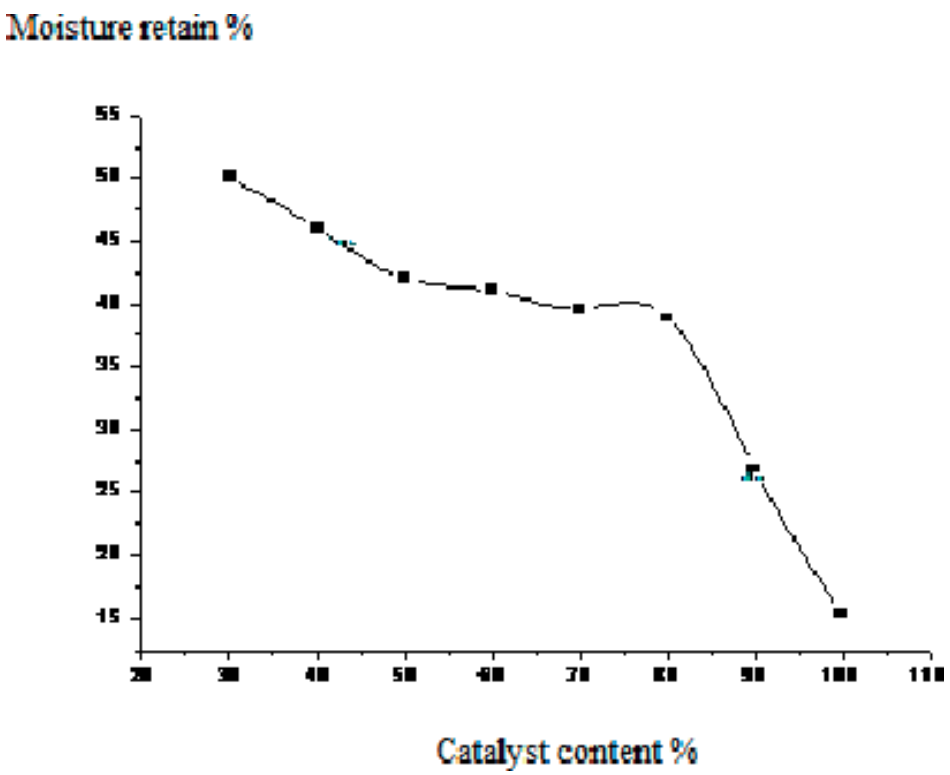

Figure 10. The percentage moisture retains values of maghnite-Na^+ obtained including different percentages of maghnite.

http://dx.doi.org/10.5772/intechopen.80033

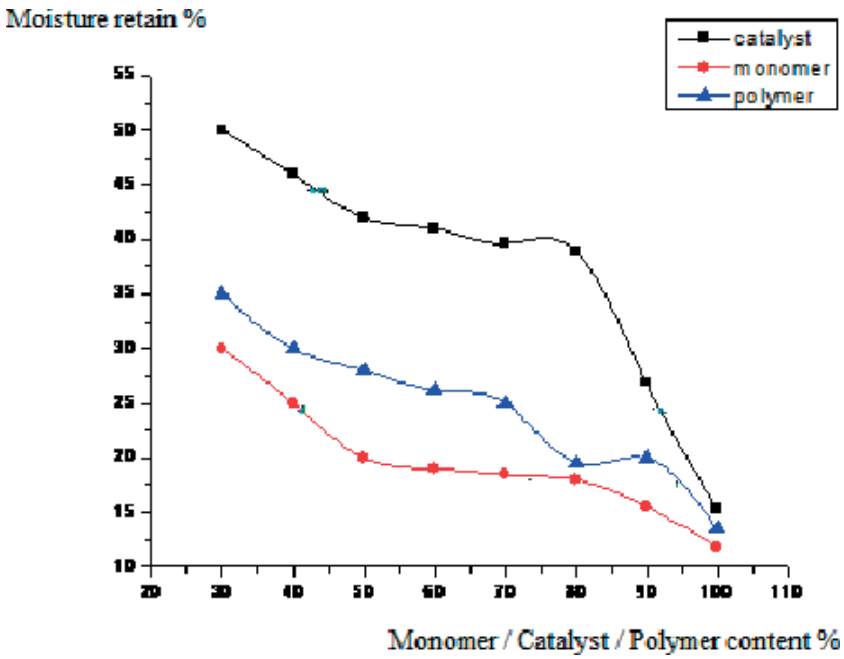

Figure 11. The percentage moisture retains values of maghnite-Na+, Am and APAm obtained including different percentages of Am, maghnite-Na+ and APAm.

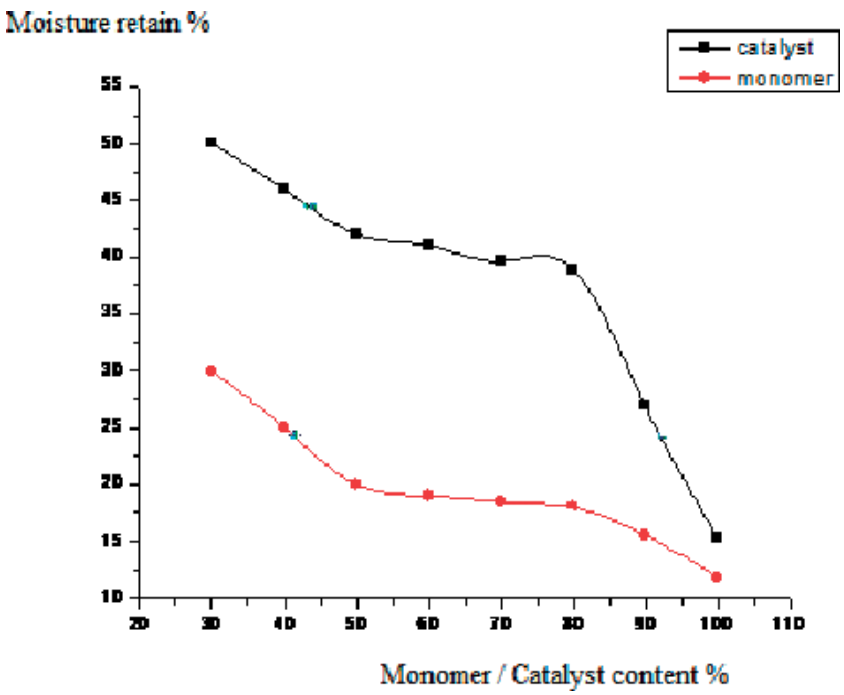

Figure 12. The percentage moisture retains values of maghnite-Na^+ and APAm/maghnite-Na^+ obtained including different percentages of Am.

6.3. Mechanical properties

To evaluate the effect of maghnite (Algerian MMT) catalyst in APAm, we prepared five samples with the same procedure. Tensile tests were conducted using a LLoyd LR/10KN Universal Machine at room temperature and crosshead speed of 50 mm min^{-1} for the determination of tensile modulus and yield strength, according to the standard ASTM D638.

Compared with PAm prepared by other catalyst such as Lewis acid and under conventional method, the Young's modulus and yield strength are greatly enhanced as shown in (**Table 7**). It shows that the mechanical properties depend on amount of catalyst.

The tensile test was carried out to evaluate the tensile properties of the various samples compositions in order to determine the influence of the addition of the clay on the tensile properties of the virgin matrix. Young modulus, tensile strength and elongation at break were evaluated as a function of the mass fraction of clay in all series of samples. The test pieces are maintained during the test by pneumatic jaws preventing any sliding of the test piece during the traction. The initial strain rate was set at 5 mm min^{-1}. From these results, it can be deduced that the incorporation of the clay into the APAm matrix, with different percentages, has significantly improved all of its tensile properties. Thus Young's modulus increased in compositions with the highest clay contents, (1–12 w%). The composition of clay (5 w%) in APAm has the highest tensile values. This is attributed to the interactions between the polymer chains and the nanometric layers of the clay with a decrease in the value of the Young's modulus. This composition is the most tensile resistant with a maximum stress of 57.55 MPa, the most flexible (E = 1.89 GPa) and the most ductile (ε_r = 54.03%). This result confirms the exfoliation of maghnite clay in polymer (APAm) which is in agreement with the literature [56].

6.4. Proposed mechanism

In general, the anionic polymerization like in other vinyl polymerization methods consists of three main reactions: (a) initiation, (b) propagation, and (c) termination, as described in **Figure 13**. However, termination is brought about intentionally using a suitable electrophile, which can be useful for end group modification [49]. The initiation reaction is generally fast and is not reflected in the overall rate of the polymerization [57]. The kinetics of the polymerization is predominantly controlled by the propagation step [58].

The interaction of propagating ion pairs with functional groups of the vinyl monomer or the polymer chain can affect the propagation rate and in some cases induces side reactions that can cease the polymerization [49]. In a side reaction-free anionic vinyl polymerization; the termination is a simple rapid reaction wherein anions are quenched through acidic hydrogen or another suitable electrophile [45]. Hence, it is important to match the reactivity of the initiator with the propagating species in order to have fast and homogeneous initiation [44]. For example, the reaction of sodium metal generates a radical anion in polar solvent, which can be used as initiator for the anionic polymerization [59]. The anionic polymerization of acrylamide in free solvent and under microwave irradiation was first studied using the maghnite-Na^+ as catalyst. The proposed anionic polymerization mechanism as shown in **Figure 13**. The high reactivity of the methylene group of double bond in acrylamide, involves

Sample	Catalyst (w%)	Young's modulus (GPa)	Deformation at break (%)	Maximum stress (MPa)	Yield strength (MPa)
Maghnite	—	1.23	54.36	43.26-	—
APAm (pure)	—	0.68	42.91	33.91	70.45
APAm-1/Magh	1	0.64	35.56	35.13	62.05
APAm-2/Magh	2	0.86	30.42	33.80	65.66
APAm-3/Magh	3	0.95	29.35	31.28	67.33
APAm-4/Magh	4	1.45	31.22	31.22	70.88
APAm-5/Magh	5	1.29	54.03	57.55	85.09
APAm-6/Magh	7	1.81	46.47	48.37	84.12
APAm-7/Magh	12	1.72	41.44	41.44	83.56

Table 7. Mechanical properties of APAm/maghnite samples.

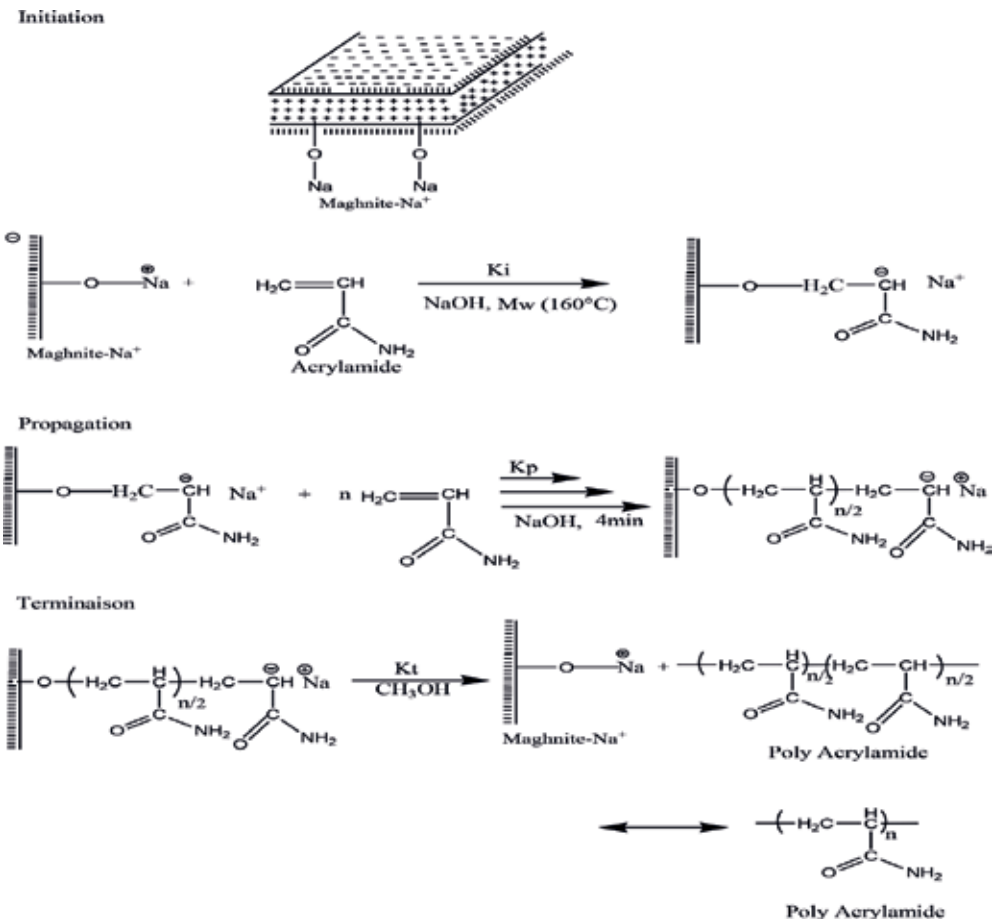

Figure 13. Proposed mechanism for obtained anionic polyacrylamide catalyzed by maghnite-Na^+.

the formation of a strong proton donor by the reaction of the maghnite-Na^+, followed by the protonation of the acrylamide molecule, whose ensuing carbenium ion rearranges to form a carbocation responsible for the propagation reaction [60] . This process is extremely rapid and exothermic. In order to obtain polymers with viable molecular weights of a few thousand, the polymerization temperature must be particularly low and around of −160°C [61], to reduce the relative kinetic contribution of the transfer reaction with respect to chain propagation. The driving forces for the reaction are the high reactivity of the l double bond of monomer and the high reactivity of catalyst [62, 63, 64, 65].

7. Conclusion

At the optimal conditions, anionic polyacrylamide material was successfully synthesized as an aqueous free solvent dispersion with acrylamide (Am) and maghnite-Na^+ (MMT-Na^+) in aqueous solution of sodium hydroxide NaOH under microwave irradiation. The influencing factors on the polymerization reaction were studied, and the optimal reaction conditions were obtained. The characterization of anionic polyacrylamide was measured by IR and HNMR spectroscopy. The results indicated that, the polymerization was successful under microwave irradiation. In our previous papers, we already reported about polymerization catalyzed by maghnite-Na^+ (Algerian MMT) this new nontoxic cationic catalyst exhibited higher efficiency via the polymerization of vinylic and hetero-cyclic monomers. The objectives of this work are the synthesis of anionic polyacrylamide of by the use of MMT-Na^+ as catalyst. The interesting aspect of this new non-toxic catalyst is the environmentally friendly nature of the reaction because it does not imply the disposal of solvents or metal catalysts.

Acknowledgements

All our gratitude to the anonymous referees for their careful reading of the manuscript and valuable comments which helped in shaping this paper to the present form. We thank all laboratory staff of polymer chemistry from the University of Oran1 (Algeria) for their kind cooperation.

Author details

Rahmouni Abdelkader* and Belbachir Mohammed

*Address all correspondence to: ramaek23@yahoo.fr

Laboratory of Polymer Chemistry, Department of Chemistry, Faculty of Sciences, Oran1, University Ahmed Benbella, Oran, Algeria

References

[1] Roberts WJ, Day AR. A study of the polymerization of alpha-pinene and beta-pinene with Friedel crafts type catalysts. Journal of the American Chemical Society. 1950;**72**(3):1226-1230

[2] Ruckel ER, Wojcik RT, Arlt HG. Cationic polymerization of alpha-pinene oxide and beta-pinene oxide by a unique oxonium ion-carbenium ion sequence. Abstracts of Papers of the American Chemical Society. 1977;**173**(MAR 20):49

[3] Barros MT, Petrova KT, Ramos AM. Potentially biodegradable polymers based on alpha- or beta-pinene and sugar derivatives or styrene, obtained under normal conditions and on microwave irradiation. European Journal of Organic Chemistry. 2007;**8**:1357-1363

[4] Klass DL. Biomass for Renewable Energy, Fuels, and Chemicals. San Diego: Academic Press; 1998

[5] Wool RP, Sun XS. Bio-Based Polymers and Composites. Oxford: Elsevier; 2005

[6] Keszler B, Kennedy JP. Advances in Polymer Science. 1992;**100**:1

[7] Lu J, Kamigaito M, Sawamoto M, Higashimura T, Deng Y-X. Macromolecules. 1997;**30**:22

[8] Guine RPF, Castro J. Polymerization of beta-pinene with ethylaluminum dichloride ($C_2H_5AlCl_2$). Journal of Applied Polymer Science. 2001;**82**(10):2558-2565

[9] Belbachir M, Yahiaoui A, Hachemaoui A. Cationic polymerization of 1,2-epoxypropane by an acid exchanged montmorillonite clay in the presence of ethylene glycol. International Journal of Molecular Sciences. 2003;**4**:572-585

[10] Rabiee A, Zeynali ME, Baharvand H. Synthesis of high molecular weight partially hydrolyzed polyacrylamide and investigation on its properties. Iranian Polymer Journal. 2005;**14**:603-608

[11] El-Zawawy WK, Ibrahim MM. Preparation and characterization of novel polymer hydrogel from industrial waste and copolymerization of poly(vinyl alcohol) and polyacrylamide. Journal of Applied Polymer Science. 2012;**124**:4362-4370

[12] Kabiri K, Omidian H, Zohuriaan-Mehr MJ, Doroudiani S. Superabsorbent hydrogel composites and nanocomposites. Polymer Composites. 2011;**32**:277-289

[13] Chen M, Wang LY, Han JT, Zhang JY, Li ZY, Qian DJ. Preparation and study of polyacrylamide-stabilized silver nanoparticles through a one-pot process. The Journal of Physical Chemistry B. 2006;**110**:11224-11231

[14] Dragan S, Mihai M, Ghimici L. Viscometric study of poly(sodium 2-acrylamido-2-methylpropanesulfonate) and two random copolymers. European Polymer Journal. 2003;**39**:1847-1854

[15] Rosa F, Bordado J, Casquilho M. Hydrosoluble copolymers of acrylamide-(2-acrylamido-2-methylpropanesulfonic acid). Synthesis and characterization by spectroscopy and viscometry. Journal of Applied Polymer Science. 2003;**87**:192-198

[16] Ferfera-Harrar H, Aiouaz N, Dairi N, Hadj-Hamou AS. Preparation of chitosan-g-poly(acrylamide)/montmorillonite superabsorbent polymer composites: Studies on swelling, thermal, and antibacterial properties. Journal of Applied Polymer Science. 2014;**131**:9747-9761

[17] Belbachir M, Yahiaoui A, Hachemaoui A. An acid exchanged montmorillonite clay-catalyzed synthesis of polyepichlorhydrin. International Journal of Molecular Sciences. 2003;**4**:548-561

[18] Belbachir M, Bensaoula A. Composition and method for catalysis using bentonites. US patent no. 7, 094-823 B2; 2006

[19] Yahiaoui A, Belmokhtar A, Sahli N, Belbachir M. Express Polymer Lett. 2007;**1**(7):443-449

[20] Shields SP, Richards VN, Buhro WE. Nucleation control of size and dispersity in aggregative nanoparticle growth a study of the coarsening kinetics of thiolate-capped gold nanocrystals. Chemistry of Materials. 2010;**22**:3212-3225

[21] Zhao Q, Sun J, Lin Y, Zhou Q. Superabsorbency, study of the properties of hydrolyzed polyacrylamide hydrogels with various pore structures and rapid pH-sensitivities. Reactive and Functional Polymers. 2010;**70**:602-609

[22] Singh V, Tewari A, Tripathi DN, Sanghi R. Microwave assisted synthesis of guar-g-polyacrylamide. Carbohydrate Polymers. 2004;**58**:1-6

[23] Rahmouni A, Harrane A, Belbachir M. Thermally stable forms of pure polyaniline catalyzed by an acid-exchanged montmorillonite clay called maghnite-H+ as an effective catalyst. International Journal of Polymer Science. 2012:7. DOI: 10.1155/2012/846710. Article ID846710

[24] Rahmouni A, Harrane A, Belbachir M. 1H-NMR spectra of conductive, anticorrosive and soluble polyaniline exchanged by an eco-catalyst layered (maghnite-H^+). World Journal of Chemistry. 2013;**8**(1):20-26

[25] Rahmouni A, Harrane A, Belbachir M. Structure and physicochemical properties of polyaniline synthesized in presence of maghnite clay catalyst layered (Algerian MMT). Research Journal of Material Sciences. 2013;**1**(3):1-6

[26] Megherbi A, Meghabar R, Belbachir M. Preparation and characterization of clay (maghnite-H)/poly(3,4-ethylenedioxythiophene) composites. Journal of Surface Engineered Materials and Advanced Technology. 2013;**3**:21-27

[27] Belbachir M, Bensaoula A. Composition and method for catalysis using bentonites. United States Patent Number: 6274527 B1; 2001

[28] Hachemaoui A, Belbachir M. Montmorillonite clay-catalysed synthesis of cyclic allylamines. Mendeleev Communications. 2005;**15**:124-125

[29] Toumi I, Benyoucef A, Yahiaoui A, Quijada C, Morallon E. Effect of the intercalated cation-exchanged on the properties of nanocomposites prepared by 2-aminobenzene sulfonic acid with aniline and montmorillonite. Journal of Alloys and Compounds. 2013;**551**:212-218

[30] Pramoda KP, Liu T, Liu Z, He C, Sue HJ. Thermal degradation behavior of polyamide 6/clay nanocomposites. Polymer Degradation and Stability. 2003;**81**(1):47-56

[31] Sudha JD, Sivakala S, Chandrakanth CK, Neethu KS, Rohini KN, Ramakrishnan. Percolated conductive polyaniline-clay nanocomposite in polyvinyl chloride through the combined approach porous template and self-assembly. Express Polymer Letters. 2014;**8**(2):107-115

[32] Kherroub DE, Belbachir M, Lamouri S. Nylon 6/clay nanocomposites prepared with Algerian modified clay (12-maghnite). Research on Chemical Intermediates. 2015;**41**:5217-5228

[33] Mohammed CB, Rachid M, Mohammed B. Acid-activated Algerian montmorillonite as heterogeneous catalyst for cationic polymerization of styrene. Asian Journal of Chemistry. 2016;**28**:1197-1204

[34] Belmokhtar A, Sahli N, Yahiaoui A, Belbachir M. Polycondensation of pyrrole and benzaldehyde catalysed by maghnite-H^+. Express Polymer Letters. 2007;**1**:443-449

[35] Kherroub DE, Belbachir M, Lamouri S. Cationic ring opening polymerization of ε-caprolactam by a montmorillonite clay catalyst. Bulletin of Chemical Reaction Engineering & Catalysis. 2014;**9**:74-80

[36] Ya-Qing Z, Xiang K, Xiao-Li Z, Zheng-Hong L. Particle kinetics and physical mechanism of microemulsion polymerization of octamethylcyclotetrasiloxane. Powder Technology. 2010;**201**:146-152

[37] Ouis N, Benharrats N, Belbachir M. Synthesis of polytetrahydrofurane catalyzed by kaolin of Tamazert. Comptes Rendus Chimie. 2004;**7**:955-962

[38] Njopwouo D, Roques G, Wandji R. A contribution to the study of the catalytic action of clays on the polymerization of styrene: II. Reaction mechanism. Clay Minerals. 1988;**23**:35-43

[39] Nicolay V, Tsarevsky S, Wojciech J. Atom transfer radical polymerization of functional monomers employing Cu-based catalysts at low concentration: Polymerization of glycidyl methacrylate. Journal of Polymer Science, Part A: Polymer Chemistry. 2011;**49**(4):918-925

[40] Wang W, Liu LY, Huang ZH. Study of photoinitiated dispersion polymerization of acrylamide by using graft copolymer of acrylic acid and nonylphenoxypoly (ethylene oxide) macromonomers as dispersant. Acta Polymerica Sinica. 2005;**3**:320-326

[41] Shainberg I, Warrington DN, Rengasamy P. Water quality and PAM interactions in reducing surface sealing. Soil Science. 1990;**149**:301-307

[42] Zolfaghari R, Katbab AA, Nabavizadeh J, Tabasi RY, Nejad MH. Preparation and characterization of nanocomposite hydrogels based on polyacrylamide for enhanced oil recovery applications. Journal of Applied Polymer Science. 2006;**100**(3):2096-2103

[43] Smets G, Hesbain AM. Hydrolysis of polyacrylamide and acrylic acid–acrylamide copolymers. Journal of Polymer Science. 1956;**40**:217-226

[44] Luo J, Bu R, Zhu H, Wang P, Liu Y. Property and application of comb-shape polyacrylamide. Acta Petrolei Sinica. 2004;**25**(2):65-68

[45] Feng YJ, Billon L, Grassl B, Bastiat G, Borisov O, Francois J. Hydrophobically associating polyacrylamides and their partially hydrolyzed derivatives prepared by post-modification. 2. Properties of non-hydrolyzed polymers in pure water and brine. Polymer. 2005;**46**(22):9283-9295

[46] Martin D, Ighigeanu DI, Mateescu EN, Craciun GD, Calinescu II, Iovu HM, et al. Combined microwave and accelerated electron beam irradiation facilities for applied physics and chemistry. IEEE Transactions on Industry Applications. 2004;**40**:41-52

[47] Caulfield MJ, Hao X, Qiao GG, Solomon DH. Degradation on polyacrylamides. Part II. Polyacrylamide gels. Polymer. 2003;**44**:3817-3826

[48] Ayat M, Belbachir M, Rahmouni A. Journal of Molecular Structure. 2017;**1139**:381-389

[49] Zhao YZ, Zhou JZ, Xu XH, Liu WB, Zhang JY, Fan MH, et al. Synthesis and characterization of a series of modified polyacrylamide. Colloid & Polymer Science. 2009;**287**(2):237-241

[50] Abdolbaghi S, Pourmahdian S, Saadat Y. Preparation of poly (acrylamide)/nanoclay organic-inorganic hybrid nanoparticles with average size of ~250 nm via inverse Pickering emulsion polymerization. Colloid and Polymer Science. 2014;**292**:1091-1097

[51] Aguilar J, Moscoso F, Rios O, Ceja I, Sánchez J, Bautista F, et al. Swelling behavior of poly(N-isopropylacrylamide) nanogels with narrow size distribution made by semicontinuous inverse heterophase polymerization. Journal of Macromolecular Science, Part A. 2014;**51**:412-419

[52] Reddy KR, Lee KP. Facile synthesis of conducting polymer metal hybrid nanocomposite by in situ chemical oxidative polymerization with negatively charged metal nanoparticles. Materials Letters. 2008;**62**:1815-1818

[53] Zhou C, Wu Q. A novel polyacrylamide nanocomposite hydrogel reinforced with natural chitosan nanofibers. Colloids and Surfaces B. 2011;**84**:155-162

[54] Capek I. On photoinduced polymerization of acrylamide. Designed Monomers and Polymers. 2014;**17**:356-363

[55] Mishra A, Yadav A, Pal S, Singh A. Biodegradable graft copolymers of fenugreek mucilage and polyacrylamide: A renewable reservoir to biomaterials. Carbohydrate Polymers. 2006;**65**:58-63

[56] Fortenberry DI, Pojman JA. Solvent-free synthesis of polyacrylamide by frontal polymerization. Journal of Polymer Science: Part A. 2000;**38**(7):1129-1135

[57] Mishra A, Rajani S, Agarwal M, Dubey RP. Psyllium-g-polyacrylamide: Synthesis and characterization. Polymer Bulletin. 2002;**48**:439-444

[58] Hatada K, Ute K, Tanaka K, Kitayama T, Okamoto Y. Mechanism of polymerization of MMA by grignard reagents and preparation of high isotactic PMMA with narrow molecular weight distribution. In: Hogen-Esch T, Smid J, editors. Recent Advances in Anionic Polymerization. New York: Elsevier; 1987. p. 195

[59] El-Sayed M, Sorour M, Abd-El-Moneem N, Talaat H, Shalaan H, El-Marsafy N. Synthesis and properties of natural polymers-grafted-acrylamide. World Applied Sciences Journal. 2011;**13**:360-368

[60] Capek I. Photopolymerization of acrylamide in the very low monomer concentration range. Designed Monomers and Polymers. 2016;**19**:290-296

[61] Truong ND, Galin JC, Francois J, Pham QT. Microstructure of acrylamide acrylic-acid copolymers. 1. As obtained by alkaline-hydrolysis. Polymer. 1986;**27**(3):459-466

[62] Cho MS, Yoon KJ, Song BK. Dispersion polymerization of crylamide in aqueous solution of ammonium sulfate: Synthesis and characterization. Journal of Applied Polymer Science. 2002;**83**:1397-1405

[63] Gemeinhart RA, Park H, Park K. Pore structure of superporous hydrogels. Polymers for Advanced Technologies. 2000;**11**:617-625

[64] Zhou Y, Li F, Liu J, Yun Z, Gui X. Pt-H_2SO_4/Zr-montmorillonite: An efficient catalyst for the polymerization of octamethylcy-clotetrasiloxane, polymethylhydrosiloxane and hexamethyldisiloxane to low-hydro silicone oil. Chinese Journal of Chemical Engineering. 2017; pp. 1771-1776

[65] Belmokhtar A, Benyoucef A, Zehhaf A, Yahiaoui A, Quijada C, Morallon E. Studies on the conducting nanocomposite prepared by polymerization of 2-aminobenzoic acid with aniline from aqueous solutions in montmorillonite. Synthetic Metals. 2012;**162**(21): 1864-1870

Chapter 8

Biocomposites from Colombian Sugarcane Bagasse with Polypropylene: Mechanical, Thermal and Viscoelastic Properties

Miguel Ángel Hidalgo-Salazar,
Fernando Luna-Vera and Juan Pablo Correa-Aguirre

Additional information is available at the end of the chapter

http://dx.doi.org/10.5772/intechopen.80753

Abstract

Biocomposites are materials formed by mixing a polymer matrix and a filler or reinforcement, with the characteristic that at least one should be of biological origin. For this study, biocomposites were obtained from natural fibers of cane bagasse and polypropylene, using bagasse from postindustrial sources, originating from the production of sugarcane from the Valle-Cauca region in Colombia. In addition, cane bagasse fibers were treated chemically, with the purpose of improving the interfacial relationship. Polypropylene homopolymer was used as a polymeric matrix, which was mixed in a twin screw extruder, obtaining different materials as biocomposites. Finally, it was possible to obtain a suitable biocomposite for application in injection molding processes and studying its mechanical, viscoelastic, and thermal behaviors, through DSC, TGA, DMA, and SEM techniques.

Keywords: biocomposites, sugarcane bagasse, mechanical properties, thermal properties, DMA

1. Introduction

Since several decades ago, biocomposites have emerged as an option aimed to solve several issues within the composite materials science. In most of published cases in the literature, the use of natural fibers in combination with polymers is carried out to achieve some degree of reinforcement from the fibers to the polymer. Many studies report the use of natural fibers such as flax, hemp, jute, sisal, coconut fiber, banana, and fique, among many others [1], using

an extensive variety of polymer matrices like polyethylene [2, 3], polypropylene [4], polystyrene [5], polyester resins [6], and natural rubber [7]. Clear effects have been seen in the improvement of mechanical performance. For example, usually Young's modulus and tensile and flexural strength increase when natural fibers are compounded in percentages from 10 to 40%, which make the composites stiffer than its matrix counterpart [8]. Also, improvement in impact strength has been observed [9]. These findings give to the natural fibers a real opportunity to replace to some extent the use of fiberglass, aramid, and other synthetic fibers usually used for polymer reinforcement since, on top of their reinforcement ability, natural fibers are also cheap and have a much lower density than fiberglass, as previously stated in literatures [10–12]. However, the interest in utilization of natural fibers in biocomposites goes beyond their advantages for formulating new and mechanically improved materials. Interest is also driven by a global concern about the impact of plastics in the environment and a growing consciousness of the need for establishing a circular economy where residues like biomass and lignocellulosic can be valued and used as new raw material for industrial processes [13, 14]. In that regard it makes sense to use the agroforestry residues of extensive crops in a way that results in a neutral CO_2 process, like the fabrication of composites, instead of using them for energy production through combustion. An example of the potential of lignocellulosic materials is the region of Valle del Cauca in the South West of Colombia, which has a large influence of the sugarcane industry. It produces 80% of all Colombian sugar, and also it counts for 50% of all local agricultural production. This industry produces a lot of agroforestry residues, approximately 6 million tons of sugarcane bagasse a year [15]. The availability and low cost of this residue are thought as competitive advantages for the development of sustainable biocomposites in this region. That is the main reason behind of our resent research: the valorization of sugarcane residues by their use in natural fiber reinforced polymer composites (NFPC). In regard to the use of sugarcane bagasse, some studies have reported its use as reinforcement for polypropylene, polyester, recycled PET, PVC, HIPS, and HDPE and as agents and/or compatibilizing treatments such as aluminates and mercerization (NaOH treatment) and the use of ethylene and methyl acrylate as copolymers and benzyl chloride [16–19]. However, to the best of our knowledge, there have been no reports of the use of silanes as compatibilizing agents in sugarcane bagasse microfibers, in order to improve their adhesion to polymer matrices. In this chapter, polypropylene bagasse (PP bagasse) biocomposites prepared through extrusion, injection, and thermocompression molding will be evaluated. The morphology as well as the mechanical, thermal, and thermomechanical properties of the biocomposites will be investigated with the aim to understand the effect of the chemical treatments of the bagasse fibers on the polypropylene (PP) matrix properties.

2. Materials and methods

2.1. Materials

Sugarcane bagasse was obtained from a local sugar mill and kindly provided by Sucromiles S.A. Hexadecyltrimethoxysilane and sodium hydroxide were analytical-grade reagents from Aldrich (Wisconsin, USA). Absolute ethanol was a product from Merck (PA, USA). Polypropylene homopolymer 01H41 was obtained from Essentia (Cartagena, Colombia).

2.2. Preparation and characterization of sugarcane bagasse microfibers

Sugarcane as received was cleaned with distilled water in order to take off soil and residues from the lignocellulosic material. Clean bagasse was later dried at 60°C for 6 h until constant weight. Around 500 g of bagasse was then grounded using a Kinematica™ Polymix™ PX-MFC 90 D Lab mill drive and a sieve size of 200 μm. The sample was divided in three groups: one used as it was obtained after milling with no further treatment. A second group was treated with an aqueous solution of 8% NaOH using a 1:1 bagasse/solution ratio during 2 h, in order to remove lignin from the bagasse's surface. A third group of fibers were silanized after lignin removal. For silanization, a solution of 2×10^{-3} M of octadecyltrimethoxysilane in an 8:2 ethanol/water ratio as solvent was prepared. The pH of solution was kept at 3 using acetic acid. A time of 10 minutes was allowed for hydrolysis after addition of silane and before the solution was sprayed over bagasse fibers using a plastic spray bottle. Wet fibers were allowed to dry at 90°C for 24 h in a forced air oven. After drying, fibers were kept in plastic bags until used in the composition process with polypropylene.

Each group of fibers was characterized by thermal gravimetric analysis (TGA) using a nonreactive atmosphere (N2 at 50 mL/min) from 25 to 650°C at a heating rate of 10°C/min using a TGA/DSC 2 STAR system, from Mettler Toledo. Surface structure of fibers was characterized by scanning electron microscopy (SEM), and chemical maps are also obtained by electron dispersed spectroscopy (EDS) using an ultra-high-resolution analytical FE-SEM SU-70 from Hitachi. All samples were sputtered with gold before analysis. Silicon content on fibers was quantified by flame atomic absorption spectrometry (FAAS). Around 0.5 g of fibers was calcinated at 550°C for 4 h in porcelain crucibles. After calcination each sample was treated with 2 mL of HF (48–50%) and 98 mL of H_2SO_4 0.08 M. Samples were kept for 24 h in polypropylene containers for 24 h and then filtered. Quantification using Analist 800 from Perkin Elmer was performed using a nitrous oxide/acetylene flame.

2.3. Preparation of the biocomposites

Biocomposites were compounded in a counter-rotating twin screw extruder Thermo Scientific HAAKE™ Polylab. In all cases fibers were physically premixed with polypropylene pellets in a plastic bag using 20% of fiber in weight. About 500 g of fiber-polypropylene mix was introduced in the extruder at 70 rpm. A temperature gradient from 140 to 170°C from the feeder to the melting zone was used. The outcoming cord of composite from the extruder was pelletized using a rotating cutter which produced pellets of about 5 mm long.

After the pelletization process, the PP and PP-bagasse biocomposite samples were dried in an oven at 85°C followed by injection molding process at 180°C. A BOY XS (BOY Machines, Inc., USA) microinjection molding machine was used to prepare samples (3*12.7*60 mm) for flexural and impact tests. An injection pressure of 68 bar and a back pressure of 18 bar were used.

Also, sheets of the different samples were obtained using a hot-plate press and a forced water circulation cooling system (LabPro 400, Fontijne Presses). To shape the specimens, stainless steel molds were used. The molding was conducted at a temperature of 185°C, with a pressure of 50 kN and a 15 minute cycle. Finally, the sheets were demolded and adjusted to the required dimensions for DMA tests (1.7*12.7*60 mm) using a computer numerical control router. **Figure 1** shows the injected specimens of PP and a PP-bagasse biocomposite.

Figure 1. Injected specimens of PP and a PP-bagasse biocomposite.

2.4. Characterization of the biocomposites

2.4.1. Flexural properties

Three-point bending flexural tests were performed with an INSTRON universal testing machine model 3366 according to the ASTM D 790–17. The tests were carried out on bars of rectangular cross section at 23°C and at a rate of crosshead motion in 1.3 mm/min. This rate was determined based on the dimensions of the specimen. Also, the distance between the supports was 50 mm, and the tests were conducted up to 5% strain. All the results were taken as the average value of five samples.

2.4.2. Impact properties

The impact strength of PP and biocomposites were determined with an Izod Tinius Olsen impact pendulum equipped with a 4.53 N pendulum. Prior to the test, the materials were subjected to conditioning for 48 h at 50% relative humidity and a temperature of 25°C. The specimens were made following the standard ASTM D256, and the starting angle of the test was 55.80°. All the results were taken as the average value of five samples.

2.4.3. Thermal characterization

Differential scanning calorimeter (DSC) and TGA test of the neat PP and biocomposites were carried out using a TGA/DSC 2 STAR system, from Mettler Toledo. DSC tests were carried out under nitrogen atmosphere (N_2 at 50 mL/min) from 20 to 200°C at a scanning rate of 10°C/min, with a sample of 10 mg in aluminum pans. Melting temperatures (Tm) were determined from the first heating scans. TGA was carried out on 10 mg samples using a TA Q500 thermogravimeter at 10°C/min from 23 to 600°C under nitrogen flow. The thermal degradation temperatures considered were the onset of inflection (T_0) and the temperature of maximum weight loss rate (T_{max}).

2.4.4. Dynamic mechanical analysis

Polymers and composites have a different response to mechanical loads in comparison with other materials. They can be studied as materials that in some cases behave as elastic solids

and, in others, as viscous fluids. As such, its mechanical properties also depend on time, stress, and temperature. The present study of the viscoelastic performance was carried out in a DMA RSA-G2 with ACS-3 Air Chiller System. In order to identify the viscoelastic behavior of biocomposites, the following test modes were used:

2.4.4.1. Strain sweep tests

To begin the study of the viscoelastic response of biocomposites, the linear viscoelastic region for the PP matrix was identified. To find this region, strain sweeps were carried out at a defined temperature. The geometry used to perform these tests was three-point bending. A strain sweep test takes successive measurements with an increase in the strain. For these experiments, the RSA-G2 was programmed with a strain between 0.001 and 1%; the frequency was constant at 1 Hz. Measurements were made at 0, 30, and 60°C.

2.4.4.2. Temperature ramp tests

After finding the linear viscoelastic zone, temperature ramp tests were performed to observe the behavior of the PP matrix at different temperatures. These tests were performed between −60°C and 170°C, at 1 Hz, 3°C/min, and 0.01% of strain.

2.4.5. Morphology

Scanning electronic microscopy (SEM) of biocomposites was carried out on the cryogenic fracture surfaces of the specimens using a Quanta FEG 250 microscope operating at a voltage of 10 kV.

The samples were previously sputter-coated with gold to increase their electric conductivity. The cross-sectional diameters of the dispersed phase were measured using ImageJ 1.8v (Wayne Rasband, National institutes of health, USA). Determinations were performed in different areas of the SEM images.

2.4.6. Statistical analysis

Flexural and impact properties of the materials were subjected to analysis of variance (ANOVA), and the Tukey's test was applied at the 0.05 level of significance. All statistical analyses were performed using Minitab Statistical Software Release 12 (Pennsylvania, USA).

3. Results and discussion

3.1. Preparation of bagasse microfibers for biocomposite fabrication

In order to produce and tune a lignocellulosic material to improve the mechanical performance of natural fiber reinforced polymer composites (NFPC), it is very important to conceptualize adhesion as one of the most important factors to achieve such challenge [20, 21]. Adhesion on the polymer-fiber interface is said to follow one of the four common mechanisms: mechanical interlocking, electrostatic interactions, molecular entanglement, or chemical bonding [22]. Many commercial polymer-coupling additives like maleic and acrylate grafted thermoplastics work as adhesion enhancers in polyolefins by generating chemical bonds with the free

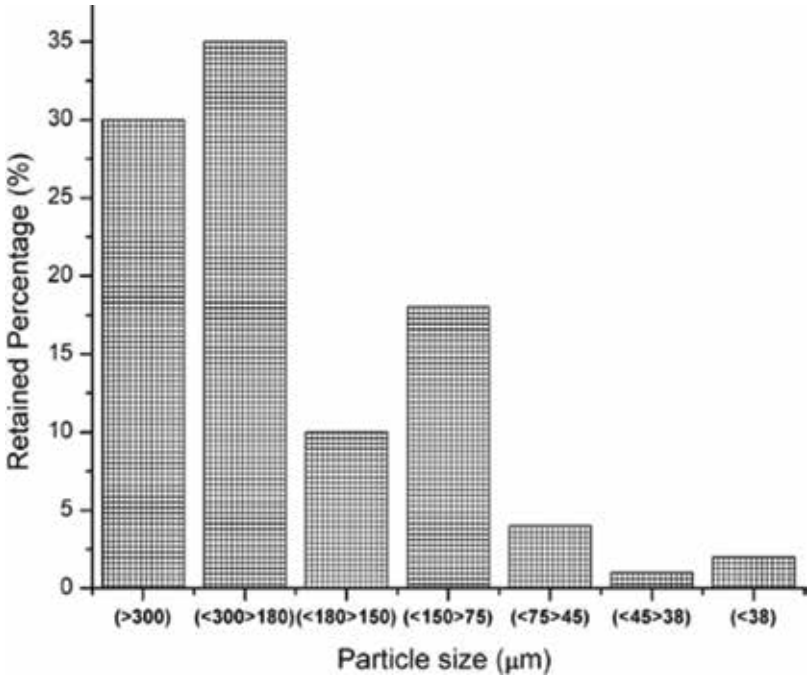

Figure 2. Granulometry of milled sugarcane fibers after lignin removal and silanization with hexadecyl triethoxysilane.

alcohol functionality on the fiber's cellulose [23]. In those aforementioned cases, the adhesion increases by conditioning the polymer to the fiber's surface. Instead, when silanes are used to increase adhesion, in the fiber's surface which is conditioned to interact with the olefin polymer matrix by promoting electrostatic interactions or chain molecular entanglement [24, 25].

When nonpolar silanes, like dodecyl, hexadecyl, or octadecyl triethoxysilanes, are used for fiber modification, there is a lowering effect of the fiber surface energy which increases compatibility with the matrix by matching the polarities [26]. A practical and quick way of estimating the surface energy of surfaces is by measuring the contact angle of the surface. However, in many NFPC applications, the size of the fibers used is in the range of micrometers, as shown in the granulometry in **Figure 2**, for the case of sugarcane bagasse fibers.

Measuring contact angle on rough surfaces, such as those formed for a bed of microsized fibers, can be challenging since the observed angle is the manifestation not just of the molecular interactions at the solid/liquid interphase but also of the microstructure of the surface (**Figure 3**).

This effect is counted by the model of Wenzel which predicts that if a molecularly hydrophobic surface is rough, the appearance is that of an even more hydrophobic surface [27, 28]. An interesting evidence of this phenomenon in particulate fibers is shown in **Figure 4**, where the contact angle of several groups of sugarcane bagasse fibers treated with solutions of variable silane concentrations appears almost invariant (between 122° and 129°), even though the absorbed amount of silane changes nearly in one order of magnitude (5.5×10^{-5} to 1.04×10^{-4} mol of silane per gram of fiber).

http://dx.doi.org/10.5772/intechopen.80753

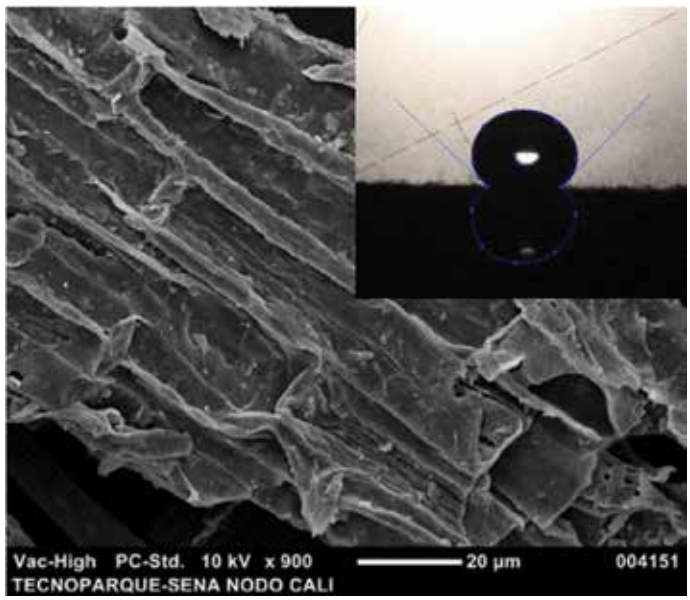

Figure 3. SEM photograph of a silanized sugarcane fiber. Inset shows the rough surface of a bed of fibers used to measure contact angle of the fibers.

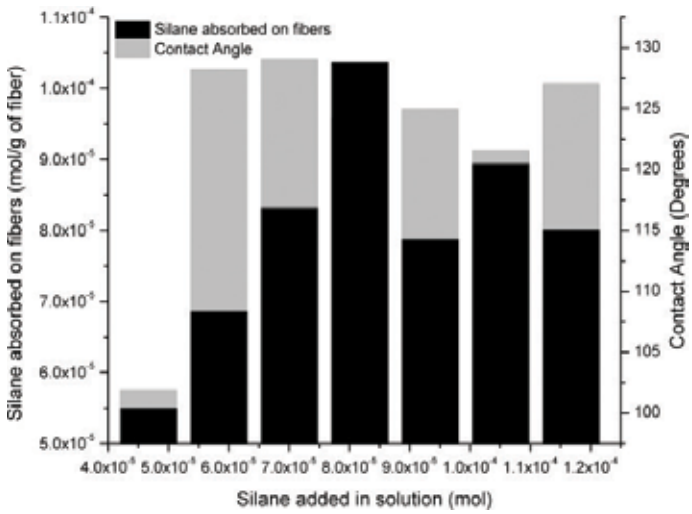

Figure 4. Effect of silane absorbed on microsized sugarcane bagasse fibers and their contact angle.

Another critical factor to achieve a good reinforcing material made of small natural fibers is the generation of anchoring points on the rough surface in order to produce enough silanization. Natural fibers in contrast with fiberglass, for example, do not have a well-defined geometry and instead lack of the advantage of having a highly energetic surface prone to react during silanization. Fiberglass has a surface populated with free hydroxyl groups from Si-OH functionality, but

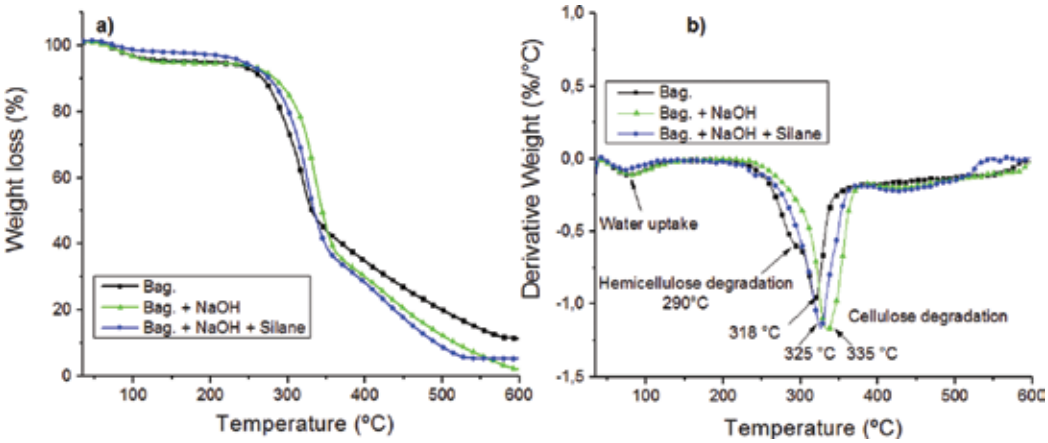

Figure 5. (a) TG and (b) DTG curves of bagasse fibers at heating rates of 10°C/min.

natural fibers are usually covered by a nonreactive lignin layer. That is why for natural fibers, the surface area that will react with silanes is determined by a good process of lignin removal, using alkaline or oxidative solutions, which will expose cellulose at the natural fiber's surface [29, 30].

The performance of the delignification treatment can be estimated from thermal gravimetric analysis (TGA) of fibers. **Figure 5** shows the TGA of sugarcane bagasse fibers before and after delignification with alkaline treatment and after silanization.

When a good delignification is carried out, fibers gain some thermal stability. As shown in **Figure 5**, the T_0 for sugarcane bagasse goes from 262 to 282°C when lignin has been removed. Also, as noted in the DTG, the typical signal of hemicellulose around 290°C disappears [31]. Furthermore, after most of lignin goes away, it is possible to observe a cleaner DTG signal with no shoulders that make evident the presence of residual compounds in the fibers. With only cellulose, the maximum degradation (T_{max}) in DTG occurs around 325°C. Silane presence also increases T_{max} to 335°C, mostly due to the formation of refractory siloxane network after silanization. Additionally, as observed in the TGA results, when surface modification by silanization with hydrophobic moieties has occurred, there is a clear decrease of water evaporation after 60°C, since fibers absorb less water when silanized. Changes in water uptake can go from 5 to 1%. This result indicates that silanization process reduces water absorption of the fibers and may give resistance against fungal decay [32].

Another factor that plays a role in the reinforcing ability of fibers is the distribution of silane on their surface. Few works have detailed how silane gets distributed in the rough surface of natural fibers. Using chemical maps from scanning electron microscopy coupled with energy dispersive X-ray spectroscopy (SEM-EDS), it is possible to survey the surface and locate silicon at specific locations on the fiber [33]. **Figure 6** shows the chemical maps for oxygen and silicon, as an example of chemical mapping of silanized fibers.

From SEM–EDX spectra, the concentration of surface atoms can be estimated using the intensity of signals at the specific energies of each atom. In this case, sugarcane bagasse fibers modified with hexadecyltrimethoxysilane were interrogated for the content of oxygen, silicon, and carbon before and after silanization. **Figure 7** reviews the results. Spectra revealed

http://dx.doi.org/10.5772/intechopen.80753

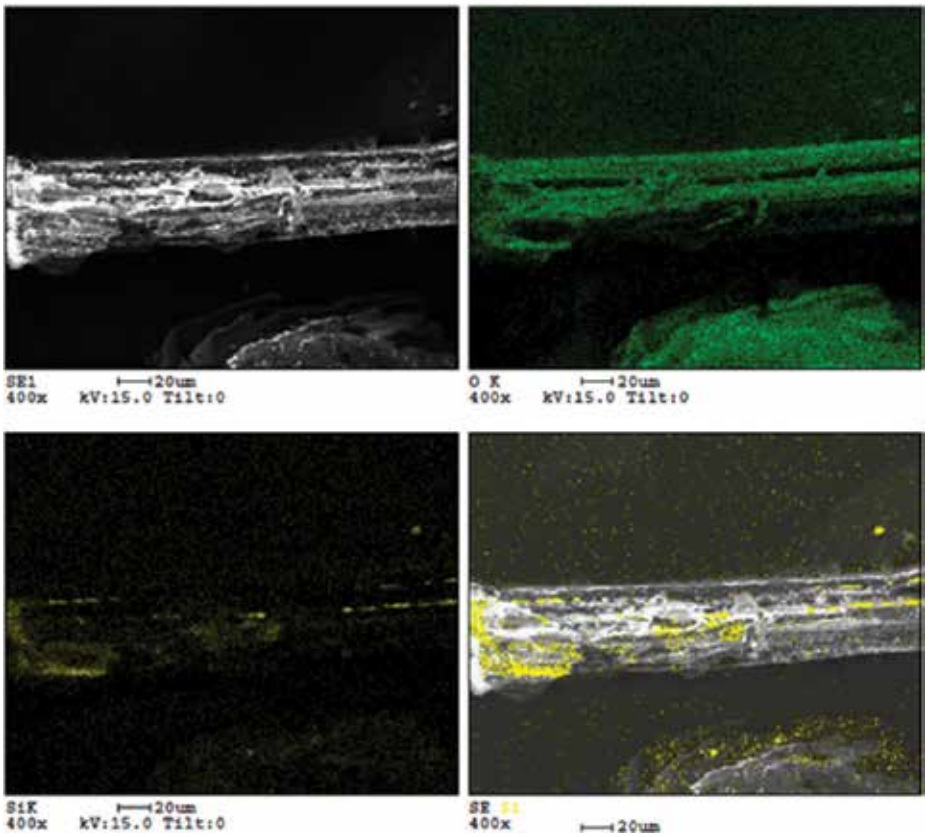

Figure 6. SEM–EDX chemical maps of sugarcane bagasse fiber treated with hexadecyltrimethoxysilane after delignification with NaOH 8%.

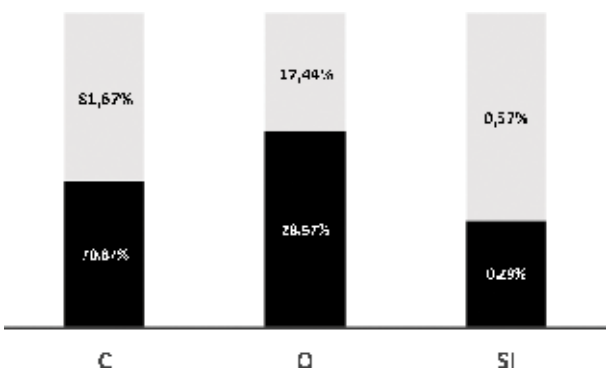

Figure 7. Percentage of total atomic content of carbon, oxygen, and silicon at fiber surface (black) and after (gray) silanization, measured by SEM–EDX.

that atomic oxygen content changed from 28.57 to 17.44%, carbon from 70.86 to 81.67%, and silicon from 0.29 to 0.57% before and after silanization, respectively. The variations in the atomic content are in agreement with the process performed. For example, the increment in

carbon content after silanization is due to the additional carbons brought to the surface by the long chains (C16) of hexadecyltrimethoxysilane. For oxygen instead, the surface atomic concentration becomes lowered since a not-significant amount of oxygen is added by silanes. Silicon, as expected, almost doubles his surface concentration.

In general, thermal, morphological, and chemical characterization of fibers is necessary when lignocellulosic materials are prepared as reinforcing fillers. The knowledge of important factors like the degree of lignin removal, distribution of silane, and hydrophobic character of fibers are very important to ensure that the material will behave successfully during compounding with polymeric matrices and then to obtain suitable mechanical properties of biocomposites.

3.2. Biocomposite characterization

3.2.1. Mechanical properties

The influence of bagasse fiber addition on the PP flexural and impact properties was evaluated. **Table 1** presents the values of the flexural modulus, flexural strength, and impact strength of the materials. Biocomposites showed different mechanical properties, indicating that the treatments affect the fiber-matrix interaction.

The results show that bagasse fiber incorporation induces a significant improvement of flexural properties of PP. For PP-bagasse and PP-Bag+NaOH biocomposite flexural modulus (FM) increased 60 and 42%, respectively. On the same way, flexural strength (FS) reached improvements of 20 and 8% compared to neat PP. For PP-Bag+NaOH+Silane, FM was enhanced 16%, respectively, in comparison with PP. However, the FS value was not significantly different ($p \geq 0.05$). Similar results were reported by Cerqueira et al. [34] when they studied the morphology and mechanical properties of PP-bagasse biocomposites. The authors reported that biocomposites present higher FM and FS values in comparison with neat PP and suggested a good interaction under the compressive stresses developed in part of the transverse section of the biocomposite specimens during bending.

On the other hand, the impact tests did not show significant differences between the PP matrix and the biocomposites PP bagasse and PP-Bag+NaOH. However, for PP-Bag+NaOH+Silane an

Sample	Impact and flexural properties*		
	Flexural properties		Impact properties
	Modulus (MPa)	Strength (MPa)	Impact strength (kJ/m^2)
PP	1296 ± 70^a	40.0 ± 0.7^a	4.4 ± 0.5^a
PP-Bag	2069 ± 30^b	48.0 ± 1.1^b	4.2 ± 0.2^a
PP-Bag+NaOH	1847 ± 114^c	43.3 ± 0.5^c	5.1 ± 0.5^a
PP-Bag+NaOH+Silane	1505 ± 94^d	38.6 ± 1.9^a	6.2 ± 0.1^b

Different letters (a–d) in the same column indicate significant differences ($p < 0.05$).
*Mean of five replications ± standard deviation.

Table 1. Flexural and impact properties of PP and PP-bagasse biocomposites.

increase of 40% was observed. This result shows that silanization increases the capacity of PP to absorb energy. This phenomenon can be explained by a possible energy absorption promoted by fracture mechanisms, which involve detachment, slippage, and fragmentation of the fiber. These mechanisms do not occur in neat PP and PP biocomposites without silanization.

3.2.2. Dynamic mechanical analysis

3.2.2.1. Strain sweep tests

Figure 8 shows the results of the strain sweep tests of the PP matrix. Images of the PP specimen are included at a strain of 0.01% (linear region) and 0.6% which corresponds to the nonlinear zone. In this zone it is observed that the specimen has been highly deformed. From these results a strain of 0.01% was used for subsequent temperature ramp tests.

3.2.2.2. Temperature ramp tests

Figure 9 shows the thermograms obtained in the DMA for the PP matrix and its biocomposites. In these graphs the values of the storage modulus (E′), loss modulus (E″), and tan delta are shown. Neat PP tan delta plot shows two relaxations located near 6°C (β relaxation or Tg) and 60°C (α relaxation) [35]. It is also observed that the values of E′ are temperature dependent. At 25°C the value of E′ is 2708 MPa, while at 75°C, this value is 1199 MPa, which represents a decrease of 55%.

In the tan delta plot of the biocomposite PP-Bag (**Figure 10**), a Tg of 5.3°C is observed, while the α relaxation increased 17.5°C compared to the neat PP. Also, E′values at 25°C is 2454 MPa,

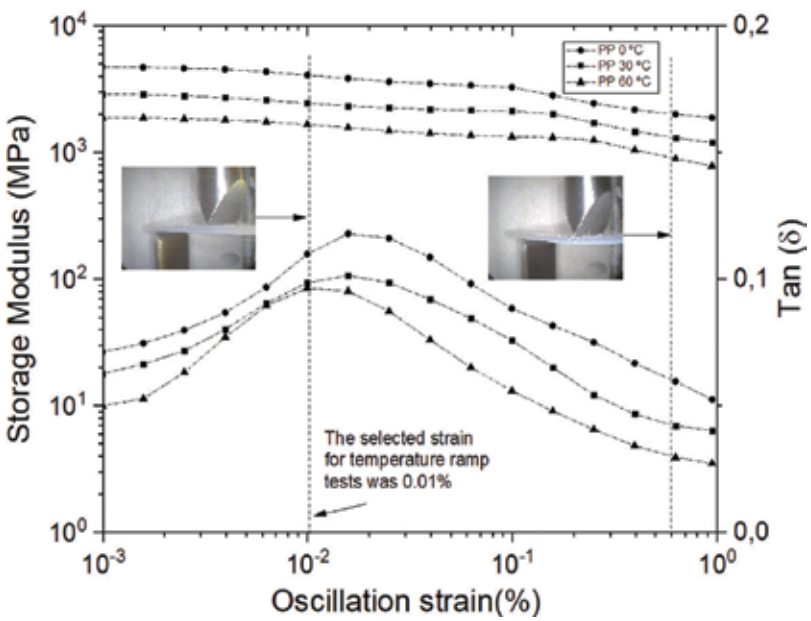

Figure 8. Strain sweep test curves for neat PP at 0, 30, and 60°C.

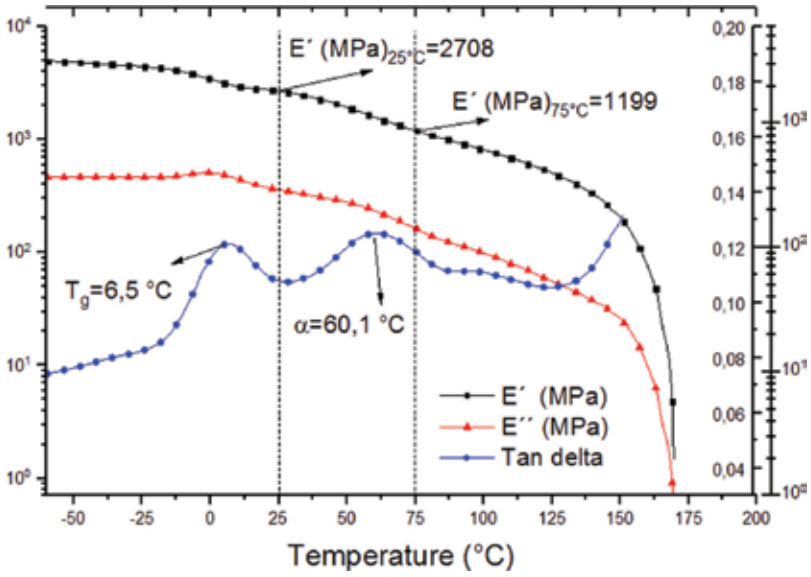

Figure 9. Dynamic mechanical analysis (DMA) curves of neat PP.

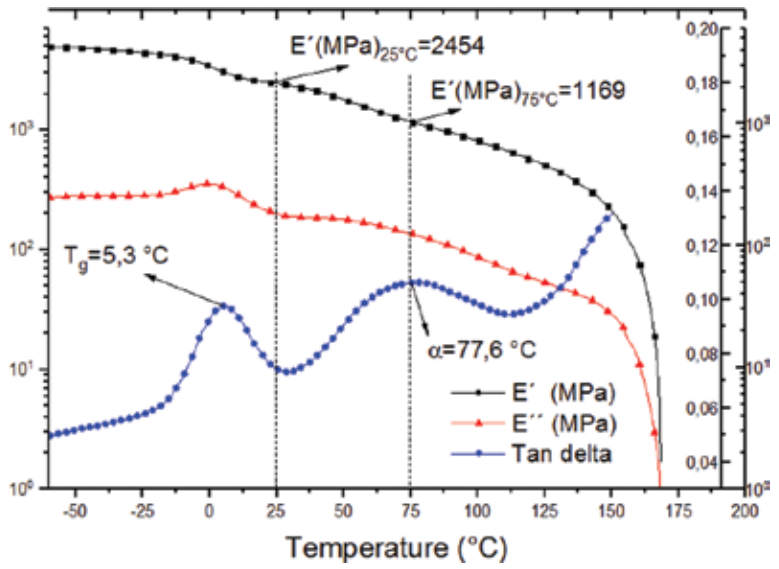

Figure 10. Dynamic mechanical analysis (DMA) curves of PP-Bag biocomposite.

while at 75°C, this value is 1169 MPa. E′values′ decrease in this temperature range was 52%. This result shows that the addition of bagasse fiber improves the stability of the storage module of the PP matrix with the temperature. The increase in the value of α relaxation and the stability of E′ with the temperature was also observed in biocomposites PP-Bag + NaOH and PP-Bag + NaOH+Silanes (**Figures 11** and **12**).

http://dx.doi.org/10.5772/intechopen.80753

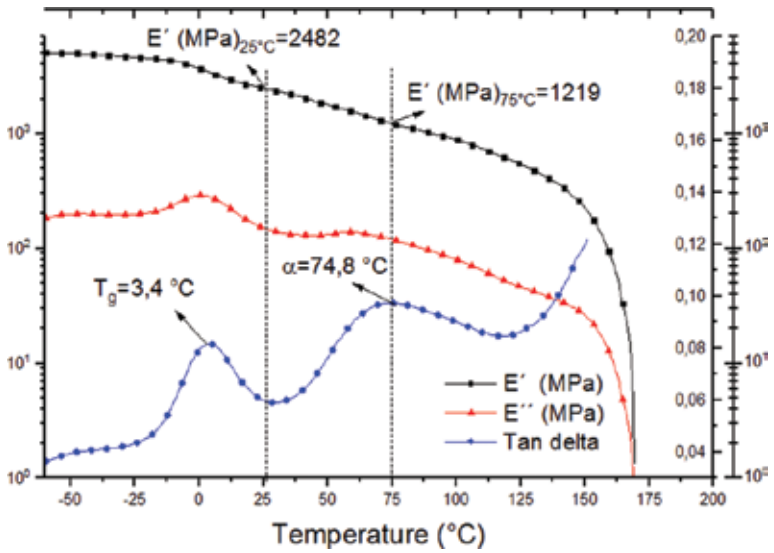

Figure 11. Dynamic mechanical analysis (DMA) curves of PP-Bag + NaOH biocomposite.

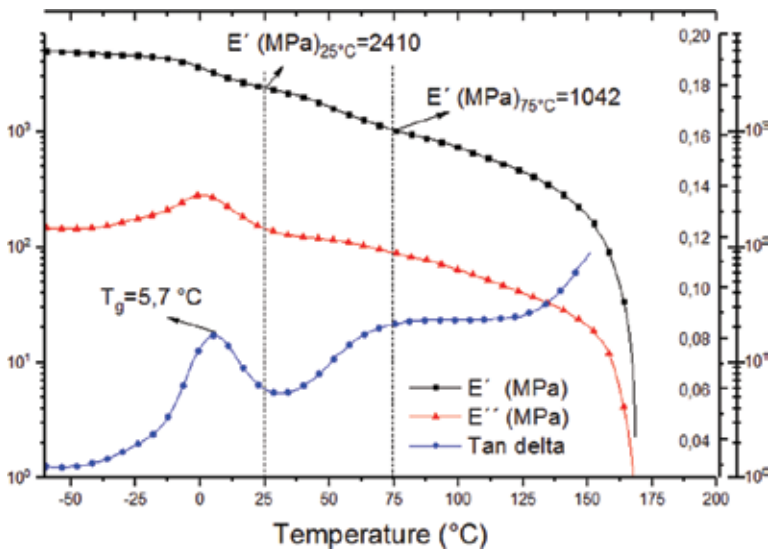

Figure 12. Dynamic mechanical analysis (DMA) curves of PP-Bag + NaOH+Silane biocomposite.

Figure 13 shows the summary of the temperature sweep tests for biocomposites. The tan delta graphics show that there are no significant changes in the Tg of the biocomposites compared to the PP matrix. The values of Tg range between 3.7°C and 6.5°C. Also, these graphs show a reinforcing effect in the PP-bag biocomposite. Tan delta values varied 19.8% compared to the PP matrix. In the case of biocomposite PP-Bag + NaOH, this variation was 32.64% while in the biocomposite PP-Bag + NaOH+ Silane was 32.95%.

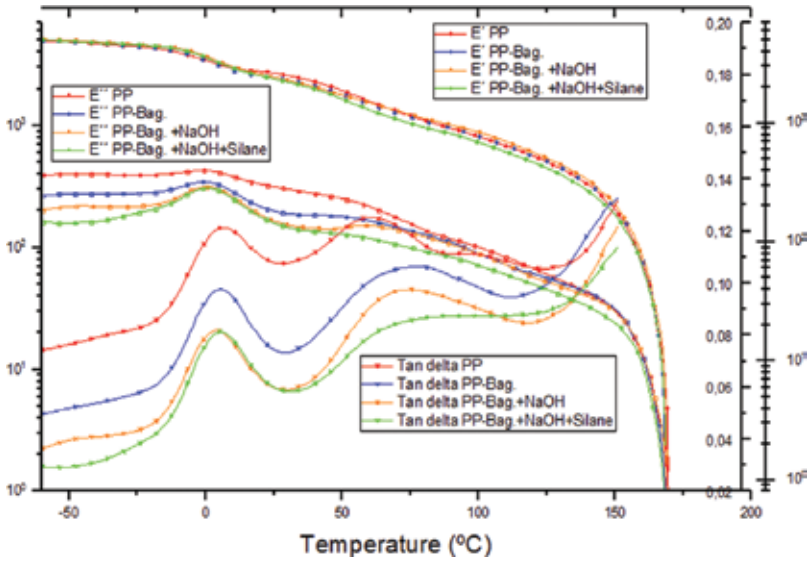

Figure 13. Dynamic mechanical analysis (DMA) curves of neat PP and its composites.

With temperature increase, a second peak is observed around 60°C for neat PP. This peak can be related to an alpha transition. In the case of biocomposites, this alpha transition can be spotted at higher temperatures. This suggests that the service temperature of the biocomposites with alkaline and silanized treatments would allow a better performance of the material. In this experiment observed that the addition of silane to bagasse does not generate an improvement in the viscoelastic properties compared to the alkalinization treatment. It is emphasized that the alkalization treatment generates an improvement against the damping. This improvement can be positive for biocomposite applications that require an enhanced mechanical performance against stresses produced by bending loads.

3.2.3. Thermal characterization

3.2.3.1. Differential scanning calorimetry (DSC)

The first heating runs of PP and PP-bagasse biocomposite were shown in **Figure 14**. Both samples exhibit an endothermic peak between 163 and 165°C corresponding to the melting of the PP matrix. These results indicate that the addition of the bagasse fibers does not disturb the melting processes of the PP matrix.

3.2.3.2. Thermogravimetric analysis (TGA)

TG and DTG curves for PP and PP-bagasse biocomposites are shown in **Figure 15a** and **b**, respectively. Neat PP degradation occurs in a single-step process with an onset temperature (To) located at 371°C and a T_{max} of 449°C. Regarding biocomposites, TG and DTG show that degradation occurs in a two-step process. The first degradation step is associated with the

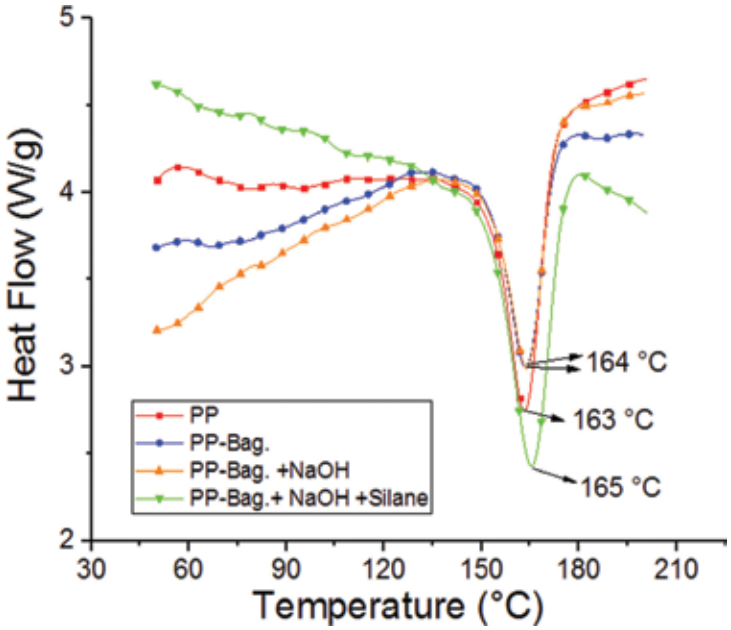

Figure 14. First heating DSC curves for neat PP and PP-bagasse biocomposites.

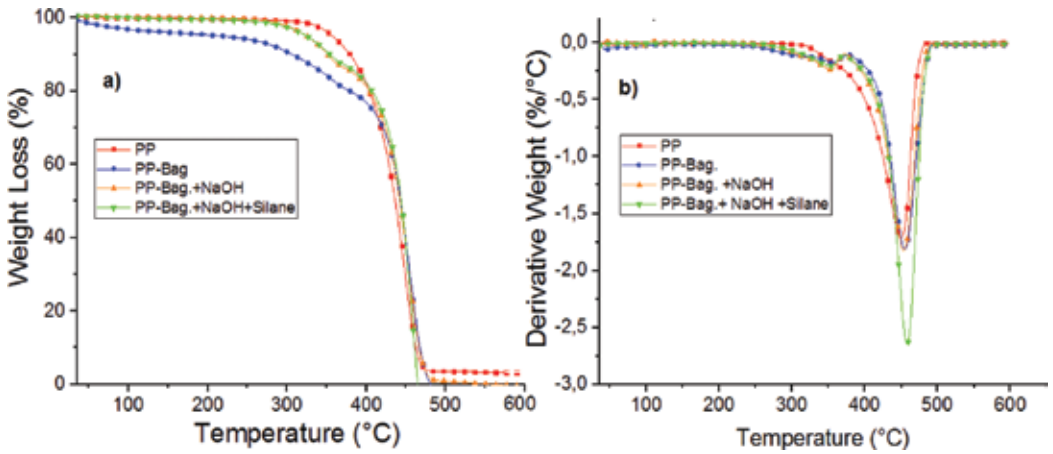

Figure 15. (a) TG and (b) DTG curves of neat PP and PP-bagasse biocomposites.

decomposition of fiber constituents with a To located between 264 and 311°C for neat bagasse and silane-modified bagasse, respectively. This result indicates that chemical treatments improve the thermal stability of bagasse fibers.

The second degradation step corresponds to the decomposition of PP matrix. As shown in **Table 2**, To increases between 51 and 53°C. Also, T_{max} increase between 4 and 9°C in comparison

Sample	Degradation stage	T_0 (°C)	T_{max} (°C)
PP	1	371	449
PP-Bag	1	264	353
	2	423	455
PP-Bag + NaOH	1	310	355
	2	422	453
PP-Bag + NaOH + Silane	1	311	355
	2	424	458

To: onset of inflection of each stage in TG curves.
T_{max}: peak of the maximum degradation rate in DTG curves.

Table 2. Thermal degradation data of the samples at 10°C/min in nitrogen atmosphere.

to neat PP. This increment in the thermal stability of the biocomposites has been previously observed in different studies [36, 37], indicating that the incorporation of fibers in the material induces spherulite nucleation points, increasing the crystallinity of the polymer and improving its thermal properties.

3.3. Morphology

Figure 16 shows SEM images of fractured surfaces from PP-Bag and PP-Bag+NaOH+Silane biocomposites. Gaps between the bagasse fibers and the surrounding PP matrix can be clearly observed in **Figure 16a**, which indicates a poor interfacial adhesion between the PP matrix and the bagasse fibers [38]. For **Figure 16b**, with the chemical treatments, we can see that the gaps between bagasse and PP were reduced significantly and exhibited improved interface for the composite. This result confirms that chemical treatments expose the bagasse fibers and provided links between the cellulosic fibers and the surrounding polymer long chains, which improved the interfacial property of the hydrophobic PP matrix and the hydrophilic bagasse.

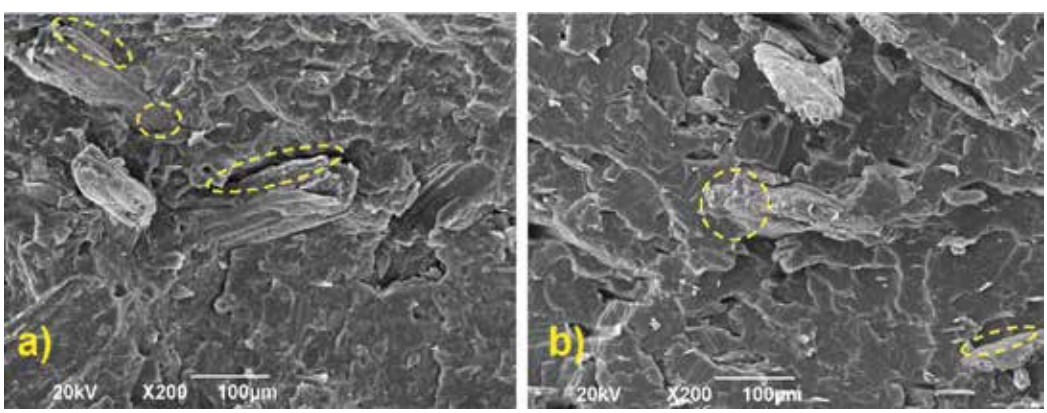

Figure 16. SEM pictures for a) PP-Bagasse and b) PP-Bag + NaOH+Silane biocomposites.

4. Conclusions

The chemical composition and thermal behavior of neat and chemically modified sugar bagasse fibers were studied. The biocomposites of bagasse fiber incorporated into a PP matrix were prepared by a melt-extrusion, injection, and thermocompression processes. The effects of bagasse fibers and chemical modification on the properties of the biocomposites were explored. Flexural characterization showed that bagasse fiber incorporation induces a significant improvement of flexural properties of PP. Also, the impact tests showed that the addition of silanized bagasse increases the capacity of PP to absorb energy. The DMA experiments show that bagasse fiber addition improves the maximum service temperature of the PP matrix. It was also observed that silanization process didn't improve the viscoelastic properties compared to the alkalinization treatment. However, the alkalization treatment generates an improvement against the damping of the PP matrix. Thermal studies show that bagasse fiber addition did not disturb the melting process and improves the thermal stability of the PP matrix. This study offers an environmentally friendly alternative for utilizing waste bagasse fiber generated by the sugar industry for the production of biocomposites.

Acknowledgements

The authors acknowledge the Autónoma de Occidente University, Cali-Colombia, for the technical and financial support; the nanocharacterization center of Virginia Commonwealth University, Virginia-United States, for EDX and SEM spectra; Santiago de Cali University, Cali-Colombia, for its support in the use of FAAS; Servicio Nacional de aprendizaje (SENA), Cali-Colombia, for the financial support through the System of Research, Technological Development and Innovation (SENNOVA). In addition, we wish to thank the company "Sucromiles" Colombia, for providing the sugarcane bagasse.

Conflict of interest

The authors of this manuscript declare that they do not hold any conflicts of interest that might have any bearing on research reported in their submitted manuscript.

Author details

Miguel Ángel Hidalgo-Salazar[1]*, Fernando Luna-Vera[2] and Juan Pablo Correa-Aguirre[1]

*Address all correspondence to: mahidalgo@uao.edu.co

1 Research Group for Manufacturing Technologies GITEM, Universidad Autónoma de Occidente, Cali, Colombia

2 Research Group for Development of Materials and Products GIDEMP, National Center for Technical Assistance to Industry (ASTIN-SENA), Cali, Colombia

References

[1] Joseph K, Thomas S, Pavithran C. Effect of chemical treatment on the tensile properties of short sisal fibre-reinforced polyethylene composites. Polymer (Guildf). 1996;**37**(23):5139-5149. Available from: https://www.sciencedirect.com/science/article/pii/0032386196001449

[2] Chen HL, Porter RS. Composite of polyethylene and kenaf, a natural cellulose fiber. Journal of Applied Polymer Science. 1994;**54**(11):1781-1783. DOI: 10.1002/app.1994.070541121

[3] Coutinho FMB, Costa THS, Carvalho DL. Polypropylene-wood fiber composites: Effect of treatment and mixing conditions on mechanical properties. Journal of Applied Polymer Science. 1997;**65**(6):1227-1235. DOI: 10.1002/%28SICI%291097-4628%2819970808%2965%3A6%3C1227%3A%3AAID-APP18%3E3.0.CO%3B2-Q

[4] La Mantia FP, Morreale M. Improving the properties of polypropylene–wood flour composites by utilization of maleated adhesion promoters. Composite Interfaces. 2007;**14**(7-9):685-698. DOI: 10.1163/156855407782106500

[5] Khalil HPSA, Rozman HD, Ahmad MN, Ismail H. Acetylated plant-fiber-reinforced polyester composites: A study of mechanical, hygrothermal, and aging characteristics. Polymer-Plastics Technology and Engineering. 2000;**39**(4):757-781. DOI: 10.1081/PPT-100100057

[6] Mathew L, Joseph KU, Joseph R. Isora fibres and their composites with natural rubber. Progress in Rubber, Plastics and Recycling Technology. 2004;**20**(4):337-349

[7] La Mantia FP, Morreale M. Green composites: A brief review. Composites Part A: Applied Science and Manufacturing. 2011;**42**(6):579-588. Available from: https://www.sciencedirect.com/science/article/pii/S1359835X11000406

[8] Panthapulakkal S, Raghunanan L, Sain M, KC B, Tjong J. Natural fiber and hybrid fiber thermoplastic composites: Advancements in lightweighting applications. Green Composites. 2017:39-72. Available from: https://www.sciencedirect.com/science/article/pii/B9780081007839000034

[9] El-Sabbagh A. Effect of coupling agent on natural fibre in natural fibre/polypropylene composites on mechanical and thermal behaviour. Composites Part B: Engineering. 2014;**57**:126-135. Available from: https://www.sciencedirect.com/science/article/pii/S135983681300560X

[10] Truong M, Zhong W, Boyko S, Alcock M. A comparative study on natural fibre density measurement. Journal of the Textile Institute. 2009;**100**(6):525-529. DOI: 10.1080/00405000801997595

[11] Teja MS, Ramana MV, Sriramulu D, Rao CJ. Experimental investigation of mechanical and thermal properties of sisal fibre reinforced composite and effect of sic filler material. IOP Conference Series Materials Science and Engineering. 2016;**149**(1):012095. Available from: http://stacks.iop.org/1757-899X/149/i=1/a=012095?key=crossref.f5867800e25ad9145654bd70cae9ae11

[12] Ashik KP, Sharma RS. A review on mechanical properties of natural fiber reinforced hybrid polymer composites. Journal of Minerals and Materials Characterization and Engineering. 2015;**03**(05):420-426. Available from: http://www.scirp.org/journal/PaperDownload.aspx?DOI=10.4236/jmmce.2015.35044

[13] Posada JA, Osseweijer P. Socioeconomic and environmental considerations for sustainable supply and fractionation of lignocellulosic biomass in a biorefinery context. Biomass Fractionation Technology a Lignocellulosic Feedstock Based Biorefinery. 2016:611-631. Available from: https://www.sciencedirect.com/science/article/pii/B9780128023235000268

[14] Hagemann N, Gawel E, Purkus A, Pannicke N, Hauck J. Possible futures towards awood-based bioeconomy: A Scenario Analysis for Germany. Sustain. 2016;**8**(98):1-24

[15] Carlos Cueva-Orjuela J, Hormaza-Anaguano A, Merino-Restrepo A. Sugarcane bagasse and its potential use for the textile effluent treatment. DYNA. 2017;**84**(203):291-297. DOI: 10.15446/dyna.v84n203.61723

[16] Vilay V, Mariatti M, Mat Taib R, Todo M. Effect of fiber surface treatment and fiber loading on the properties of bagasse fiber–reinforced unsaturated polyester composites. Composites Science and Technology. 2008;**68**(3-4):631-638. Available from: https://www.sciencedirect.com/science/article/pii/S0266353807003843

[17] Huang Z, Wang N, Zhang Y, Hu H, Luo Y. Effect of mechanical activation pretreatment on the properties of sugarcane bagasse/poly(vinyl chloride) composites. Composites Part A: Applied Science and Manufacturing. 2012;**43**(1, 1):114-120. Available from: https://www.sciencedirect.com/science/article/pii/S1359835X11003228

[18] Beninia KCCC, Voorwald HJC, Cioffi MOH. Mechanical properties of HIPS/sugarcane bagasse fiber composites after accelerated weathering. Procedia Engineering. 2011;**10**:3246-3251. Available from: https://www.sciencedirect.com/science/article/pii/S1877705811007247

[19] Mulinari DR, Voorwald HJC, Cioffi MOH, da Silva MLCP, Luz SM. Preparation and properties of HDPE/sugarcane bagasse cellulose composites obtained for thermokinetic mixer. Carbohydrate Polymers. 2009;**75**(2):317-321. Available from: https://www.sciencedirect.com/science/article/pii/S014486170800338X

[20] Fogorasi M, Barbu I. The potential of natural fibres for automotive sector—review. IOP Conference Series Materials Science and Engineering. 2017

[21] Mohammed L, Ansari MNM, Pua G, Jawaid M, Islam MS. A review on natural fiber reinforced polymer composite and its applications. The International Journal of Polymer Science. 2015;**2015**:1-15. Available from: http://www.hindawi.com/journals/ijps/2015/243947/

[22] Rao J, Zhou Y, Fan M. Revealing the interface structure and bonding mechanism of coupling agent treated WPC. Polymers (Basel). 2018;**10**(3):266-279

[23] Catto AL, Stefani BV, Ribeiro VF, Santana RMC. Influence of coupling agent in compatibility of post-consumer HDPE in thermoplastic composites reinforced with eucalyptus

fiber. Materials Research. 2014;**17**(suppl 1):203-209. Available from: http://www.scielo.br/scielo.php?script=sci_arttext&pid=S1516-14392014000700033&lng=en&tlng=en

[24] Zou H, Wu S, Shen J. Polymer/silica nanocomposites: Preparation, characterization, properties, and applications. Chemical Reviews. 2008;**108**(9):3893-3957. Available from: http://pubs.acs.org/doi/abs/10.1021/cr068035q

[25] Clemons CM, Sabo RC, Kaland ML, Hirth KC. Effects of silane on the properties of wood-plastic composites with polyethylene-polypropylene blends as matrices. Journal of Applied Polymer Science. 2011;**119**(3):1398-1409. DOI: 10.1002/app.32566

[26] Lu JZ, Professor A, McNabb HS, Professor J. Society of wood science and technology state-of-the-art review Chemical coupling in wood fiber and polymer composites: A review of coupling agents and treatments' Qinglin W u t

[27] Cao H, Amador C, Jia X, Ding Y. Capillary dynamics of water/ethanol mixtures. Industrial and Engineering Chemistry Research. 2015;**54**(48):12196-12203. DOI: 10.1021/acs.iecr.5b03366

[28] Prakash S, Xi E, Patel AJ. Spontaneous recovery of superhydrophobicity on nanotextured surfaces. Proceedings of the National Academy of Sciences of the United States of America. 2016;**113**(20):5508-5513. Available from: http://www.ncbi.nlm.nih.gov/pubmed/27140619

[29] Li X, Tabil LG, Panigrahi S. Chemical treatments of natural fiber for use in natural fiber-reinforced composites: A review. Journal of Polymers and the Environment. 2007;**15**(1):25-33. DOI: 10.1007/s10924-006-0042-3

[30] Luna Vera F, Melo Cortes HA, Viviana Murcia C, Charry Galvis I. Informador técnico. Informador técnico. 2014;**78**(2):106-114. ISSN 0122-056X, ISSN-e 2256-5035. Centro Nacional de Asistencia Técnica a la Industria, ASTIN-SENA. Available from: https://dialnet.unirioja.es/servlet/articulo?codigo=5129559

[31] Lin B-J, Chen W-H. Sugarcane bagasse pyrolysis in a carbon dioxide atmosphere with conventional and microwave-assisted heating. Frontiers in Energy Research. 2015;**3**:1-4

[32] Sood M, Dwivedi G. Effect of fiber treatment on flexural properties of natural fiber reinforced composites: A review. Egypt J Pet [Internet]. 2017;**26**(4):911-919

[33] Malenab RAJ, Ngo JPS, Promentilla MAB. Chemical treatment of waste abaca for natural fiber-reinforced geopolymer composite. Materials (Basel, Switzerland). 2017;**10**(6):579-598

[34] Goulart SAS, Oliveira TA, Teixeira A, Miléo PC, Mulinari DR. Mechanical behaviour of polypropylene reinforced palm fibers composites. In: Procedia Engineering. 2011;**10**:2034-2039

[35] Chui-gen G, Yong-ming S, Qing-wen W, Chang-sheng S. Dynamic-mechanical analysis and SEM morphology of wood flour/polypropylene composites. 2006;**17**(4):315-318

[36] Hidalgo-Salazar MA, Munõz MF, Mina JH. Influence of incorporation of natural fibers on the physical, mechanical, and thermal properties of composites LDPE-Al reinforced with fique fibers. International Journal of Polymer Science. 2015;**2015**:1-8

[37] Luz SM, Gonçalves AR, Del'arco AP, Ferrão PMC. Composites from Brazilian natural fibers with polypropylene: mechanical and thermal properties. Composite Interfaces. 2008;**15**(7-9):841-850. DOI: 10.1163/156855408786778366

[38] Hidalgo-Salazar MA, Mina JH, Herrera-Franco PJ. The effect of interfacial adhesion on the creep behaviour of LDPE-Al-Fique composite materials. Composites Part B: Engineering. 2013;**55**:345-351. Available from: https://www.sciencedirect.com/science/article/pii/S1359836813003430

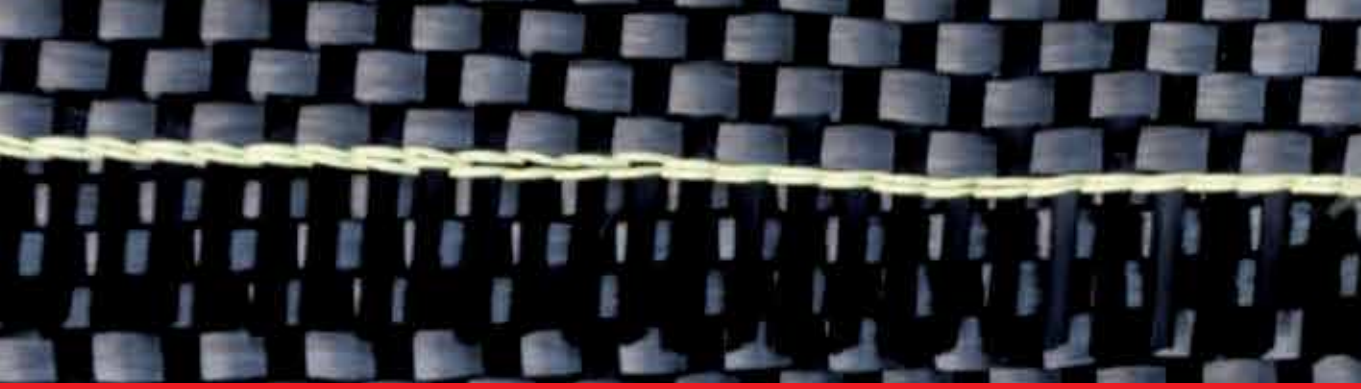

Edited by Hosam El-Din M. Saleh and Martin Koller

Composite materials are materials made from two or more constituents with significantly different physical or chemical properties; when combined, a new material with characteristics different from the individual components is produced, while the individual components remain separate and distinct within the finished structure. The new composite material often displays many beneficial characteristics; in many cases, composites are stronger, of lower density, or less costly in comparison to established materials.

Based on the classification of composites, we are already familiar with the fact that there exists a myriad of different types of these materials. It is a common saying that different types of composites differ in their performance. Yet, composites also have some characteristics in common.

The proper material choice for an envisaged application is of outstanding importance and key in the development of a new product. Selecting the most suitable material determines the performance and characterization of the final product whether it will meet the designated function and performance requirements.

The present book "Characterizations of some composite materials" contains eight selected chapters, starting with a general introductory chapter on composite materials, and covers different aspects in characterizing some composite materials.

In this context, the present book is considered an appropriate way to communicate the advances in characterization of some composite materials to the scientific community. Chemists, scientists, and researchers from related areas, and undergraduates involved in materials issues and interested in approaches to improve the quality of life, as well as people from industry could find this book to be an inspiring and effective guide.

Published in London, UK

IntechOpen

ISBN 978-1-83881-734-3